

EXPERIMENTAL STUDY OF PRESSURE DROP AND BUBBLE SIZE IN A  
LABORATORY SCALE COMPRESSED AIR FOAM  
GENERATION SYSTEM

by

Dhrupad Parikh

**Copyright by Dhrupad Parikh 2017**

All Rights Reserved

A thesis submitted to the Faculty and the Board of Trustees of the Colorado School of Mines in partial fulfillment of the requirements for the degree of Master of Science (Mechanical Engineering).

Golden, Colorado

Date \_\_\_\_\_

Signed: \_\_\_\_\_  
Dhrupad Parikh

Signed: \_\_\_\_\_  
Dr. Nils Tilton  
Thesis Advisor

Golden, Colorado

Date \_\_\_\_\_

Signed: \_\_\_\_\_  
Dr. Greg Jackson  
Professor and Head  
Department of Mechanical Engineering

## ABSTRACT

Underground tunneling involves the treatment and transportation of large amounts of soil using various conditioning agents. Foam, the most common conditioning agent, is injected into the soil at the cutter head of the tunnel boring machine. The foam transforms the excavated material into a deformable soil paste that provides a homogenous pressure to the surrounding ground, improves stability of the tunnel face, and minimizes friction and wear on metallic parts of a TBM. In the tunneling industry, foam is generated by flowing a mixture of air, water, and surfactant through a porous medium such as packed beads. Extensive studies have been done on the properties of conditioned soil; however, little literature exists on the mechanical system that generates the foam.

This study focused on understanding the influence of the design and operating parameters of a foam generation system on different foam properties by replicating the foam generation process on a tunneling site. The foam generation system comprised of a foam generator filled with beads, a transport pipe to transfer the foam, and a pressure chamber in which we injected the foam under different pressures. Different system parameters were explored, such as size of bead fillings in the generator (1, 2, 3 mm), lengths of foam generator (110, 200, 400 mm), length (1, 3, 5 m) and diameter (6.3, 9.5, 12.7 mm) of foam transport pipes, and chamber pressure (1, 3, 5 bar). The air and liquid mass flow rates were varied as 9.5 to 49 slpm and 0.3 to 2.2 slpm respectively. Foam properties such as the foam bubble size distribution, stability, and compressibility were investigated. Based on the experimental study it was found that the average bubble diameter decreased with decrease in bead size. The pore-scale mixing governed the bubble diameter for 3 mm bead size, while the pore size played a dominant role in case of 1 and 2 mm beads. The chamber

pressure also had a significant influence on the foam bubble diameter and foam stability. With the increase in the chamber pressure, the bubble diameter decreased, and the foam stability increased.

Some preliminary experiments are conducted to investigate if foam could be generated without a foam generator, and how would the bubble size vary through a transport pipe. It was observed that foam could be generated without a foam generator if longer transport pipes are used.

## TABLE OF CONTENTS

ABSTRACT .....	iii
LIST OF FIGURES .....	viii
LIST OF TABLES .....	xiii
ACKNOWLEDGEMENT .....	xiv
CHAPTER 1 INTRODUCTION .....	1
1.1 Overview .....	1
1.2 Foam Generation on Tunnel Boring Machines .....	4
1.3 Motivation .....	5
1.4 Objectives .....	6
CHAPTER 2 LITERATURE REVIEW .....	8
2.1 Foams and Foam Stability .....	8
2.2 Foam Rheology .....	11
2.3 Foam flow through pipes .....	15
2.4 Bubble Size Analysis .....	18
2.5 Flow through porous media .....	19
2.6 Mechanism of foam generation through porous media .....	21
CHAPTER 3 EXPERIMENTAL METHODS .....	23
3.1 Laboratory-Scale Foam Generation System .....	23
3.2 Foam Compressibility .....	30
3.3 Foam Drainage .....	31

CHAPTER 4	RESULTS AND DISCUSSION: FLOW CHARACTERIZATION.....	34
4.1	Characterization of Pressure and Foam Flow Velocity .....	35
4.2	Influence of Flow Rate .....	37
4.3	Influence of Bead Diameter.....	40
4.4	Influence of Length of Foam Generator .....	45
4.5	Influence of Length of Foam Transport Pipe .....	49
4.6	Influence of Pressure Chamber.....	52
4.7	Influence of Transport Pipe Diameters.....	54
4.8	Pressure drop for single phase and multiphase flow using pressure chamber.....	56
CHAPTER 5	RESULTS AND DISCUSSION: BUBBLE SIZE ANALYSIS .....	58
5.1	Foam Capture and Image Analysis.....	58
5.2	Influence of operating parameters on bubble distribution.....	59
5.3	Foam Compressibility.....	77
5.4	Foam Drainage.....	78
5.5	Variation of foam bubble diameter through transport pipe .....	79
CHAPTER 6	DIMENSIONAL ANALYSIS AND FLOW REGIMES.....	82
6.1	Dimensional analysis for foam generator .....	82
6.2	Reynolds number and flow regimes in the foam generator.....	85
6.3	Dimensional analysis for foam transport pipe .....	90
CHAPTER 7	SUMMARY AND CONCLUSIONS.....	92

7.1	Summary of key findings.....	92
7.2	Recommendation for Future Work.....	97
	REFERENCES .....	98
APPENDIX A	PROCEDURE FOR PRESSURE CHAMBER TESTS AND FOAM CAPTURE.....	104
APPENDIX B	HISTOGRAM AND LOG-NORMAL DISTRIBUTION.....	107

## LIST OF FIGURES

Figure 1.1	Key components of Earth Pressure Balance - Tunnel Boring Machine, image courtesy of Herrenknecht Tunneling System .....	2
Figure 1.2	Aqueous foam injected through the foam port from the cutter head on a TBM .....	3
Figure 1.3	Schematic of a foam generation system on EPB-TBM. The schematic shows the foam solution tank and the compressed air units for various generators. The foam ports are also indicated shown on the cutter head of the EPB-TBM.....	5
Figure 2.1	Microscopic view of the foam structure indicating the lamella, plateau border, and interface region. Image redraw from Emulsion, Foams, and Suspensions: Fundamentals and Applications by Laurier L. Schramm .....	9
Figure 2.2	Internal pressure inside a bubble $P_G$ and the partial pressure of liquid $P_L$ .....	10
Figure 2.3	Classification of different fluids based on the shear stress ( $\tau$ ) and shear rate plots ...	12
Figure 2.4	Plot showing velocity profiles for foam flow through circular tubes of different diameter. Parabolic profile is observed at low flow rate (dashed line), and plug-like flow at a high flow rate (solid line). Image is a qualitative representation from David & Marsden (1969).....	14
Figure 2.5	Flow regions through the cone and plane rheometer and pipe flow. Region A - Newtonian slip layer, region B - unsheared foam and region C - sheared foam. Image redraw from Calvert 1986.....	15
Figure 2.6	Bubble frequency distribution with respect to average bubble diameter for foam drainage at various time. Qualitative plot is redrawn from Lemlich et al. (1985) ....	19
Figure 2.7	Mechanism of foam generation through porous media: (a) snap-off (b) lamella division .....	21
Figure 3.1	Schematic of the laboratory foam generation system and foam testing device. Not to scale. The FCD can be used to photograph the foam bubbles at the outlet of foam generator, and at the inlet of the pressure chamber .....	25
Figure 3.2	Foam generator filled with 3 mm beads. The length of the foam generator is 200 mm and the diameter is 15.2 mm.....	25
Figure 3.3	Mass flow controllers for air and surfactant solution. The solid arrows show flow of air supply and the dotted arrows indicate inlet & outlet of surfactant solution.....	27

Figure 3.4 Pressure chamber setup to conduct experiments under pressure up to 5 bar. The solid arrow shows compressed air supply, and dotted arrows show foam flow. A back pressure regulator connected with a pressure gauge is placed in the top of the pressure chamber .....	28
Figure 3.5 Set-up for photographing foam bubbles using a bleed-off valve, a foam capture device, a microscope and a back pressure regulator .....	29
Figure 3.6 Screenshot of image analysis of foam bubbles using AmScope software. ....	29
Figure 3.7 Setup of the foam generation system to inject foam into the pressure chamber for the foam compressibility and drainage tests.....	30
Figure 3.8 Schematic, not to scale, of foam compressibility .....	31
Figure 3.9 Funnel test to determine stability (half-life) of foam .....	32
Figure 3.10 Schematic, not to scale, of liquid drainage from the foam over time.....	32
Figure 4.1 Sketch, not to scale, of the foam generator filled with beads.....	36
Figure 4.2 Variation of pressure and superficial air velocity across the foam generator: (a) Absolute pressure at the inlet and outlet of foam generator; (b) Superficial air velocity at the inlet and outlet of foam generator. The experiment is performed using 1 mm .....	38
Figure 4.3 Variation of pressure and superficial air velocity across the foam generator for 1, 2, 3 mm bead diameter: (a) Pressure variation at the inlet and outlet of foam generator; (b) superficial air velocity at the inlet and outlet of foam generator .....	40
Figure 4.4 Pressure drop ( $\Delta P$ ) for 1, 2, 3 mm bead foam generator: (a) Pressure drop through the 1m foam transport pipe; (b) Pressure drop across the foam generator. $\Delta P_{\text{Foam generator}}$ is higher than $\Delta P_{\text{Transport pipe}}$ for 1mm bead foam generator .....	42
Figure 4.5 Pressure drop across transport pipe as a function of average foam velocity on a log plot.....	43
Figure 4.6 Pressure drop across foam generator as a function of average foam velocity on a log-log plot.....	44
Figure 4.7 Absolute pressure and superficial air velocity for different lengths of foam generator: (a) absolute pressure at the inlet and outlet of foam generator; (b) superficial air velocity at the inlet and outlet of foam generator .....	45
Figure 4.8 Pressure drop per unit length across the transport pipe as a function of average superficial air velocity. ....	47

Figure 4.9 Pressure drop as a function of average foam velocity: (a) pressure drop through foam generator (b) Pressure drop per unit length through the foam generator. The dashed line is the best fit for the data points that indicate a linear regime. ....	48
Figure 4.10 Absolute pressure and superficial air velocity for three different lengths of foam transport pipe: (a) Absolute pressure at the inlet and outlet of foam generator; (b) Superficial air velocity at the inlet and outlet of foam generator. The pressure at the inlet of 3m tube and outlet of 5 m tube are similar, hence their superficial velocities are overlapping. ....	49
Figure 4.11 Pressure drop for 1, 3 and 5 m foam transport pipe lengths: (a) Pressure drop through the foam transport pipe; (b) Pressure drop per unit length through the transport pipe. ....	50
Figure 4.12 Pressure drop across the foam generator for 1, 3, 5 m lengths of foam transport pipe .....	51
Figure 4.13 Variation of flow parameters in pressure chamber tests: (a) Absolute pressure at the inlet and outlet of foam generator. Dotted lines indicate inlet and solid lines outlet conditions across the foam generator; (b) Variation of superficial air velocity at the inlet and outlet of the generator. ....	52
Figure 4.14 Pressure drop for the foam flow across the foam generator and transport pipe for different chamber pressures: (a) Pressure drop through the transport tube for different average foam velocity across the pipe; (b) Pressure drop through the foam generator .....	53
Figure 4.15 Pressure drop across the foam transport pipe for diameters 6.3, 9.5 and 12.7 mm. The length of the transport pipe is fixed at 1m, the FER is 15, and the length of foam generator is 200 mm. ....	55
Figure 4.16 Pressure drop for single phase flow across the foam generator under 1 bar chamber pressure with varying mass flow rates: (a) Pressure drop for air flow; (b) Pressure drop for water flow. Length of foam generator is 200 mm, bead size is 3 mm and FERp is .....	56
Figure 4.17 Pressure drop across the foam generator for multiphase (air and water) flow - dashed line, and foam flow - solid line. For both the tests the length of the foam generator is 200 mm, the length of transport pipe is 1 m, and bead size is 3 mm. ....	57
Figure 5.1 Sample photograph of foam bubbles during analysis using Amscope software .....	59
Figure 5.2 Average bubble diameter as a function of average superficial air velocity ( $V_{avg,air}$ ) across the foam generator for three different bead diameters 1 mm, 2 mm and 3 mm. The dashed lines indicate linear fit for the data points. For this experiment the length of foam gun is 110 mm, length of foam transport tube is 1 m, and FER is 15 .....	61

Figure 5.3	Bubble images for three bead diameters at $V_{\text{avg,air}} = \sim 0.4$ m/s. The average bubble diameter for these three cases is shown by red circles in figure 5.2.....	61
Figure 5.4	Bubble size distribution for the three bead diameters at $V_{\text{avg,air}} = 0.4$ m/s. These distributions are for the bubble images shown in figure 5.3.....	64
Figure 5.5	Bubble size distribution for foam bubbles generated using 3 mm beads. The length of foam generator is 110 mm, length of transport pipe is 1 m and the FER is 15.....	65
Figure 5.6	(a) and (b) Bubble size distribution for 2 mm and 1 mm bead diameter at different air mass flow rates, (a) bubble size distribution for 2 mm beads; (b) bubble size distribution for 1 mm beads. The length of foam generator is 110 mm, length of transport pipe is 1 m .....	66
Figure 5.7	Average bubble diameter as a function average superficial air velocity across the generator. The FER is 15, length of foam transport pipe is 1 m, and bead size is 3 mm .....	68
Figure 5.8	Bubble size distributions for a different length of foam generator with varying air mass flow rates, (a) bubble size distribution for 200 mm foam generator; (b) bubble size distribution for 400 mm foam generator. The length of transport pipe is 1 m and bead size is 3 m.....	70
Figure 5.9	Average bubble diameter as a function of average superficial air velocity ( $V_{\text{avg,air}}$ ) across the foam generator for different lengths of foam transport pipe. The length of foam generator = 110 mm, and bead diameter = 3 mm .....	71
Figure 5.10	Bubble size distributions for different lengths of foam transport pipe with varying air mass flow rates, (a) Bubble size distribution for 3 m foam transport pipe; (b) bubble size distribution for 5 m pipe. The length of foam gun is 110 mm, and bead size is 3 mm. ....	73
Figure 5.11	Average bubble diameter measured at the outlet of the foam generator when the foam is injected into a pressure chamber under 1, 3 and 5 bar pressure. The length of foam generator is 200 mm, bead diameter is 3 mm and $FER_p = 15$ .....	74
Figure 5.12	Bubble size distribution at 1 bar chamber pressure for various air flow rates. Length of foam gun is 200 mm, length of transport pipe is 1 m, bead size = 3 mm, and $FER_p = FER = 15$ .....	75
Figure 5.13	Bubble size distributions for different chamber pressures, (a) bubble size distribution for 3 bar chamber pressure; (b) bubble size distribution for 5 bar chamber pressure. The length of foam generator is 200 mm, bead size is 3 mm, and $FER = 15$ .....	77

Figure 5.14 Foam compressibility at time = 5 minutes for various range of flow rates at different chamber pressures. The bead size is 3 mm, the length of transport pipe is 1 m, and length of foam generator is 200 mm.....	78
Figure 5.15 Foam liquid volume loss after 30 minutes as a function of the average superficial velocity across the foam generator for different chamber pressure.....	79
Figure 5.16 Average bubble diameter at every 1 m distance through a 5 m long transport pipe. The data labels indicate the average foam velocity at that instance. Foam is produced without a foam generator. ....	80
Figure 6.1 Foam generator with different parameters considered for dimensional analysis .....	83
Figure 7.1 Subdivision of foam bubbles as they flow downstream of the generator.....	95
Figure 7.2 Limitation in the minimum bubble diameter.....	95
Figure 7.3 Expansion of foam bubbles as they flow downstream of the generator.....	95
Figure A.1 Laboratory set-up for generating foam.....	105
Figure B.1 Histogram with overlaid log-normal distribution for 1 mm beads.....	107
Figure B.2 Histogram with overlaid log-normal distribution for 2 mm beads.....	108
Figure B.3 Histogram with overlaid log-normal distribution for 3 mm beads.....	109
Figure B.4 Histogram with overlaid log-normal distribution for 200 mm length of generator..	110
Figure B.5 Histogram with overlaid log-normal distribution for 400 mm length of generator..	111
Figure B.6 Histogram with overlaid log-normal distribution for 3 m length of pipe.....	112
Figure B.7 Histogram with overlaid log-normal distribution for 5 m length of pipe.....	113
Figure B.8 Histogram with overlaid log-normal distribution for 1 bar chamber pressure .....	114
Figure B.9 Histogram with overlaid log-normal distribution for 3 bar chamber pressure .....	115
Figure B.10 Histogram with overlaid log-normal distribution for 5 bar chamber pressure .....	116
Figure B.11 Sample distribution with 95% confidence interval.....	118

## LIST OF TABLES

Table 6.1	Permeability and porosity for bead diameter 1, 2, and 3 mm. Both permeability and porosity are determined experimentally by performing repeated number of tests ....	87
Table 6.2	Reynolds number for air and liquid flow through porous media based on the particle diameter and permeability. The minimum and maximum values are computed based on the flow velocities.....	88
Table B.1	Error analysis for the distribution curves with mean of the log plot ( $\mu$ ) and standard deviation ( $\sigma$ ) .....	118

## ACKNOWLEDGEMENT

The completion of this dissertation would not have been possible without the support, and guidance of several people and I would like to acknowledge my gratitude to these people.

Firstly, I would like to express my gratitude to my advisor Dr. Nils Tilton for his continuous support, guidance, and motivation throughout my studies. His guidance helped me during my research and writing this dissertation.

I am very grateful to my co-advisor Dr. Michael Mooney for his guidance and motivation during my research. Without his assistance, this work would not have been possible.

I want to thank my committee member Dr. Keith Neeves for supporting me throughout my studies and research.

I would like to thank Yuanli Wu and Christian Peterson, for their continuous support and assistance during my laboratory test. I am also thankful to Scott Jarriel and Jordan Hurt for their help during the summer.

Finally, I would like to thank my family, and my friends Abhishek Parikh, Marm Dixit and Anand Parejiya.

## CHAPTER 1 INTRODUCTION

### 1.1 Overview

Over the past 30 years, there has been a rapid rise in the underground construction and tunneling sector, with growing requirement in the mining, infrastructure, transportation and communication industry for railways, pipelines, subways, and cable network [1], [2]. Tunneling technology is increasingly preferred over open excavation techniques due to difficulties in excavation over uneven ground conditions and higher surface disruptions, such as water inflow, unstable faults, wide clefts and different grades of weathered rocks [2]. Tunneling techniques include conventional drill and blast methods and advanced mechanical excavation methods. Presently, mechanical excavation is preferred because it is often more economical than drill and blast methods. Other advantages of mechanical excavation over traditional tunneling methods are [3]

- accurate estimation of production rates and costs for mechanized excavation system;
- elimination of blasting and toxic fumes, improving personnel safety;
- reduction in ground disturbances, leading to less face support requirement.

The current study focuses on Earth Pressure Balance - Tunnel Boring Machines (EPB-TBMs) such as that illustrated in figure 1.1. During operation, the rotating cutter head removes soil from the tunnel face. Simultaneously, a “conditioning agent” is injected through ports in the cutter head. This agent mixes with the excavated soil to form a malleable paste that is removed from the chamber through a screw conveyor, see figure 1.1. Common conditioning agents include aqueous foams, polymers, and bentonite slurries [2], [4], [5]. The malleable soil paste at the cutter

head and excavation chamber applies a mechanical pressure to the tunnel face to counter-balance the earth pressure, and prevent the collapse of the tunnel face. The conditioned soil also has a low permeability and acts to seal the tunnel face and prevents the inflow of groundwater [3], [5].

In contrast to other methods, EPB-TBM works without a secondary support medium such as compressed air, because the excavated conditioned soil serves as a support medium [2], [4]. The use of EPB-TBMs is the most sought-after technique for mechanical excavations through soils ranging from coarse sand and gravels to stiff clays. EPB-TBMs are also preferred when adverse geological effects such as face collapse and ground squeezing are encountered [5], [6].

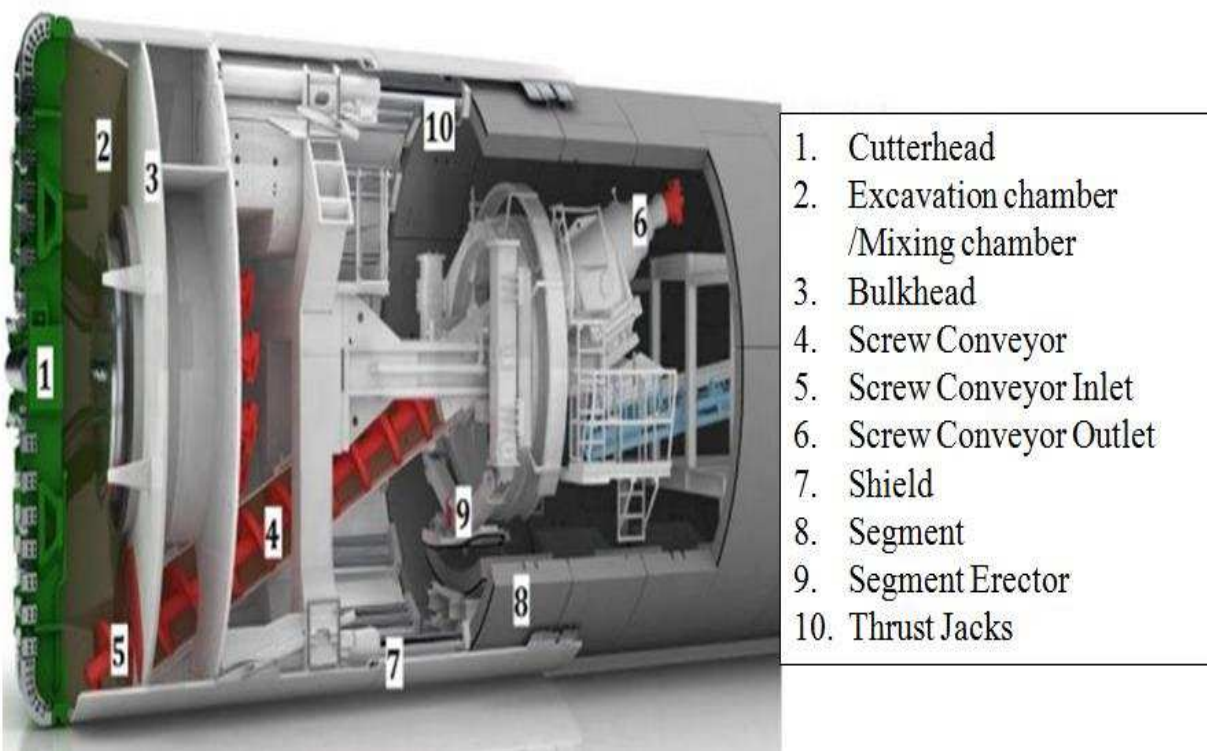


Figure 1.1 Key components of Earth Pressure Balance - Tunnel Boring Machine, image courtesy of Herrenknecht Tunneling System



Figure 1.2 Aqueous foam injected through the foam port from the cutter head on a TBM

Aqueous foams are widely-used additives in soil conditioning. Foams are colloidal dispersions in which a gas (usually air) is dispersed in a continuous liquid phase [7]. The liquid phase is usually a water-surfactant solution. Surfactants are chemical compounds that lower the interfacial tension (free-energy) of the liquid-gas interface to facilitate the creation of stable bubbles. There are certain desired properties of foam suggested for soil conditioning [8]:

- High foam stability in the excavation chamber. Foam stability refers to the tendency for the liquid to drain from the foam with time. Highly stable foams have a slow drainage rate compared to low stability foams.
- The generated foam should have a homogeneous bubble size.
- The foam should have a uniform foam density. This means the air and surfactant solution should mix completely such that the foam has uniform properties.

Soil conditioning is an important aspect of the performance of EPB-TBMs. The conditioned soil improves the performance of tunneling machines by providing the following benefits [2], [5], [9]:

- Control the face pressure of soil during excavation by increasing the soil compressibility and lowering the soil permeability.
- Improve the workability and flow of soil through the screw conveyor that removes the excavated material from the pressurized excavation chamber, see figure 1.1.
- Reduction in torque of the cutterhead by decreasing the shear strength of the soil.
- Reduction in wear of mechanical parts.

## **1.2 Foam Generation on Tunnel Boring Machines**

Figure 1.3 shows a detailed schematic of a generalized EPB-TBM (Mooney, 2017). On EPB-TBM's, foam is generated by flowing a mixture of air and surfactant solution through a tube of randomly packed beads or other materials such as perforated tubes and steel wool. The mass flow rates of air and surfactant solution are selected based on the foam expansion ratio. The foam expansion ratio (FER) is the ratio of the volume of foam to the volume of liquid [1]. A higher FER indicates dry foam, while a lower FER indicates wet foam [11]. On tunneling sites, the FER can range from 5 to 20 [10], [12], [13], though EPB-TBM's commonly use an FER of 15.

An EPB-TBM typically has multiple foam generators that have an inlet supply of compressed air and surfactant solution. The outlet of the foam generators is connected to a transport pipe, which transports the foam to the foam ports, as shown on the cutter head on the schematic in figure 1.3. The foam ports inject foam into the soil and transform the soil into a compressible malleable paste. The injection of foam into the soil is set by the Foam Injection Ratio (FIR), defined as the ratio of the volume of foam to the volume of excavated soil [1], [4].

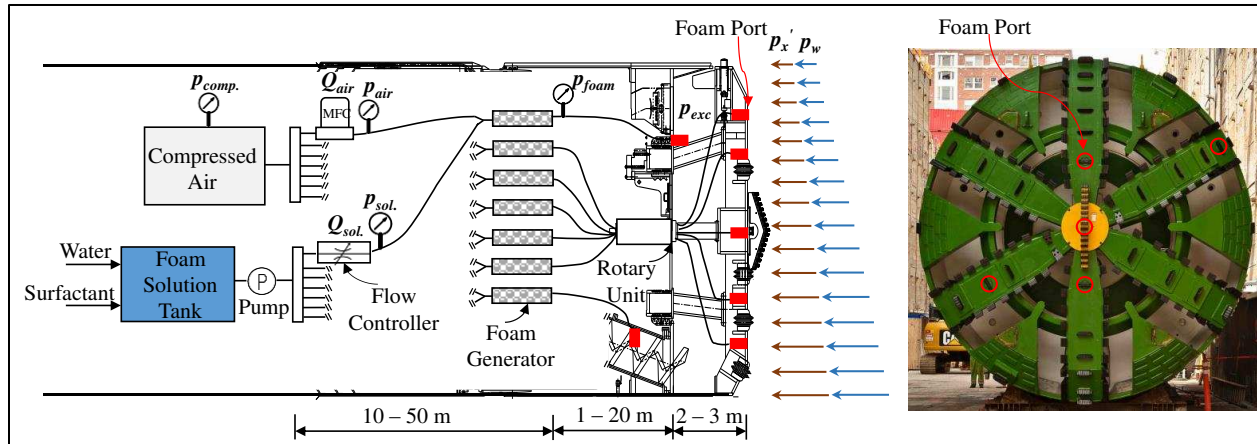


Figure 1.3 Schematic of a foam generation system on EPB-TBM. The schematic shows the foam solution tank and the compressed air units for various generators. The foam ports are also indicated shown on the cutter head of the EPB-TBM

### 1.3 Motivation

The foam generation process and the effect of conditioning treatment on the properties of different soils are not well understood. Presently, the production and dosage of foam for soil conditioning is based on the practical experience of the EPB-TBM operator [3]. When an operator encounters varying ground conditions, the operator varies the FIR based on trial and error, by inspecting the conditioned soil exiting the screw conveyor. For example, if the conditioned soil appears dry, the operator might increase the FIR to increase the amount of foam, or decrease the FER to use wetter foam. This process can lead to considerable downtime on a tunneling site.

Various experimental studies have been performed to study the foam soil interaction, where the foam is generated at atmospheric conditions and mixed with different types of soils [2], [3], [5], [9], [14]–[16]. Few studies have focused on foam production for soil conditioning in EPB-TBMs [8], [17]. Thewes et al. experimentally studied the qualitative analysis of the influence of different operational parameters such as volumetric flow rate, the length of foam transport pipe, surfactant concentration, and FER on foam properties - foam density, drainage time and bubble

size [8]. The authors have used different foam generators (guns), however, they have not studied the influence of the porous material in the generator on foam properties.

Up to now, there have been no systematic studies that vary the operating parameters and porous material to investigate their impact on foam generation. In fact, most studies do not disclose the material used in the generator. Our study focuses on quantitatively understanding the influence of operational parameters on foam generation and flow properties by systematically varying the porous material, length of the foam generator, geometry of the transport pipe and the chamber pressure. While our collaborators at the Underground Construction and Tunneling Center are simultaneously studying the foam-soil interactions.

#### **1.4 Objectives**

The primary objective of our study is to experimentally explore the competing roles of the numerous operating parameters that impact foam generation. These parameters include

- mass flow rates of air and surfactant solution,
- porous media within the foam generator,
- the length of the foam generator,
- the length of the foam transport pipe,
- pressure within the excavation chamber.

For this purpose, we have developed an experimental setup to mimic the foam generation system on an EPB-TBM. This setup allows us to control the operating parameters mentioned above, and study the foam properties. These properties are characterized by measuring,

- bubble size distribution (probability distribution function),
- foam stability,

- foam compressibility.

Presently, in the tunneling industry, a significant body of research and literature exists on soil conditioning [12], [13], [18]–[20]. However, very few studies have focused on the production of foam on an EPB-TBM. This opens up certain questions such as what are the important foam generation system characteristics, and how do the ground pressure conditions influence the foam generation and system design. A systematic study of the operating parameters and its influence on foam properties will help us understand the foam generation process on an EPB-TBM.

Generally, on a metro-size EPB-TBMs (cutterhead diameter = 6.5 to 7 m), large beads (6 mm), steel wool or perforated tubes are used as a porous medium in the foam generator for producing foam. However, different porous media can have varying effects on the foam properties. Also, the length of the foam transport pipe varies from 2 to 20 m on EPB-TBMs. These long pipes have a significant influence on the foam flow properties such as pressure drop, foam velocity and friction loss [21]–[26].

Similarly, the diameter of the foam transport pipe influence the flow properties of the foam, leading to variations in the foam properties such as bubble size and foam viscosity [27]. These are some of the key parameters that influence the foam flow properties. Our study addresses these issues, while our collaborators at the Underground Construction and Tunneling Center are studying the foam-soil behavior. This study will overall improve the tunneling process using an EPB-TBM by understanding the influence of operating parameters on the foam generation process, and foam properties.

## 2.1 Foams and Foam Stability

Aqueous foams consist of closely packed gas bubbles within a continuous liquid phase. Foams have a wide range of applications in food processing, cosmetics, textiles, metallurgy, fire-fighting, enhanced oil recovery and tunneling industry. Based on the foam generation technique, foam properties can be manipulated for different applications in various industries. Common foaming techniques include mechanical foaming, chemical foaming, and biological foaming. Mechanical foaming techniques include rotor-stator mixers, flow through porous media, gas sparging, whipping, wave-breaking and double syringe techniques [11], [28]–[31].

Foams are compressible non-Newtonian fluids with variable density and viscosity [32], [33]. The gas phase in foams is typically air, nitrogen, or carbon dioxide, and the liquid phase is typically water and surfactant. A surfactant is a surface-active agent that reduces the surface tension between the water and the gas, providing a better stability to the liquid films in foams [34], [35]. Figure 2.1 shows a 2-dimensional sketch of a general foam system. The foam structure consists of two-phase interfaces, lamellae, and plateau borders. The interfaces separate the gas phase from the thin liquid films. The lamella is a region that incorporates the thin film (liquid phase), and the two interfaces. The junction where three lamellae meet at an angle of  $120^\circ$  is referred as a plateau border [11].

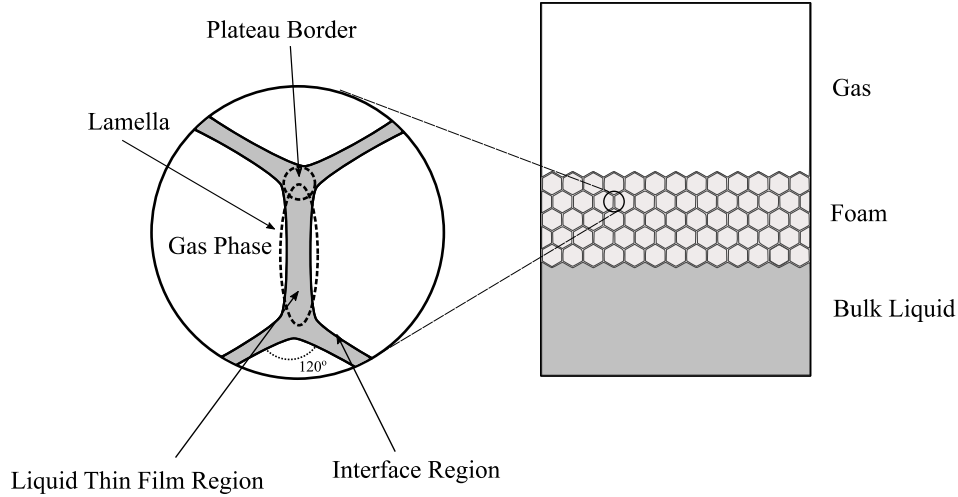


Figure 2.1 Microscopic view of the foam structure indicating the lamella, plateau border, and interface region. Image redrawn from *Emulsion, Foams, and Suspensions: Fundamentals and Applications* by Laurier L. Schramm.

To generate foam, there must be a certain mechanical work applied to the fluid to create bubble surface (interface), and a surface-active component (surfactant) to reduce the surface tension. Surface tension is the force acting on a liquid surface to minimize its surface area. Usually, the surfactant molecules adhere to the liquid surface, reducing the surface energy, and thereby aid in droplet or bubble formation of increased interfacial area, with a minimum input of mechanical energy. The surface energy is the energy expended to increase the surface of a phase, and it has a great influence on the stability and the structure of foams [11]. The Surface tension (interfacial tension) causes a pressure difference across the curved surfaces in a foam lamella, as shown in figure 2.2. If the pressure of the gas phase in a bubble is  $P_G$ , and pressure of the liquid in the interface is  $P_L$ , then the difference in the capillary pressure across the interface is given by the Young-Laplace equation,

$$\Delta P = P_G - P_L, \quad (2.1)$$

$$\Delta P = \gamma \left( \frac{1}{R_1} + \frac{1}{R_2} \right)$$

where  $\gamma$  is the surface tension,  $R_1$  and  $R_2$  are the radii of curvature.

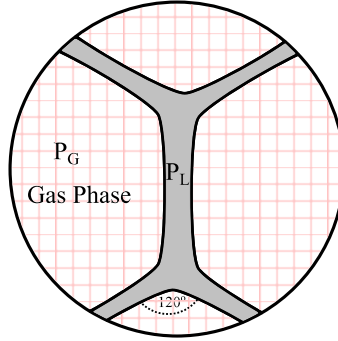


Figure 2.2 Internal pressure inside a bubble  $P_G$  and the partial pressure of liquid  $P_L$ .

Foams are often characterized using a foam expansion ratio (FER) defined as,

$$\text{FER} = \frac{\text{Vol}_A + \text{Vol}_L}{\text{Vol}_L}, \quad (2.2)$$

where,  $\text{Vol}_A$  and  $\text{Vol}_L$  are the volumes of air and liquid respectively, in the foam. Higher values of FER indicate dry foam due to a large volume of air, while lower values of FER indicate wet foam due to a small volume of air. Note that we can represent FER in terms of air and liquid flow rates [10].

$$\text{FER} = \frac{Q_A + Q_L}{Q_L}, \quad (2.3)$$

The term “foam texture” is often used to refer to the shape, size, and distribution of bubbles. It describes the distribution of gas bubbles throughout the liquid phase in foams. Foam texture is affected by numerous factors including FER, pressure, foam generation method, and the chemical composition of the surfactant. For example, it is observed that small bubbles increase the foam

viscosity. Overall, the texture affects the rheology of foam and governs the foam stability [7], [11], [30], [32], [36].

The “stability” of a foam is its capacity to resist bubble rupture. Foam stability accounts for two main things; one is drainage of liquid from the foam and another is a coalescence of smaller bubbles into larger bubbles. Both these characteristics cause the foam to degrade. The coalescence of smaller bubbles into a large bubble is mainly due to the internal pressure difference between two adjacent bubbles. This pressure difference leads to the inter-bubble diffusion causing the large bubbles to grow larger and leading to thinning of liquid films, which eventually degrades the foam [11], [32], [37]. Foam drainage, on the other hand, refers to the draining of liquid from the thin films of the foam due to gravity. It is usually quantified in terms of half-life, which is the time required for the liquid volume to decrease to one-half of the original foam volume. The longer it takes the liquid to drain from the foam, the higher is the foam stability [1].

## **2.2 Foam Rheology**

Rheology is the branch of physics that deals with the deformation and flow of matter, especially the non-Newtonian flow of liquids and the plastic flow of solids. Rheology attempts to understand the structural changes in a fluid when it is subjected to shear stress. Foams are classified as non-Newtonian fluids that tend to slip on the walls of a smooth surface as they flow. One important parameter describing foam rheology is its effective viscosity. Typically, foam viscosity is much higher than the viscosity of its constituent fluids. Foams also exhibit pseudoplastic or Bingham plastic behavior, as shown in figure 2.3. Pseudoplastic fluids show a decrease in viscosity with an increase in shear stress. Bingham plastic fluids are fluids that have an initial yield stress and they behave as solids below a certain yield stress [38].

Pseudoplastic fluids are often described using the Ostwald–de Waele power-law fluid model,

$$\tau = K \left( \frac{dV}{dy} \right)^n, \quad (2.4)$$

where  $\tau$  is the shear stress,  $K$  is the consistency index (effective fluid viscosity),  $\frac{dV}{dy}$  is the shear rate and  $n$  is the flow behavior index. For pseudoplastic fluids, the flow behavior index is less than one ( $n < 1$ ).

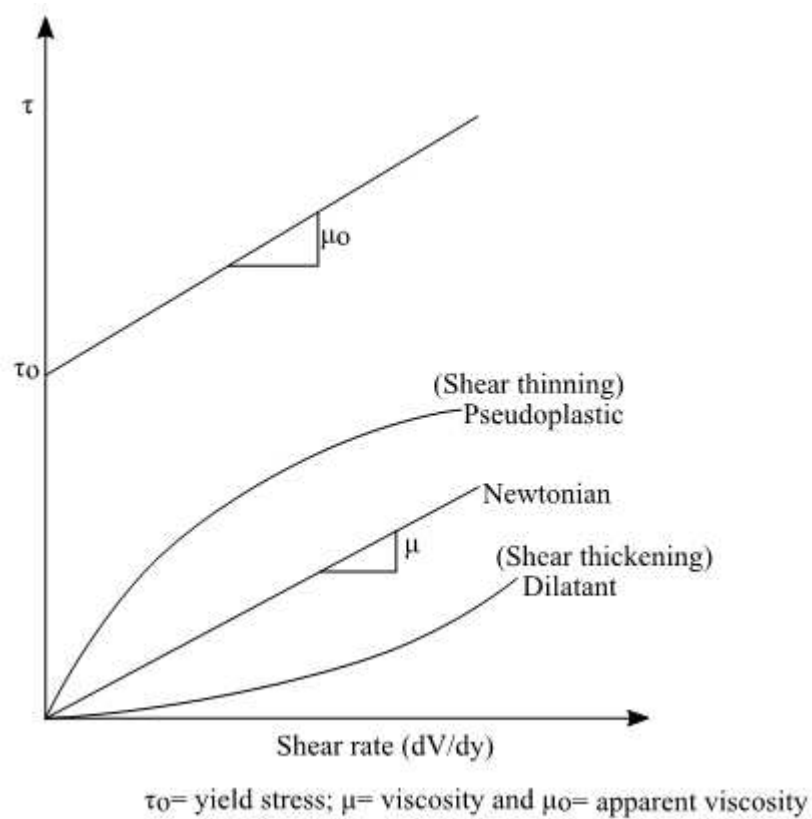


Figure 2.3 Classification of different fluids based on the shear stress ( $\tau$ ) and shear rate plots

Similarly, Bingham plastic fluids can be described by the equation 2.5

$$\tau = \tau_0 + \mu_0 \frac{dV}{dy}, \quad (2.5)$$

where,  $\tau_0$  is the yield stress, and  $\mu_0$  is the apparent fluid viscosity [22], [39], [40]. Foam can also be modeled as Herschel-Bulkley model [41], [42].

Numerous studies have explored the complex rheology of foams. Sibree [43], Blackman [44], Grove [45], and Raza [46] studied foam rheology by measuring foam viscosity using various types of viscometers. Sibree, Blackman and Raza [43], [44], [46] showed that foam viscosity decreases with shear rate, while Grove [45] observed that viscosity remained constant with shear rate. Their results indicated that for the same type of foam, different types of viscometers give different results that have led to some confusion in this field. However, these studies did not take into account the slip and foam compressibility in their analysis. Mooney [47] developed correlations to determine wall slip and viscosity of non-Newtonian fluids as functions of experimental quantities obtained from capillary and rotating cylinder viscometer. Later, these correlations were used in various studies that included the slip and viscosity in their analysis.

Wenzel et al. [21] showed that foams show a pseudoplastic behavior as they flow through pipes. Wenzel et al. were the first to report that foam flows on a thin liquid layer through pipes, provided that the shear stress at the walls is less than the yield stress. If the shear stress exceeds the yield stress, velocity gradients develop that contribute to the average foam velocity.

Later, David and Marsden [48] extended the work of Raza et al. to develop equations for foam flow through capillary tubes by including slip and compressibility. They observed that the apparent foam viscosity is independent of FER, which contradicts to the results observed by Raza et al. The authors agreed with Raza et al. that foam behaves as a pseudoplastic fluid showing a parabolic velocity profile at low flow rates, and a plug flow at higher flow rates, as shown in figure 2.4. Wenzel et al. [49] also studied the viscosity of foams using various viscometers and observed similar conclusions to those of David & Marsden.

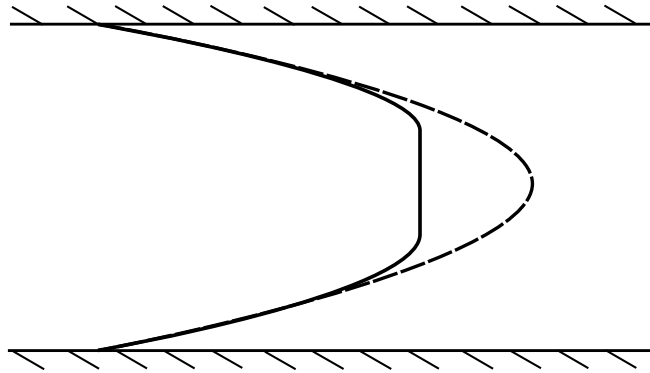


Figure 2.4 Plot showing velocity profiles for foam flow through circular tubes of different diameter. Parabolic profile is observed at low flow rate (dashed line), and plug-like flow at a high flow rate (solid line). Image is a qualitative representation from David & Marsden (1969)

Calvert and Nezhati (1986) also studied the rheology of foam by performing experiments using a cone and plate rheometer. They found that foams can be modeled using the modified Bingham plastic model,

$$\gamma = \left( \frac{\tau - \tau_y}{K} \right)^{1/n}, \quad (2.6)$$

where  $\gamma$  is the shear rate,  $\tau$  is the shear stress,  $\tau_y$  is the yield stress,  $n$  is flow behavior index and  $K$  is the consistency. For their modified Bingham plastic model, the authors assumed that there is a liquid rich layer at a solid surface due to bubble migration. Figure 2.5 shows the flow region through a cone and plate rheometer, and through a pipe. Three regions are observed. Region A is the Newtonian slip layer. Region B is unsheared foam. Region C is sheared foam. Their experimental results showed that the slip layer thickness depends on the FER and the foam flow rate.

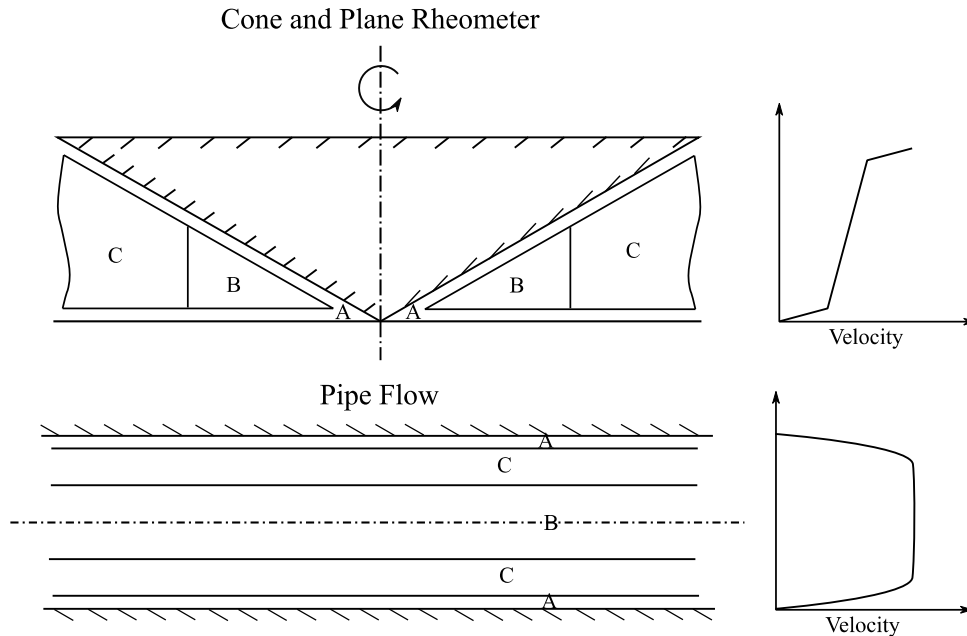


Figure 2.5 Flow regions through the cone and plane rheometer and pipe flow. Region A - Newtonian slip layer, region B - unsheared foam and region C - sheared foam. Image redrawn from Calvert 1986.

### 2.3 Foam flow through pipes

Foam flows through pipes have been extensively investigated by many authors [22], [23], [25], [26], [49]–[53]. Some studies focused on understanding the foam rheology in pipes and valves, while some studies looked upon the pressure drop and flow regimes for foam flow through pipes. Pressure drop for two-phase flows (air and water) could be computed with Lockhart-Martinelli correlation. However, this correlation does not accurately predict the pressure drop for foam flow through pipes. Hence, different models have been developed to compute the pressure drop for foam flow through pipes because [22], [51], [53].

Wenzel et al. [21] studied the flow of high expansion foams for FER range of 50 to 300. They were the first to observe a liquid rich layer on which foam flows through pipes, which was corroborated in various subsequent studies [23], [40], [52], [53]. Their experiments were

performed using a circular pipe of diameter 70 mm, three rectangular ducts of height 25.4 mm, and three different widths. They observed a non-linear relationship between pressure drop and average velocity for foams characterized by varying mean bubble diameters of <1-8 mm. They also observed that the pressure drop per unit length for a given velocity is an inverse function of average bubble diameter of foam.

Blauer et al. (1974) used a Reynolds number ( $Re_f$ ) and a fanning friction factor ( $f_f$ ) to determine the friction losses for foam flows through pipes. The authors modeled foam as a single-phase fluid having an effective foam viscosity, average velocity, and foam density to determine the  $Re_f$  and  $f_f$ . The authors developed a Moody diagram from their  $Re_f$  and  $f_f$  data on which the critical Reynolds number for the transition was evident. However, their study did not clearly indicate the method to determine the friction factor and Reynolds number. Also, it was unclear how they derived their correlation for effective foam viscosity.

Lemlich and Thondavadi (1985) reported similar results as Wenzel et al. [21], and David and Marsden [48] for foam flows through pipes. They concluded that the liquid slip layer increases with the shearing of the flow. The bubble ruptures due to the shearing of the flow and more liquid is dragged near the wall resulting in an increased thickness of the liquid layer.

Calvert (1990) investigated the pressure drop for foam flow through pipes and compared them with a plug flow model and Calvert-Nezhati (C-N) model. The author developed the C-N model using the Herschel-Bulkley law to determine the pressure drop. A major difference between the two models was the C-N model accounts for the compressibility effects of foam and it assumes that the pressure drop is not proportional to the flow rate due to the isothermal expansion of bubbles. Calvert observed that the plug-flow model was inaccurate to predict the pressure drop if

wall shear stress exceeds the yield stress. The C-N model predicted the pressure drop accurately within a factor of two.

Briceno and Joseph [52] studied the transport of aqueous foams in horizontal conduits. The authors experimentally investigated the formation of a lubricating liquid layer for foam flow through pipes and channels. For all the tests, the authors made sure that there was a low pressure drop (<20 kPa) for foam flow through the pipes/channels. They reported seven flow patterns for different FERs. For FER range of 10 to 33, a plug flow pattern was observed in which the foam flowed as a rigid plug on a thin lubricating layer. At FER >33 the plug flow transitions to a slug flow pattern, where the foam bubbles grow and eventually coalesce to create large air pockets. Based on their experimental data on pressure drop and foam flow rates, the authors computed the friction factor and Reynolds number using the mixture velocity, hydraulic diameter, liquid density, and viscosity. The authors plotted the Reynolds number and friction factor on a log-log plot and obtained as,

$$f_f = \frac{3700}{Re_f^{1.03}} \quad (2.7)$$

Comparing equation 2.7 with the relation of friction factor and Reynolds number for a single phase Newtonian fluid shown in equation 2.8, it was observed that the numerator in equation 2.7 was

$$f = \frac{16}{Re} \quad (2.8)$$

200 times larger than that of a Newtonian liquid. This indicated that there was a huge increase in the friction due to the lubricating layer.

## 2.4 Bubble Size Analysis

The influence of foam bubble size has been widely studied [21], [23], [37], [48], [49]. Wenzel et al. studied the effect of the bubble size for foam flow through pipes. The authors observed that the bubble size was an important parameter that influenced the pressure loss through the pipes at a given average foam velocity. They concluded that the pressure loss for a given average foam velocity is an inverse function of the average bubble diameter. A preliminary study showed that, as foam moved along the pipe, the foam bubbles near the walls undergo high shear and become progressively smaller. While the foam bubbles at the center are under low shear and remain their original size.

David & Marsden (1969) investigated the bubble size and bubble size distribution by measuring the foam bubbles using a microscope. Their bubble size distributions were found to be a good fit with a Weibull distribution. The distributions also indicated that, with an increase in FER, the average bubble diameter, and the range of the bubble size increased. The bubble diameter increases with FER because with an increase in FER the volume of air increases, leading to larger bubbles. However, their bubble size analysis results are not promising as they have not considered smaller bubbles whose diameter was less than 0.16 mm.

Lemlich et al. [23], [37] predicted the changes in the bubble diameter over time due to inter-bubble diffusion using De Vries' extended model of bubble size distribution. Based on the theory by De Vries, the pressure within the bubbles was considered as the driving force for diffusion. However, according to Lemlich's theory, diffusion at first occurs between each bubble and liquid. Based on this theory, Lemlich et al. modified De Vries' equation for the study. The authors observed that the distribution becomes wider, the height of the peaks decrease, and both

distribution and peaks shift towards larger radii. This indicates that inter-bubble diffusion leads to decrement in the number of bubbles, and shifting of bubble size towards a larger average diameter.

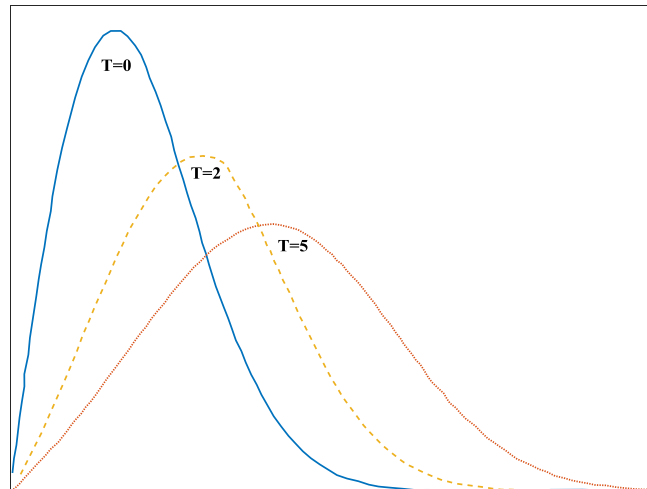


Figure 2.6 Bubble frequency distribution with respect to average bubble diameter for foam drainage at various time. Qualitative plot is redrawn from Lemlich et al. (1985)

## 2.5 Flow through porous media

Fluid flow through porous media has a wide range of applications such as oil extraction, catalytic converters, filters, chemical reactors, storing nuclear wastes, geothermal systems, and biomedical application. Flow in porous media is complicated as the fluid must travel through the tortuous passages created due to the obstruction by the solid structures. These obstructions lead to significant pressure drops across the porous medium. Hence, it is important to study the different flow regimes and the pressure drops through porous media as they are critical for these applications.

In 1856, Henry Darcy experimentally studied the flow of water through packed beds of sand and derived a correlation for the volumetric flow rate ( $Q$ ) of the fluid through the porous medium,

$$Q = -KA \frac{\Delta P}{L}, \quad (2.9)$$

where  $K$  is the hydraulic conductivity,  $A$  is the cross-sectional area of the flow,  $\Delta P$  is the pressure drop, and  $L$  is the length of the porous medium over which the pressure drop takes place. Darcy's equation did not account for fluid viscosity. The Hazen-Darcy equation takes fluid viscosity into account and hence for fluid flow through homogeneous porous medium, the Darcy's Law can be represented in a different manner as,

$$v = - \frac{k}{\mu} \nabla p, \quad (2.10)$$

where  $k$  is the permeability of the porous medium,  $\mu$  is the fluid dynamic viscosity,  $v$  is the average fluid velocity through the porous medium, also referred to as the Darcy velocity. The permeability of the porous medium is the measure of the resistance to the flow. A large value of permeability indicates that fluid can flow easily through a porous medium. The Darcy's law is valid only for incompressible, Newtonian, isothermal, creeping flow (low speed) through porous media. In the Darcy regime, the pressure drop (energy dissipation) across the porous media is solely due to the viscous drag of the flow over the solid surface.

At higher flow velocities, the energy dissipation occurs due to both viscous and inertial drag. A quadratic term is added to Darcy's law in equation 2.10 to account for the inertial effects. This equation is generally referred as the Forchheimer equation and it is defined as,

$$0 = \frac{\Delta p}{\Delta L} - \frac{\mu}{K} v - C \rho v^2, \quad (2.11)$$

where  $\rho$  is the fluid density and  $C$  is the Forchheimer coefficient (form coefficient related to the geometry of the [54]). The fluid flow regime is called the Forchheimer Regime. The quadratic term ( $C\rho v^2$ ) is the form/inertia force on the fluid due to obstruction of flow by a solid surface at higher

flow velocities. It should be noted that the flow is still laminar for both the Darcy and Forchheimer regimes.

## 2.6 Mechanism of foam generation through porous media

Foam generation through porous media can be understood by studying the pore level events for foam formation. Various studies suggested two fundamental pore-level mechanisms for foam generation [55]–[59]. Ranshoff and Radke [55] have experimentally shown that foams can be generated by two dominant mechanisms, snap-off, and lamella division, as shown in figure 2.7. Figure 2.7(a) illustrates that, as the gas-bubble flows through the constriction of the porous medium, it expands as it comes out of the downstream side. This causes a decrease in the capillary pressure across the neck of the constriction, leading to a pressure gradient in the liquid phase. As a result, liquid flows into the neck of the constriction that eventually leads to snaps off a gas bubble. Figure 2.7(b) shows the secondary foam generation mechanism - lamella division. In this mechanism, a moving lamella flows through the constrictions and divides itself to form bubbles.

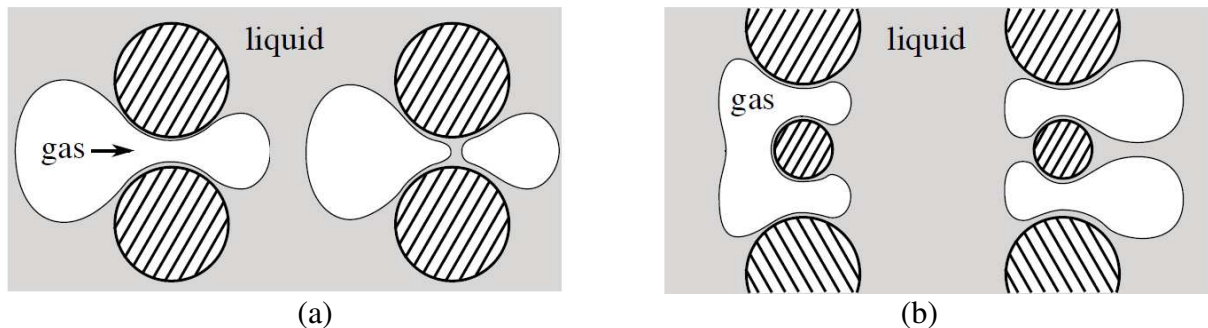


Figure 2.7 Mechanism of foam generation through porous media: (a) snap-off (b) lamella division

Ranshoff and Radke [55] studied the influence of gas velocity for foam generation in bead packs. They reported a critical capillary number in homogenous porous media above which snap-off and lamella division becomes dominant foam generation mechanism. Friedmann and Jensen

[60] studied foam generation using different porous media and observed that higher air-liquid flow rates produced smaller and uniform bubbles. Rossen and Gauglitz [61] concluded from their study that a minimum pressure gradient is required to generate foam.

We developed an experimental setup that replicates similar conditions to those on an EPB-TBM. The foam is generated by flowing a mixture of pressurized air and surfactant solution through a tube with packed beads. The foam then flows through a transport pipe into a pressure chamber. The chamber mimics the pressure conditions experienced at the cutterhead of an EPB-TBM. To study the influence of operating parameters on foam bubble size distribution, we developed a device to capture the foam and photograph the bubbles using a microscope. The foam bubbles can be captured at pressures equivalent to those at the outlet of the foam generator, at different locations in the foam transport pipe, and at the inlet of the pressure chamber.

Our experimental setup allows us to:

- investigate the influence of air and liquid mass flow rates on foam generation,
- vary the influence of the length of the foam generator,
- vary the porous medium within the generator,
- consider different lengths and diameters of the foam transport pipe carrying foam from the generator to the pressure chamber,
- vary the pressure in the chamber between 1 to 5 bar.

### **3.1 Laboratory-Scale Foam Generation System**

Figure 3.1 shows a schematic of our laboratory-scale foam generation system. This set-up is a small-scale replica of foam generation and transport on an EPB-TBM. The system can be divided into four subsystems, as labeled in the schematic. The “flow control system” supplies a controlled mass flow rate of air and surfactant solution to the foam generator. The two-phase

mixture then flows through a foam generator consisting of a tube packed with beads. The foam then flows through a transport pipe into a pressure chamber maintained at a fixed pressure. Furthermore, the foam is bled-off at the outlet of the foam generator, and the inlet of the pressure chamber, into a ‘foam capture device’ to take photographs of the bubbles using a microscope. The pipe material used for connections in the experimental setup is polyurethane with 6.3 mm inner diameter.

### **3.1.1 Foam Generator**

Foams are generated by flowing a two-phase mixture of surfactant solution and air through an acrylic tube (15.2 mm diameter) filled with randomly packed soda-lime beads, as shown in figure 3.2. In this study, we consider three different bead diameters - 1, 2, and 3 mm. We also consider three lengths of foam generators - 110, 200 and 400 mm. Controlled mass flow rates of air ( $\dot{m}_A$ ) and liquid surfactant solution ( $\dot{m}_L$ ) enter the foam generator through the wye-connector on the right of the figure. As the mixture flows through the porous medium, foam is created due to mixing generated by the pore geometry and possibly turbulence. As the two-phase mixture flows through the porous material, the pore geometry of the beads causes the liquid-gas interface to stretch, causing the fluid to snap-off and create bubbles. As these bubbles move through the tortuous paths of the porous material, they further breakdown into smaller bubbles.

At the inlet and the outlet of the foam generator, two OMEGA pressure transducers measure effective inlet /outlet pressures of the two-phase mixture. The pressure transducers are connected to a data acquisition system, and the measurements are monitored using LabVIEW.

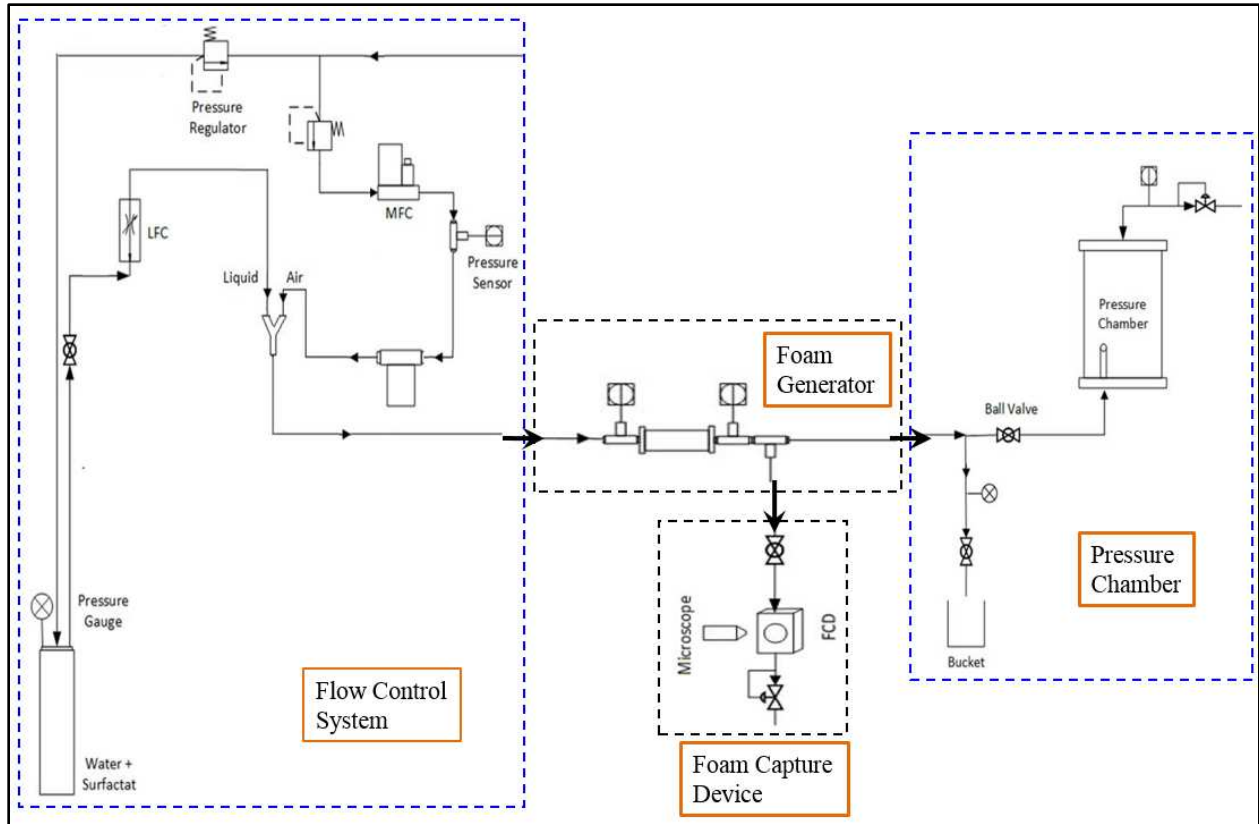


Figure 3.1 Schematic of the laboratory foam generation system and foam testing device. Not to scale. The FCD can be used to photograph the foam bubbles at the outlet of foam generator, and at the inlet of the pressure chamber

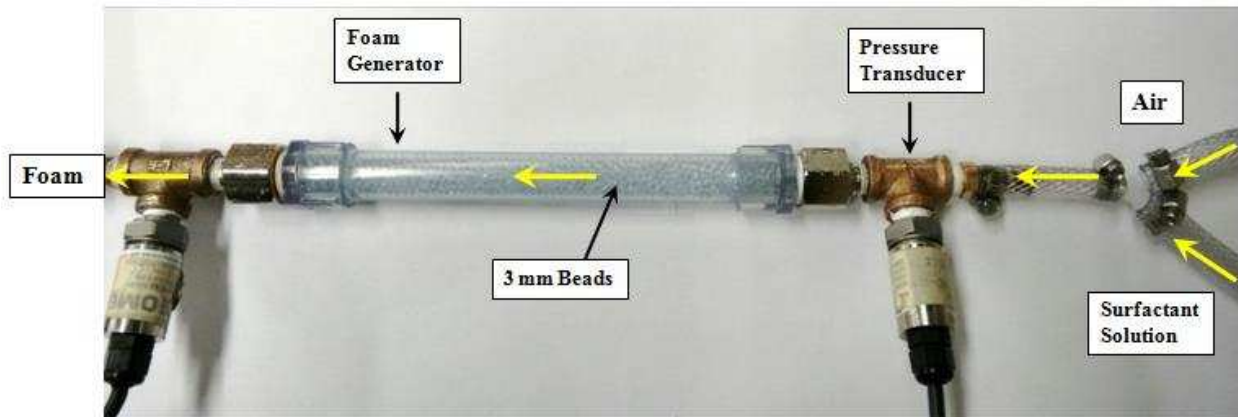


Figure 3.2 Foam generator filled with 3 mm beads. The length of the foam generator is 200 mm and the diameter is 15.2 mm

### 3.1.2 Flow Control System

The flow of the liquid and air through the generator and the transport pipe are driven by compressed air at 11 bar. Figure 3.3 shows that the compressed air is channeled to the air mass flow controller and the storage tank containing surfactant solution. An AALBORG mass flow controller supplies a controlled mass flow rate of air to the foam generator. Simultaneously, compressed air is used to pump the surfactant solution from the storage tank and an OMEGA liquid flow controller sets the mass flow rate of the surfactant solution. The air mass flow controller provides flow rates from 0 - 50 slpm (standard liters per minute) and the liquid flow controller provides from 0.26 to 2.5 slpm. In this study, we report the flow rates of air and liquid in terms of an equivalent volumetric flow rate  $Q_{\text{air}}$  (slpm), at standard temperature (21° C) and standard atmospheric pressure (101.3 kPa). The air mass flow controller is connected to a data acquisition system and the flow rates can be controlled and monitored using LabVIEW interface. Pressure controllers are used to regulate the pressure of the compressed air to the mass flow controller as well as to the storage tank.

### 3.1.3 Pressure Chamber

A pressure chamber was designed in-house to replicate the pressures encountered on a tunneling site, where the foam is injected through the cutterhead of a tunnel boring machine. The absolute pressure in the cutterhead typically varies between 2 to 5 bar. Figure 3.4 shows the pressure chamber. The foam enters through the bottom of the chamber and a measuring tape is attached to measure the height of the foam in the chamber. Compressed air is supplied from the top of the chamber, and a pressure gauge monitors the chamber pressure. A regulator back pressure is also connected at the top of the pressure chamber to maintain a desired pressure as foam fills

the chamber. In our study, we injected foam under 1, 3 and 5 bar pressure. The procedure for carrying out the pressure chamber test is given in appendix A.

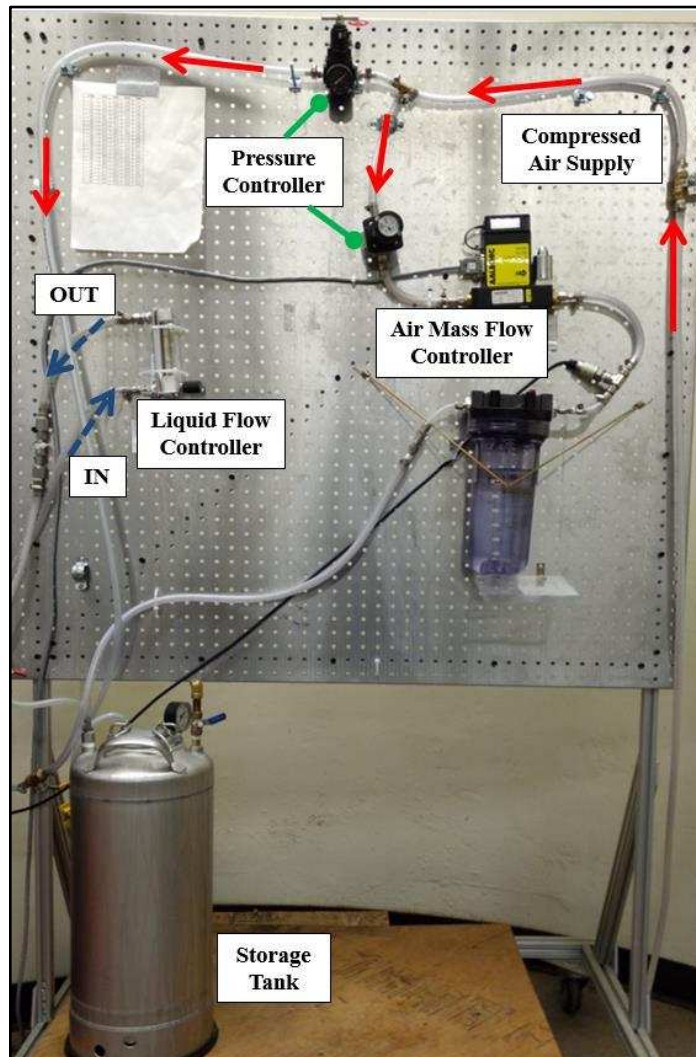


Figure 3.3 Mass flow controllers for air and surfactant solution. The solid arrows show flow of air supply and the dotted arrows indicate inlet & outlet of surfactant solution

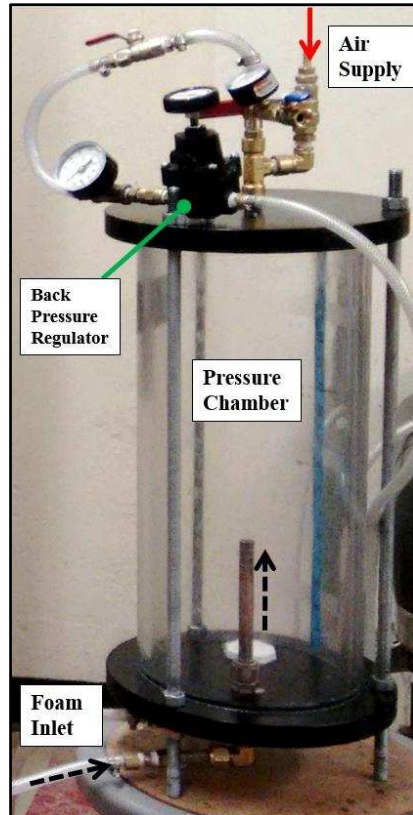


Figure 3.4 Pressure chamber setup to conduct experiments under pressure up to 5 bar. The solid arrow shows compressed air supply, and dotted arrows show foam flow. A back pressure regulator connected with a pressure gauge is placed in the top of the pressure chamber

### 3.1.4 Bubble Size Measurement

Foam bubble size (bubble diameter) is an important foam property that influences soil conditioning, stability and drainage of foam, and foam flow through the transport pipe. Figure 3.5 shows our setup for the foam capture device (FCD) used in our experiments. The foam is captured at the outlet of the foam generator using a ball valve to bleed off the foam into the foam capture device. An OMEGA back pressure regulator (BPR) is used to control the flow through the device and maintain the pressure in the FCD. The pressure is maintained equivalent to that at the outlet of the foam generator. A pressure sensor is connected to the back pressure regulator which is

monitored using the LabVIEW interface. In a similar manner, we also capture the foam bubbles at the inlet of the pressure chamber.

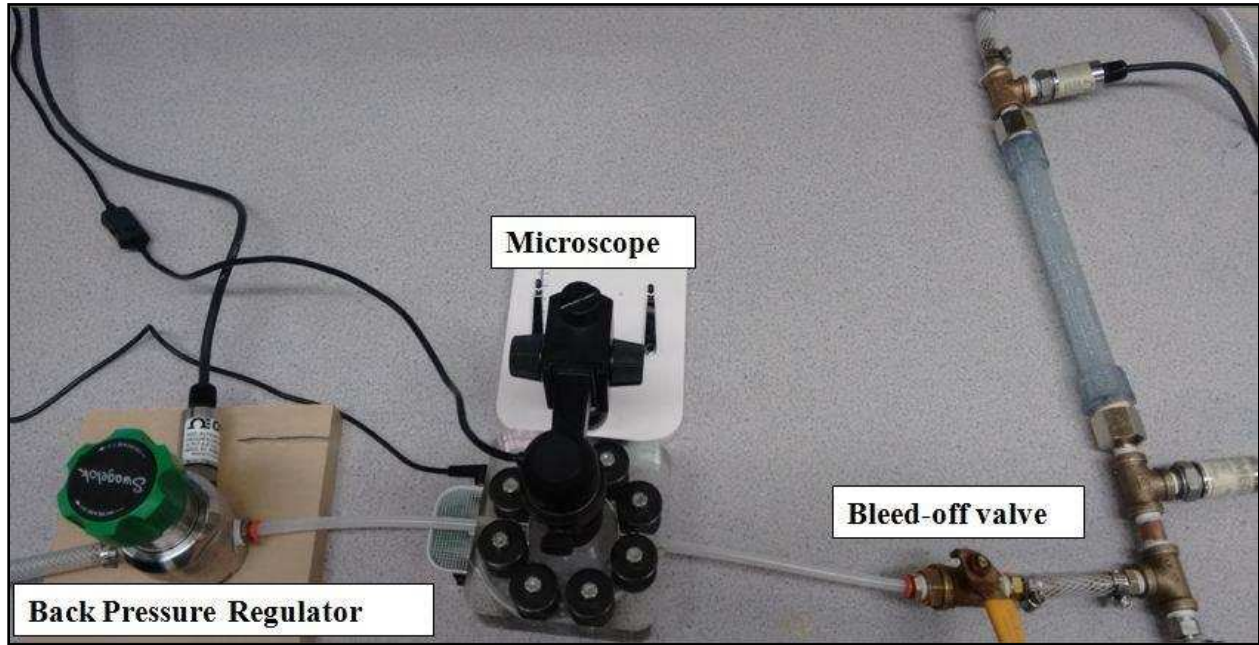


Figure 3.5 Set-up for photographing foam bubbles using a bleed-off valve, a foam capture device, a microscope and a back pressure regulator

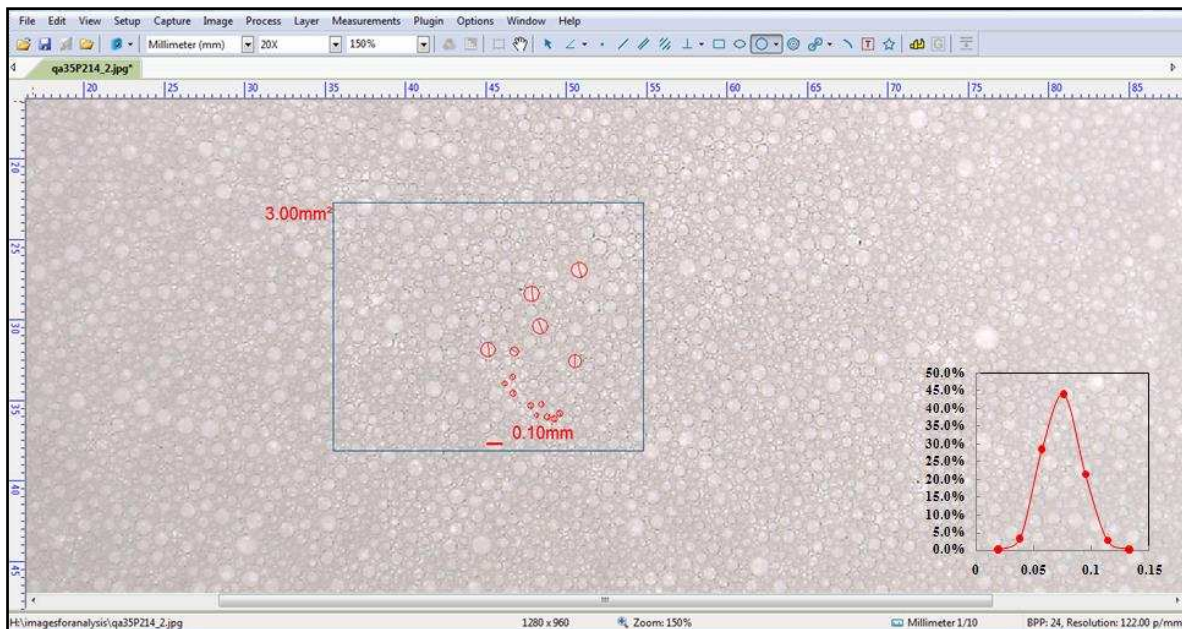


Figure 3.6 Screenshot of image analysis of foam bubbles using AmScope software.

Figure 3.6 shows the image analysis of the foam bubbles using AmScope software. The analysis is done manually by counting 700 bubbles from a certain region and the data is then exported to Excel, to determine the average bubble diameter and bubble size distribution for a given image. A detailed description of the procedure is provided in the appendix A.

### 3.2 Foam Compressibility

Foam compressibility is the measure of change in foam volume from its initial volume, due to increase in pressure. Figure 3.7 shows the setup to perform the foam compressibility test. Foam is injected at the bottom of the pressure chamber up to a certain height of the chamber ranging from 38 to 40 cm. The pressure chamber is maintained under 1, 3, and 5 bar absolute pressure using a back pressure regulator. The test is performed by loading and unloading of foam using the air pressure at 1 bar that is provided from the main supply line. The supply air pressure is monitored using a pressure gauge. The loading and unloading time duration is approximately 30 seconds.

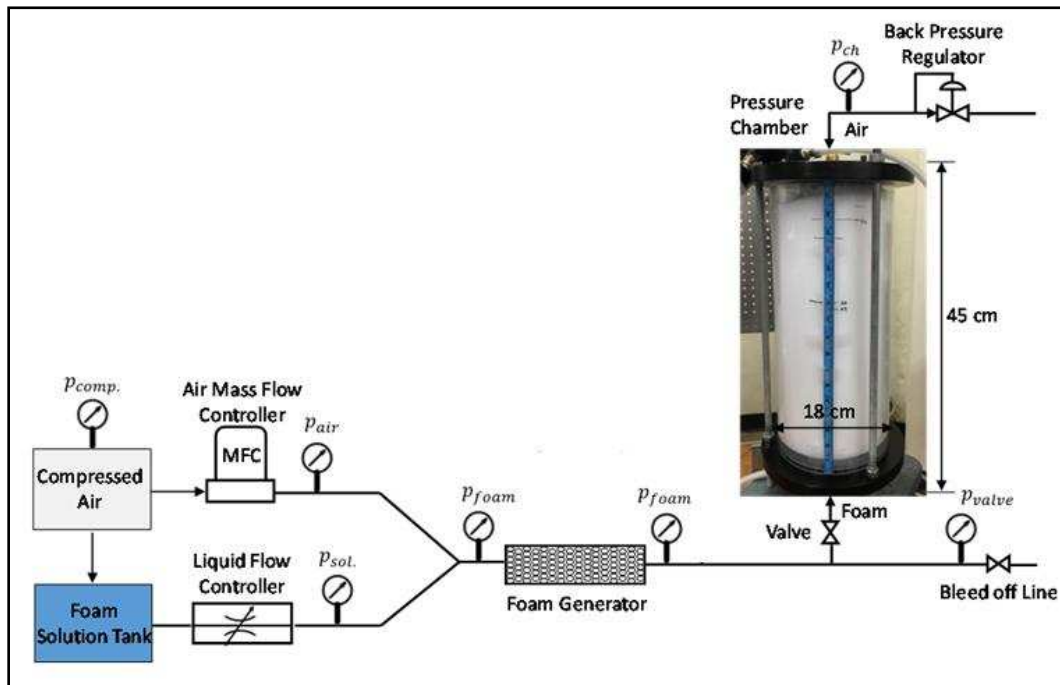


Figure 3.7 Setup of the foam generation system to inject foam into the pressure chamber for the foam compressibility and drainage tests.

The measurements of foam heights are taken every five minutes beginning from time zero up to 30 minutes. The foam height is multiplied by the cross-sectional area of the pressure chamber to obtain the volume of foam. The initial foam volume before loading ( $V_{\text{foam},i}$ ), and final foam volume after loading ( $V_{\text{foam},f}$ ) are shown in the schematic in figure 3.8. The foam compressibility ( $C_{\text{foam}}$ ) is quantified in terms of percentage and it is defined as,

$$C_{\text{foam}} = \left( \frac{V_{\text{foam},i} - V_{\text{foam},f}}{V_{\text{foam},i}} \right) \times 100\%. \quad (3.1)$$

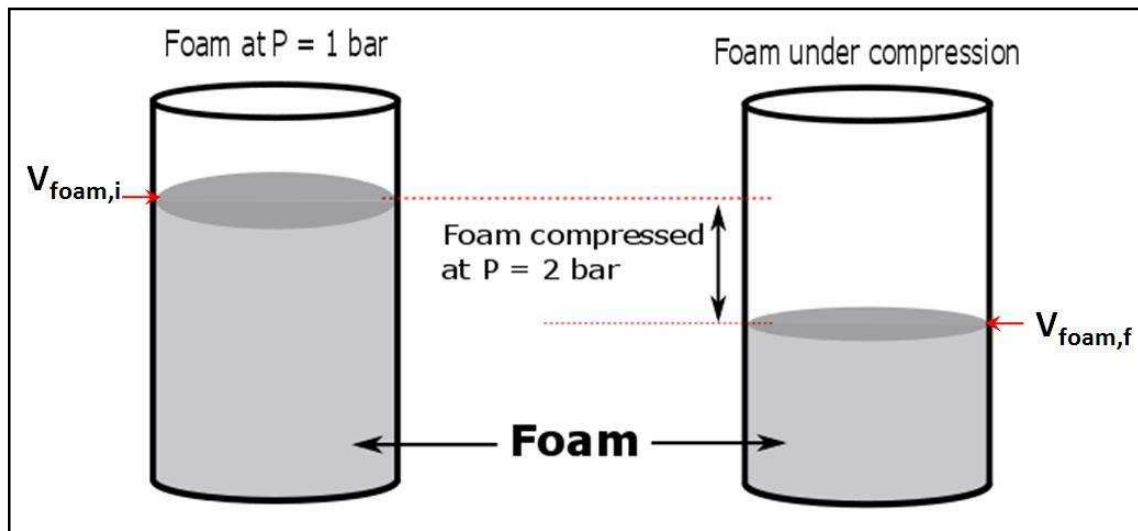


Figure 3.8 Schematic, not to scale, of foam compressibility

### 3.3 Foam Drainage

Foam stability is measured in terms of liquid drainage from the foam with time [1]. As per the guidelines established by EFNARC, the foam drainage is measured in terms of half-life using the funnel test shown in figure 3.9. Half-life is defined as the time required for the foam to lose one-half of its initial liquid mass due to drainage [9]. The funnel test is done under atmospheric conditions, and the liquid volume and time are noted when half of the liquid is drained from the

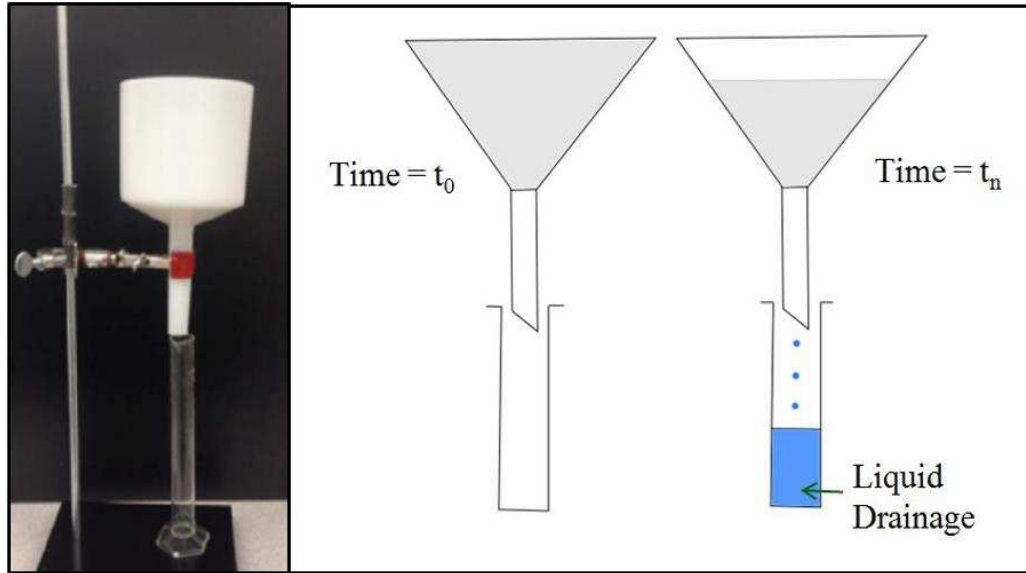


Figure 3.9 Funnel test to determine stability (half-life) of foam

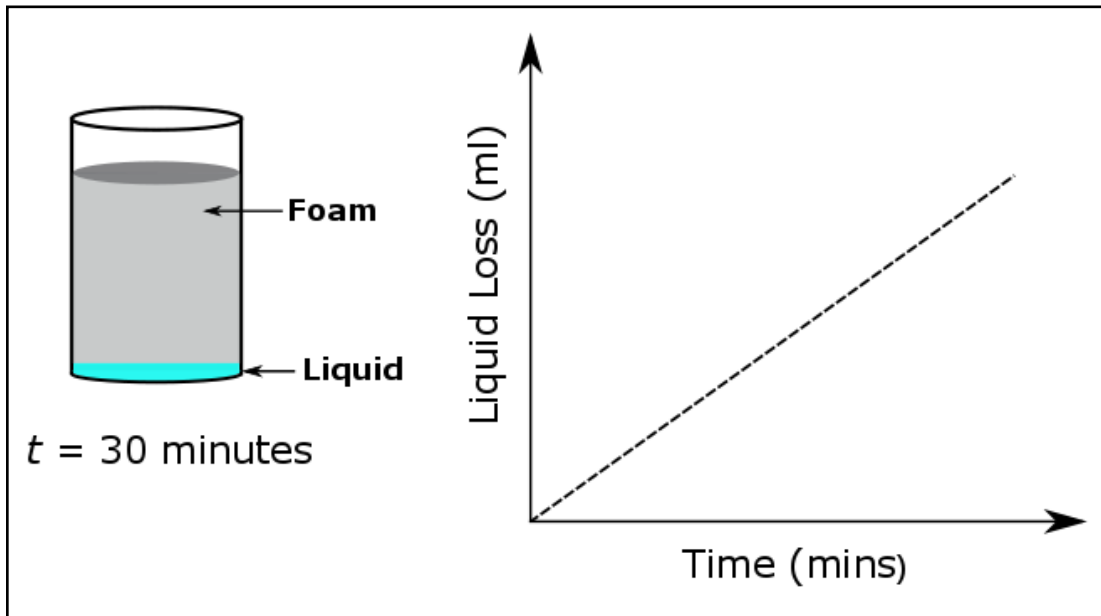


Figure 3.10 Schematic, not to scale, of liquid drainage from the foam over time

foam. In our study, we measure the liquid drainage in a unique way by taking into account the influence of the pressure in the excavation chamber. The foam drainage test is performed in a similar way as foam compressibility using the setup shown in figure 3.7. The liquid loss at the bottom of the chamber recorded using a measuring tape attached to the chamber after every cycle of loading and unloading. Five cycles are performed for a total time duration of 30 minutes. The liquid loss measurements are taken before loading and after unloading the pressure. Figure 3.10 shows a schematic of liquid volume loss at time  $t = 30$  minutes and a qualitative plot of liquid volume loss with time. The plot shows that liquid loss from the foam increases with time.

## CHAPTER 4 RESULTS AND DISCUSSION: FLOW CHARACTERIZATION

In this study, there are three major sets of experiments. In the first, we removed the pressure chamber and transported the foam through the transport pipe into an open bucket at atmospheric conditions. This greatly simplified the study because the experimental protocol for the chamber is complicated and requires at least two people. For this setup, we systematically explored the influence of bead diameter, the length of foam generator, and length of foam transport pipe. We performed all the tests by fixing the surfactant concentration to 5 % SLF50, the inner diameter of transport pipe to 6.3 mm and FER to 15. We considered three bead diameters (1, 2, and 3 mm), three lengths of foam generator (110, 200, and 400 mm), and three lengths of foam transport pipe (1, 3, and 5 m).

In the second set of experiments, we fixed the bead diameter to 3 mm, the length of foam generator to 200 mm, and the length of the foam transport pipe to 1 m. We included the pressure chamber to explore its influence on flow parameters and foam properties. We repeated the tests for chamber pressures of 1, 3, and 5 bar (absolute). The FER, surfactant concentration, the inner diameter of transport pipe and diameter of the foam generator were identical to the first set of experiments.

In the final set of experiments, we explored the role of the transport pipe diameter for chamber pressures of 1 and 3 bar. We considered the pipe diameters as 6.3, 9.5 and 12.7 mm. All other parameters were fixed as in the first set of experiments.

#### 4.1 Characterization of Pressure and Foam Flow Velocity

Figure 4.1 shows a sketch of a foam generator. To investigate the physics of foam generation, we must characterize the pressure and velocity of the liquid and gas phases within the generator. We measure pressure at the inlet ( $P_{in}$ ) and outlet ( $P_{out}$ ) of the foam generator as shown in figure 4.1. Though surface tension effects do lead to pressure differences between the gas and liquid phases, we interpret the pressure measured by the gages as an effective mixture pressure. We compute the air density using this effective pressure. Throughout our study, we report the pressure  $P$  in absolute units, where atmospheric pressure is taken as  $P_{atm} = 101.3$  kPa. Though our experiments are performed at an elevation of 1,730 m (5,675 feet), the atmospheric pressure in our lab facility deviated little from the standard value.

Based on the literature for multiphase flow and flow through porous media [54], [62]–[64], we characterize the velocity of each phase using superficial velocities defined as,

$$V_{air} = \frac{\dot{m}_{air}}{\rho_{air}A_G}, \quad V_{liq} = \frac{\dot{m}_{liq}}{\rho_{liq}A_G}, \quad (4.1)$$

where,  $\dot{m}$  is the mass flow rate of the fluid (kg/s),  $\rho$ (kg/m<sup>3</sup>) is the density of the fluid considering compressibility effects at pressure, and  $A_G$  is the cross-sectional area of the foam generator (m<sup>2</sup>) (i.e.  $\pi r^2$ ).

To compute  $V_{liq}$ , we assume the solution of water and surfactant is incompressible. We measured the density of the liquid solution and found it equal to that of water, 1000 kg/m<sup>3</sup>. Due to the large pressure variations in our system, the variations in air density are significant. We assume isothermal conditions to compute the air density using the ideal gas law.

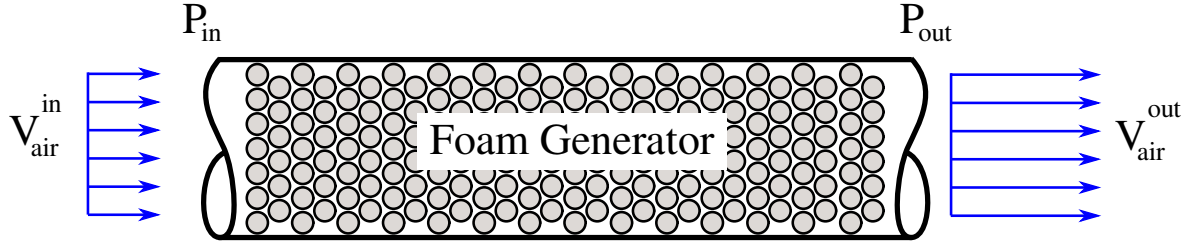


Figure 4.1 Sketch, not to scale, of the foam generator filled with beads.

In addition to the superficial velocities  $V_{air}$  and  $V_{liq}$ , we compute an effective mixture velocity defined as

$$V_{mix} = \frac{\dot{m}_{air} + \dot{m}_{liq}}{\rho_{mix}}, \quad (4.2)$$

where  $\rho_{mix}$  is an effective density, computed as

$$\rho_{mix} = \frac{\rho_{air} * V_{air} + \rho_{liq} * V_{liq}}{V_{air} + V_{liq}}. \quad (4.3)$$

One can show that the mixture velocity is simply the sum of the superficial air and liquid velocities,  $V_{mix} = V_{air} + V_{liq}$ . The velocities  $V_{air}$ ,  $V_{liq}$ , and  $V_{mix}$  are measured at the inlet and outlet of the foam generator. We also compute the average air and mixture velocity defined as,

$$V_{air,avg} = \frac{V_{air}^{in} + V_{air}^{out}}{2}, \quad V_{mix,avg} = \frac{V_{mix}^{in} + V_{mix}^{out}}{2}, \quad (4.4)$$

where  $V^{in}$  and  $V^{out}$  are the velocities at the inlet and outlet of the foam generator respectively.

In addition to the pressure and velocity in the foam generator, we also measured the pressure and velocity in the foam transport pipe carrying foam from the generator to the chamber. The foam transport pipe is connected directly to the outlet of the foam generator. Thus, the pressure at the outlet of the foam generator is taken to be the pressure at the inlet of the foam transport pipe.

We compute the superficial air and liquid velocities at the inlet and outlet of foam transport pipe using expressions analogous to those used for the generator.

$$V_{\text{air}}^{\text{pipe}} = \frac{\dot{m}_{\text{air}}}{\rho_{\text{air}} A_t}, \quad V_{\text{liq}}^{\text{pipe}} = \frac{\dot{m}_{\text{liq}}}{\rho_{\text{liq}} A_t}, \quad (4.5)$$

where  $A_t$  is the cross-sectional area of the foam transport pipe.

## 4.2 Influence of Flow Rate

To characterize the variations of pressure and velocity in the foam generator and foam transport pipe, we begin by performing a series of experiments where we fix the length of the foam generator ( $L_{\text{gen.}} = 110$  mm), diameter of the foam generator ( $D_{\text{gen.}} = 15.2$  mm), bead diameter ( $d = 1$  mm), and length of foam transport pipe ( $L_t = 1$  m). We vary the flow rates of air and liquid between the minimum and maximum values allowable by the system. The ratio of  $Q_{\text{air}}$  to  $Q_{\text{liq}}$  is controlled to maintain a constant foam expansion ratio,  $\text{FER} = 15$ , which is commonly used on tunneling sites. For the tests of varying bead diameter, the length of foam generator, and length of foam transport pipe, we replaced the pressure chamber with a bucket open to the atmosphere.

Figure 4.2(a) shows the variation of the inlet pressure (dotted line) and outlet pressure (solid line) with change in air flow rate ( $Q_{\text{air}}$ ). Note that we report the  $\dot{m}_{\text{air}}$  in terms of standard liters per minute at atmospheric conditions. As  $Q_{\text{air}}$  increases from 9.5 to 25.2 slpm, we observe that  $P_{\text{in}}$  and  $P_{\text{out}}$  both increase, and  $P_{\text{in}}$  is significantly larger than  $P_{\text{out}}$ . We also observe that the pressure drop ( $\Delta P = P_{\text{in}} - P_{\text{out}}$ ) increases with  $Q_{\text{air}}$ . For example, when  $Q_{\text{air}} = 9.5$  slpm,  $P_{\text{in}} = 560$  kPa,  $P_{\text{out}} = 220$  kPa, and  $\Delta P = 340$  kPa. At the maximum flow rate,  $Q_{\text{air}} = 25.2$ ,  $P_{\text{in}}$  increases to 885 kPa,  $P_{\text{out}}$  increases to 330 kPa, and  $\Delta P$  increases to 550 kPa. All pressures are reported as absolute pressures. Considering that the flow through the generator is driven by a pressure gradient, it makes sense that  $\Delta P$  should increase with  $Q_{\text{air}}$ .

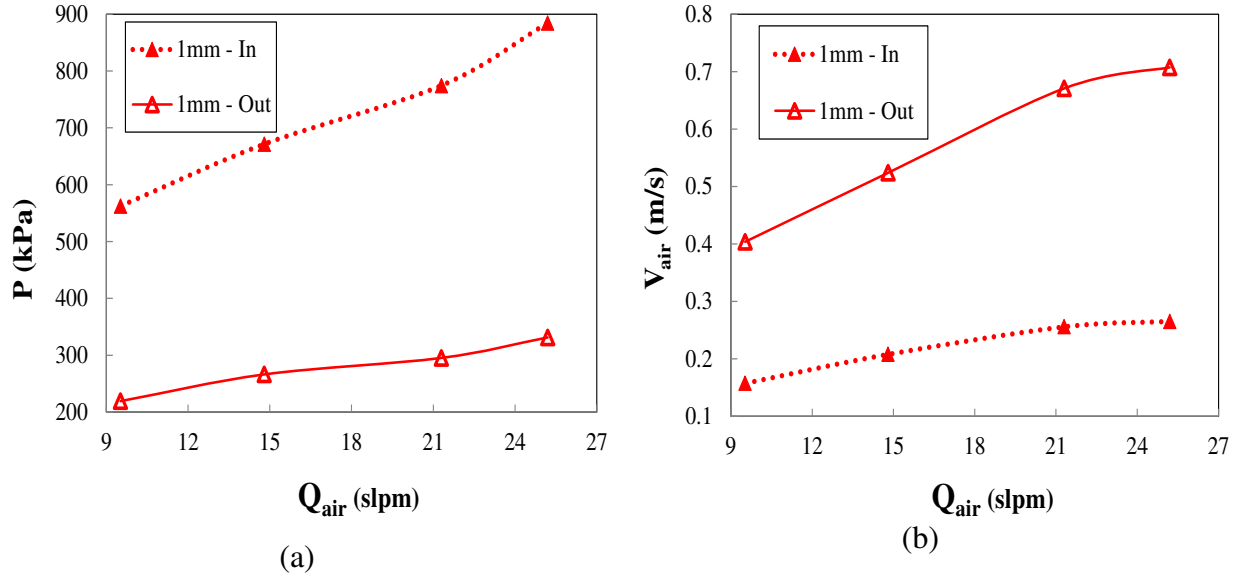


Figure 4.2 Variation of pressure and superficial air velocity across the foam generator: (a) Absolute pressure at the inlet and outlet of foam generator; (b) Superficial air velocity at the inlet and outlet of foam generator. The experiment is performed using 1 mm

We also note that foam flows lead to large pressure drops across the generator. We will demonstrate later that corresponding single-phase flows of just air or liquid produce much smaller pressure drops. In fact, a multiphase flow of air and water, i.e. no surfactant, also produces much smaller pressure drops than for foams. Consequently, foams likely flow in a unique manner compared to single phase flows and multiphase non-foam flows. The reason for a higher pressure drop for foam flows compared to multiphase flows is as follows. A multiphase flow (two immiscible fluids) in a porous medium is mainly driven by gravitational, pressure, viscous, and capillary forces (surface tension). Gravitational force leads to phase migration depending on the varying densities of the fluid. The capillary forces control the phase distribution, while the viscous forces influence the relative motion of the phases [65]. For a multiphase flow through porous media, the variation in the density and viscosity of the two immiscible fluids plays an important role. As the fluid with less viscosity and high density displaces a fluid with high viscosity and less density, instabilities arise in the process, leading to channeling of the phases through the pore

throats. This is called “viscous fingering” of phase interfaces [66]. Foam, on the other hand, is a matrix of tightly packed bubbles. As foam flows through porous media, these tightly packed groups of bubbles tend to flow through interconnected paths, without phase migration and fingering. This contributes to extra resistance to the foam flow compared to a multiphase flow. Also, note that the effective foam viscosity is much higher than its constituents. Hence, pressure drops for foam flows are significantly higher compared to multiphase flows.

Figure 4.2(b) shows  $V_{\text{air}}$  at the inlet (dotted line) and  $V_{\text{air}}$  at the outlet (solid line) of the foam generator. As expected,  $V_{\text{air}}$  increases with  $Q_{\text{air}}$ . Note, however that the outlet air velocities are consistently about 2.6 times greater than the inlet air velocities. The increase in  $V_{\text{air}}$  across the generator occurs due to the pressure drop  $\Delta P$ . As air flows across the generator, the air expands and causes an increase in  $V_{\text{air}}$  to conserve the mass flow  $Q_{\text{air}}$ . We also observe that the change in air velocity across the foam generator ( $\Delta V_{\text{air}} = V_{\text{out}} - V_{\text{in}}$ ) increases with  $\dot{m}_{\text{air}}$ . This is due to the simultaneous increase in pressure drop with air flow rate.

The plots in figure 4.2 show a linear trend for pressure and velocity with increasing  $\dot{m}_{\text{air}}$ . Figure 4.2(a) also indicates that the decrement in pressure from the inlet to outlet of the foam generator (pressure drop) is approximately 62% for all the cases. Consequently, the increment in superficial velocity is approximately 62%. This shows the coupled behavior of pressure and superficial air velocity and the influence of compressibility on the flow.

We also observe significant pressure drops through the foam transport pipe. As the outlet of the foam transport pipe is open to atmosphere, the pressure drop is simply the difference between the absolute pressure at the outlet of the foam generator and atmospheric pressure (101 kPa) at the outlet of the transport pipe. Figure 4.2(a) shows that there is a significant pressure drop per unit length across the transport pipe. For the range of mass flow rates  $Q_{\text{air}} = 9.5$  to 25 slpm, the

pressure drop through the foam transport pipe varies from 120 to 230 kPa. We will discuss the pressure drop through the transport pipe in detail in the later sections.

### 4.3 Influence of Bead Diameter

To investigate the influence of bead diameter, we repeated the experiments performed in section 4.2 for bead diameters of 2 and 3 mm. Figure 4.3(a) shows the variation of absolute pressure at the inlet and outlet of the foam generator with  $\dot{m}_{\text{air}}$  for bead diameter 1, 2, and 3 mm. We observe that the inlet and outlet pressures increase as the bead diameter decreases, and show a linear trend as well. For example, the inlet pressures for 1 mm bead are consistently ~140% higher than 3mm beads, while the outlet pressures for 1 mm beads are only 14% higher than 3mm beads respectively. We also observe that the pressure drop across the foam generator decreases

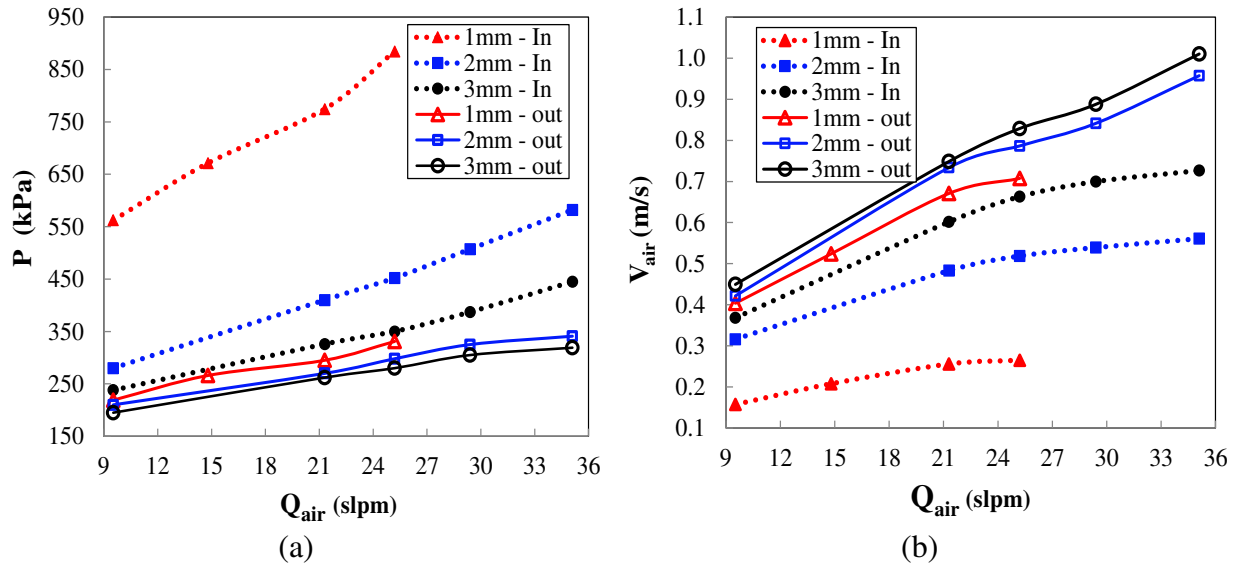


Figure 4.3 Variation of pressure and superficial air velocity across the foam generator for 1, 2, 3 mm bead diameter: (a) Pressure variation at the inlet and outlet of foam generator; (b) superficial air velocity at the inlet and outlet of foam generator

with increase in the bead diameter. The pressure drop at  $Q_{\text{air}} = 21.3$  slpm is approximately 450 kPa for 1 mm beads, 150 kPa for 2 mm beads, and 60 kPa for 3 mm beads. This is because, with an increase in the bead diameter, the pore size increases and reduces resistance to flow.

Figure 4.3(b) shows the variation of superficial air velocity across the foam generator with respect to the air mass flow rates. We see that  $V_{\text{in}}$  and  $V_{\text{out}}$  both increase with bead diameter. For example, the inlet superficial air velocity for 3 mm beads is approximately 30 % higher than the inlet velocity for 1 mm beads. And similarly, the outlet superficial air velocity for 3 mm beads is 12 % larger than 1 mm beads. This increase in velocity occurs due to a decrease in pressure with increasing bead diameter. Note that the outlet pressure at the foam generator is primarily determined by the flow downstream, i.e. in the foam transport pipe. Nevertheless, we observe a decrease in outlet pressure with increasing bead diameter. In chapter 5, we show that this is because the average bubble diameter increases with the bead diameter. Wenzel et al. have shown that pressure drops through a pipe increase with a decrease in the bubble diameter [21]. Hence, with smaller bubbles in the case of 1 mm beads, the outlet pressure at the generator (inlet pressure of the transport pipe) will be higher compared to 2 and 3 mm beads.

We observe considerable pressure drop through the transport pipe. Hence it is important to explore the pressure drop through the pipe. One can study the pressure drop by plotting it with the average foam velocity through the pipe, as described by the Hagen Poiseuille's law for pipe flows,

$$V_{\text{avg,foam}}^{\text{pipe}} = \frac{D^2}{32\mu} \frac{\Delta P}{L}. \quad (4.6)$$

Figure 4.4(a) shows the pressure drop ( $\Delta P$ ) through the transport pipe versus average foam velocity across the pipe ( $V_{\text{avg,foam}}^{\text{pipe}}$ ). The  $\Delta P_{\text{Transport pipe}}$  decreases with increase in bead diameter. For example, the pressure drop through the pipe for 1 mm beads foam generator is approximately

25 % higher than the pressure drop through 3 mm beads. This likely occurs due to increase in the bubble diameter, as mentioned earlier. It is observed in literature that as the average bubble diameter becomes smaller, the foam viscosity tends to increase, and result into higher pressure drop through the pipe. Note that for same  $V_{avg,foam}^{pipe}$ , the pressure drop across the transport pipe is always higher for 1 mm beads followed by 2 mm and 3 mm beads.

Figure 4.4(b) shows the pressure drop through the foam generator. As expected, with decrease in the bead size pressure drop through the generator increases, because the resistance to the flow increases due to decrease in the permeability. For example, at  $V_{avg,foam}^{gen.} = 0.42$  m/s, the pressure drop per unit length for 3 mm is approximately eight times smaller than the  $\Delta P_{Foam\ gen.}$  through the 1 mm beads generator. While the pressure drop through the 2 mm beads generator is twice than 3 mm beads.

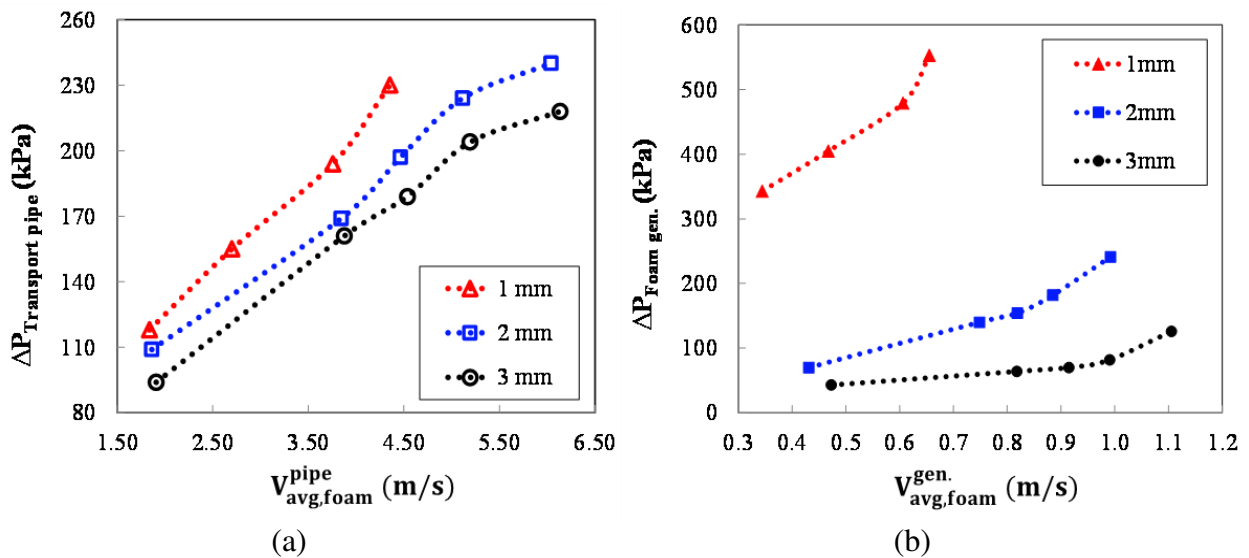


Figure 4.4 Pressure drop ( $\Delta P$ ) for 1, 2, 3 mm bead foam generator: (a) Pressure drop through the 1m foam transport pipe; (b) Pressure drop across the foam generator.  $\Delta P_{Foam\ generator}$  is higher than  $\Delta P_{Transport\ pipe}$  for 1mm bead foam generator.

Figure 4.5 shows the log-log plot for the pressure drop through the pipe and average foam velocity. We observe that  $\log(\Delta P_{\text{Transport pipe}})$  obeys a linear behavior with  $\log(V)$  where  $n$  is 1.01, 0.96 and 0.98 for 1, 2 and 3 mm. It obeys the relationship suggested by Wenzel et al. [21] with  $n \approx 1$ ,

$$\Delta P = AV^n, \quad (4.7)$$

where  $\Delta P$  is the pressure drop,  $V$  is the average velocity,  $n$  is the slope of the line and  $A$  is a constant.

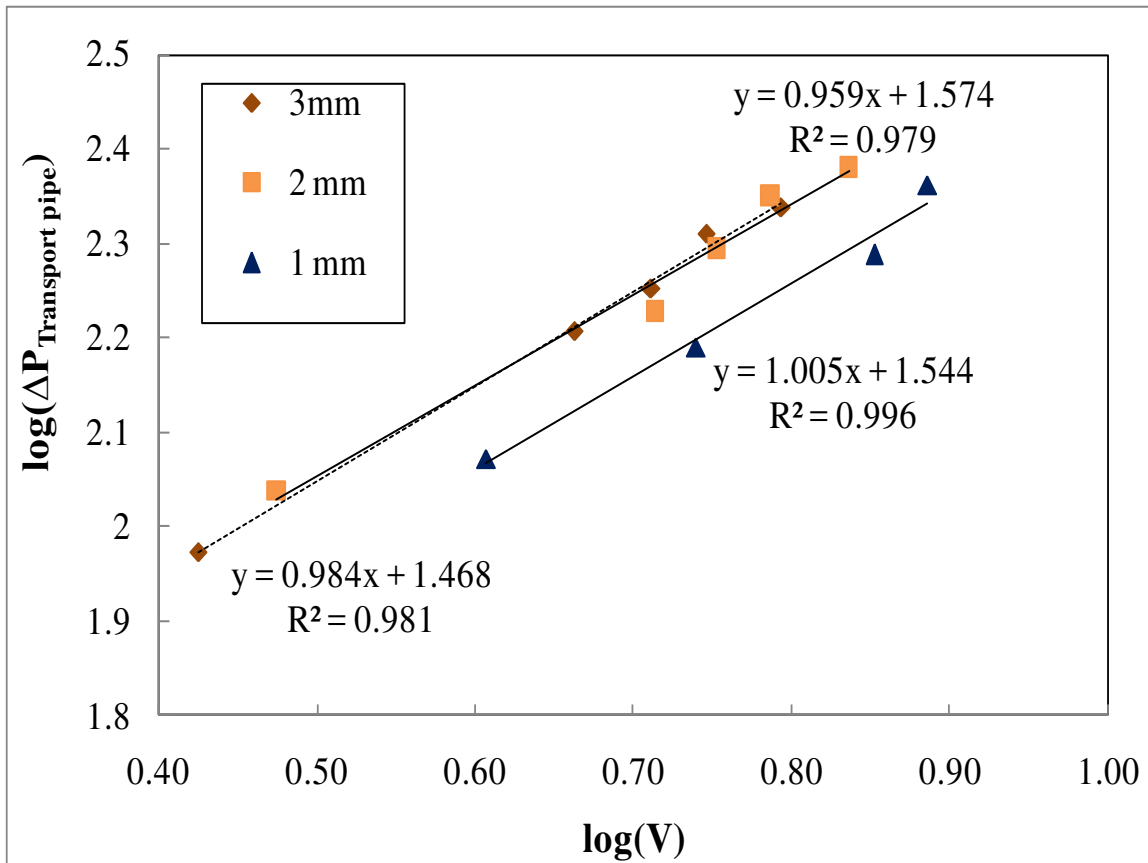


Figure 4.5 Pressure drop across transport pipe as a function of average foam velocity on a log plot

We observe from figure 4.6 that  $\log(\Delta P_{\text{Foam gen.}})$  follows a linear regime for 1, 2, 3 mm bead diameter with a slope of 0.7, 1.4, and 1.07 respectively. This behavior indicates a transition of flow regime for the two-phase flow through porous media. These results also indicate that for 1 mm beads  $\Delta P$  varies as  $V^{0.7}$  and  $A = 2.103$ , while for 2 mm beads,  $\Delta P$  varies as  $V^{1.4}$  and  $A = 1.164$ .

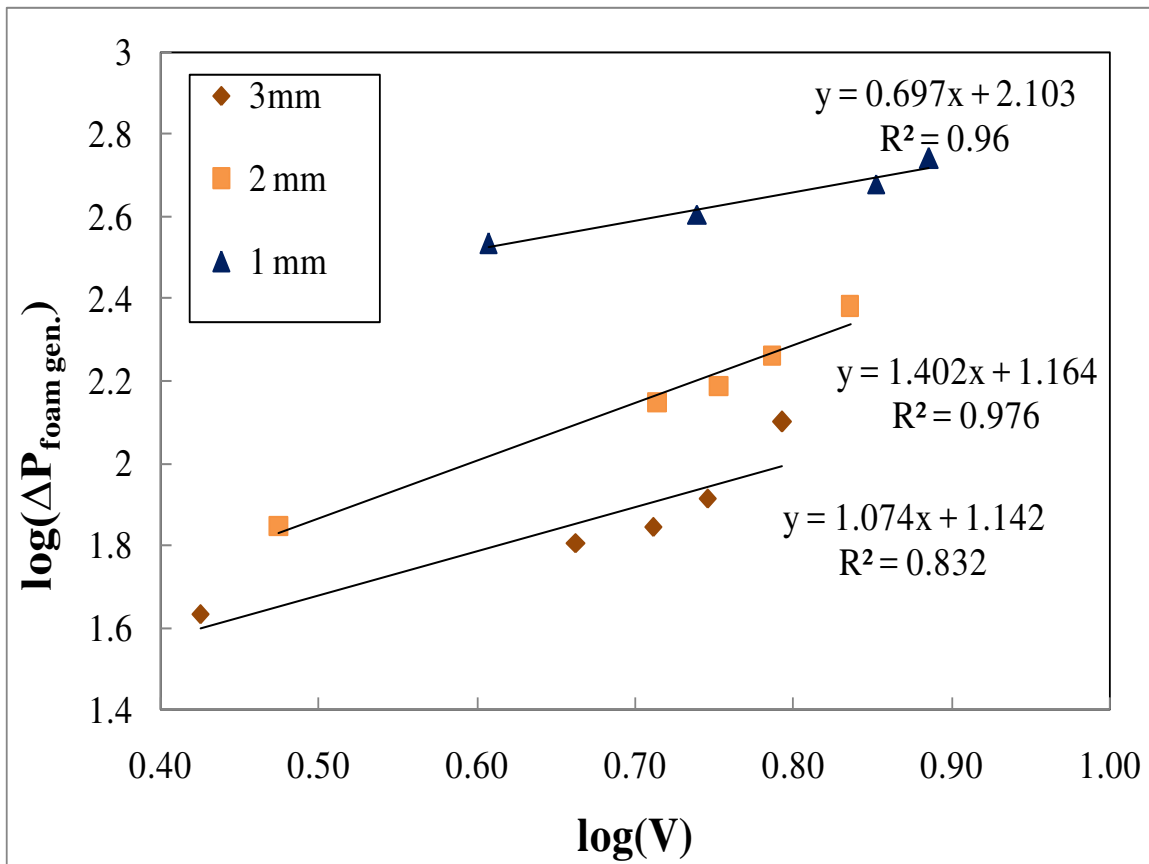


Figure 4.6 Pressure drop across foam generator as a function of average foam velocity on a log-log plot

#### 4.4 Influence of Length of Foam Generator

To investigate the influence of the length of the foam generator, we repeated the experiments in section 4.3 for the generator lengths 200 and 400 mm. We fix the bead size to 3 mm, and length of foam transport pipe to 1 m. Figure 4.7(a) shows the absolute pressure at the inlet and outlet of the generator for the three lengths considered.

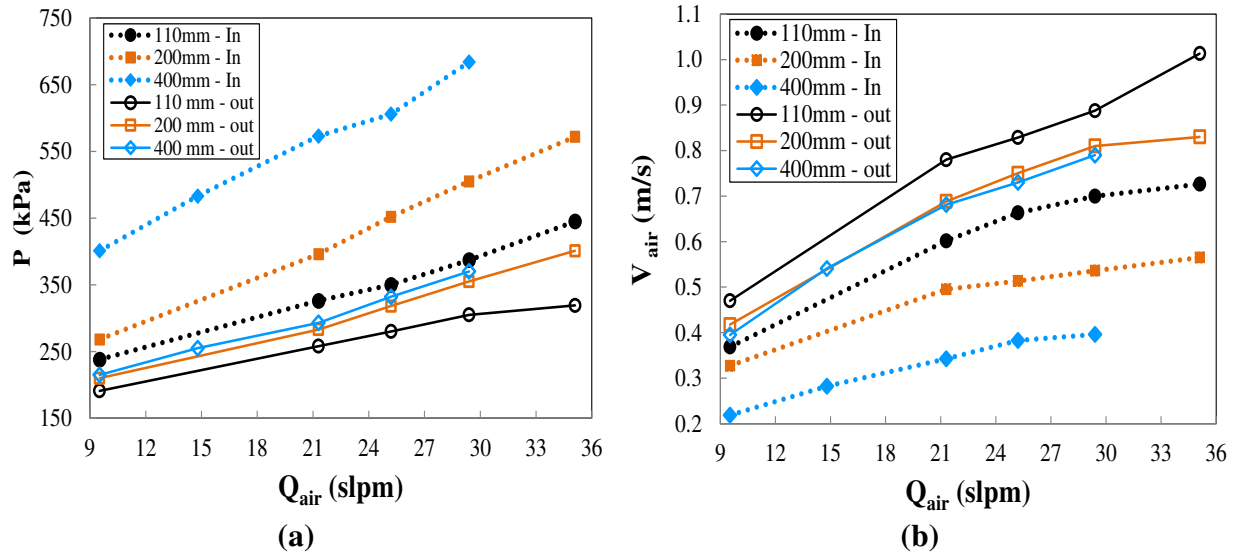


Figure 4.7 Absolute pressure and superficial air velocity for different lengths of foam generator: (a) absolute pressure at the inlet and outlet of foam generator; (b) superficial air velocity at the inlet and outlet of foam generator.

The inlet and outlet pressures increase with the length of the foam generator. The length of foam generator significantly influences the inlet pressure of the foam generator because the flow has to expend more energy to overcome the resistance to the flow that increases with the length of the generator. However, it has a considerably smaller influence on the outlet pressure of the foam generator, which is primarily determined by the downstream conditions of the transport pipe.

For example, the inlet pressure for 400 mm length of foam generator is consistently 70 % higher than 110 mm for the same mass flow rates. While the increment in the outlet pressure of the foam generator is around 10 %. The small increment in outlet pressure is due to the smaller bubbles created by a longer generator.

Figure 4.7(b) shows the corresponding result for the superficial air velocity across the generator for varying  $Q_{\text{air}}$ . We observe that, by increasing the length of foam generator from 110 mm to 200 and 400 mm, the inlet and outlet superficial air velocities consistently decrease. For example, by increasing the length of the generator from 110 to 400 mm, the inlet and outlet velocities decrease by 45 % and 12 % respectively. This is due to the higher pressures at the inlet of the foam generator resulting from the resistance offered by the porous medium.

Figure 4.8 shows the plot for pressure drop ( $\Delta P_{\text{Transport pipe}}$ ) across the foam transport pipe as a function of the average foam velocity. We observe from the plot in figure 4.8 that the  $\Delta P_{\text{Transport pipe}}$  for 200 and 400 mm is higher than 110 mm. For example, at  $V_{\text{avg,foam}}^{\text{pipe}} = \sim 8$  m/s the pressure drop for 110, 200, and 400 is 155, 180, and 190 kPa respectively. This is because by increasing the length of the foam generator, we increase the residence time that the fluid spends as it flows from the inlet to the outlet of the foam generator. We predict that the change in the pressure drop is due to decrease in the average bubble diameter, and we will confirm this in chapter 5. Wenzel et al. [21] also observed that as the bubbles get smaller the pressure drop across the transport pipe increases. However, we see a small difference of 2 % in  $(\Delta P/L)_{\text{Transport pipe}}$  for 200 and 400 mm foam generators. This is because the pressures at the inlet of the transport (outlet of the foam generator) are mainly governed by the downstream conditions, as shown in figure 4.7(a)

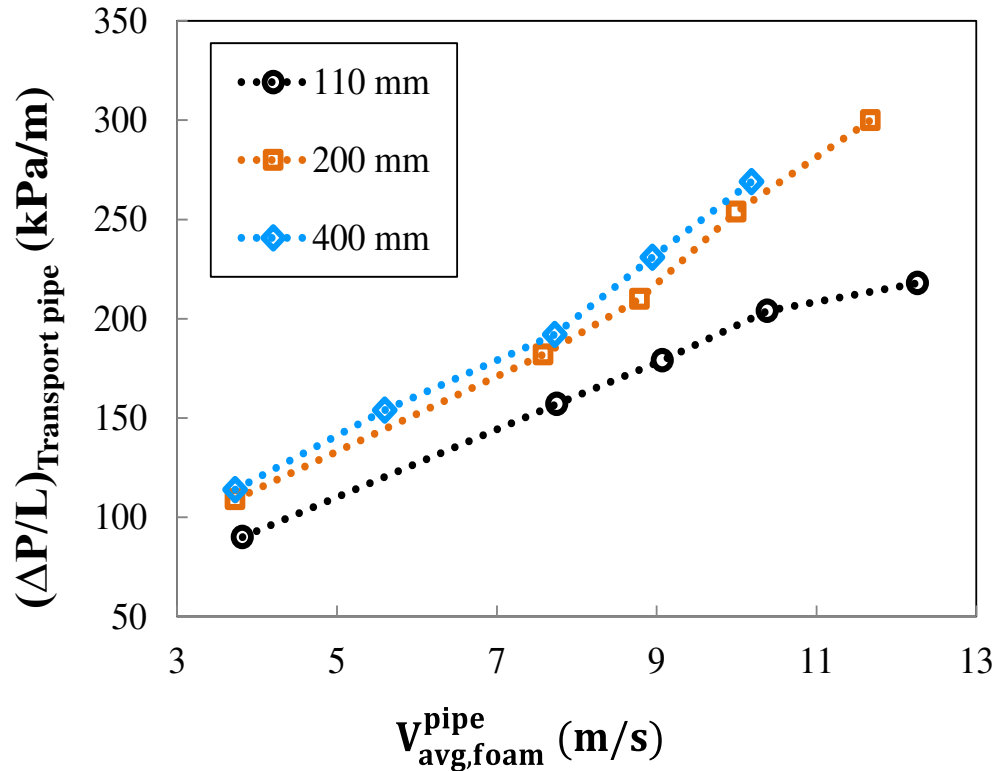


Figure 4.8 Pressure drop per unit length across the transport pipe as a function of average superficial air velocity.

Figure 4.9(a) and (b) show the pressure drop ( $\Delta P_{Foam\ gen.}$ ) and pressure drop per unit length ( $\Delta P/L$ ) across the foam generator, respectively, as a function of the average foam velocity. In figure 4.9 we observe that  $\Delta P$  and  $\Delta P/L$  across the foam generator increase with the length of the generator. We also notice that initially, the pressure drop behaves in a linear regime and then the trend shifts towards a non-linear regime at  $V_{avg,foam}^{gen.} > 1$  m/s. This is evident from the best fit shown in figure 4.9. In the linear regime, the slopes for the pressure drop increase with the length of foam generator. We also observe a similar trend in the slopes for the plot of pressure drop per unit length as a function of average foam velocity, shown in figure 4.9(b).

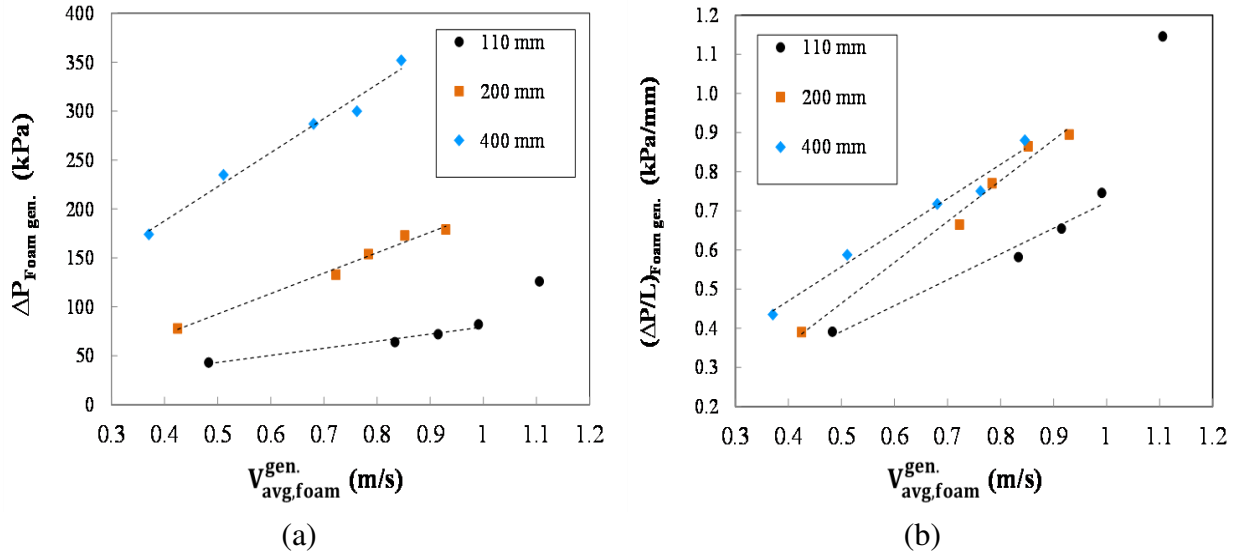


Figure 4.9 Pressure drop as a function of average foam velocity: (a) pressure drop through foam generator (b) Pressure drop per unit length through the foam generator. The dashed line is the best fit for the data points that indicate a linear regime.

If we interpret these results using the Darcy's law,

$$V_{\text{avg,foam}}^{\text{gen.}} = -\frac{k \Delta P}{\mu L}, \quad (4.8)$$

We find that the ratio of permeability to the viscosity (slope) is 1.1 for 400 mm, while it is 1.7 for 110 mm, as in figure 4.9(b). If we assume the effective foam viscosity remains constant for the three lengths of foam generator, the permeability would decrease as the length of generator increases. However, this is not likely because we fix the bead size of the porous medium for the three lengths. The more likely explanation is that the permeability is constant and the effective viscosity increases as the length of the generator increases. We can explain this physically because we observe that the average bubble diameter decreases with increase in the length of foam generator.

#### 4.5 Influence of Length of Foam Transport Pipe

We investigated the influence of the length of the foam transport pipe by varying the length of the foam transport pipe as 1, 3 and 5 m. Figure 4.10(a) shows a plot of pressure at the inlet and outlet of foam generator for 1, 3 and 5 m length of foam generator. As expected, the pressures at the inlet and outlet increase with the length of the foam transport pipe. This is due to the increase in  $\Delta P$  in the transport pipe. For example, when the length of transport pipe increases from 1 to 3 m, at  $Q_{\text{air}} = 21.2$  slpm, the pressure at the inlet of the transport pipe (outlet of foam generator) increases by 60 %, and consequently, the inlet pressure of the generator increases by 45 %. It is also evident from figure 4.10(a) that with increase in the length of the foam transport pipe, the pressure drop across the foam generator becomes smaller compared to the pressure drop across the foam transport for different  $Q_{\text{air}}$ .

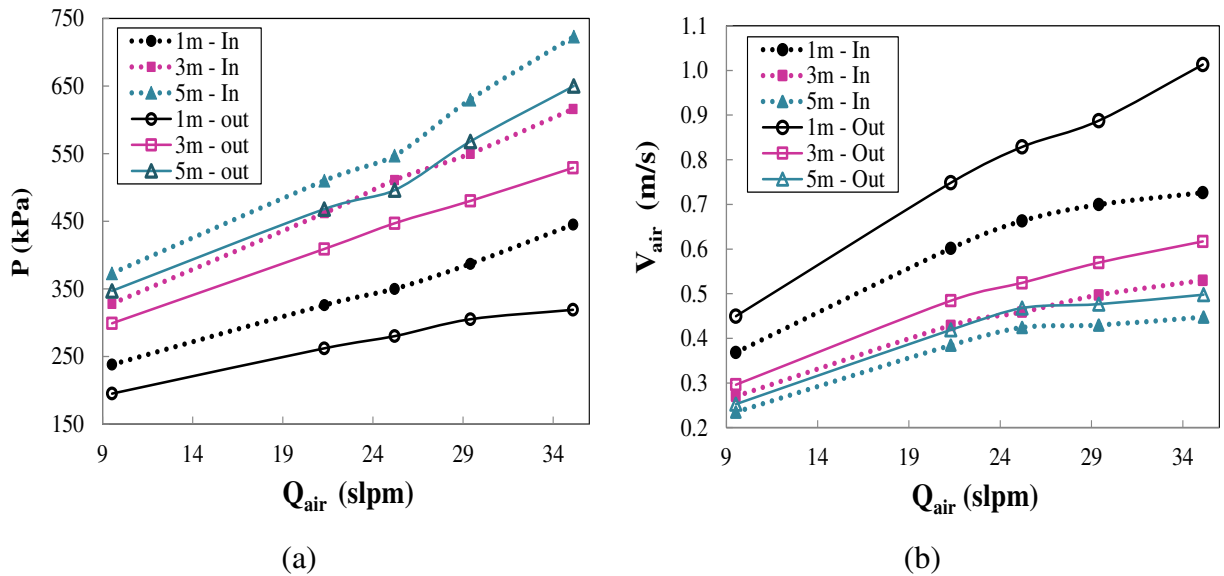


Figure 4.10 Absolute pressure and superficial air velocity for three different lengths of foam transport pipe: (a) Absolute pressure at the inlet and outlet of foam generator; (b) Superficial air velocity at the inlet and outlet of foam generator. The pressure at the inlet of 3m tube and outlet of 5 m tube are similar, hence their superficial velocities are overlapping.

Figure 4.10(b) shows the plot of superficial air velocity at inlet and outlet of the generator for different lengths of transport pipe. It is observed that with increase in the length of the transport pipe, the outlet and inlet velocities tend to decrease because the absolute pressures across the generator increase. Varying the length of pipe from 1 m to 3 m the inlet velocities decrease by 27 % and the outlet velocities decrease by 34 %.

Plots of pressure drop ( $\Delta P$ ) and pressure drop per unit length ( $\Delta P/L$ ) through the foam transport pipe are shown in figure 4.11(a) and (b) respectively. Figure 4.11(a) shows the pressure drop as a function of the average foam velocity ( $V_{avg,foam}^{pipe}$ ) through the foam transport pipe. As expected, the pressure drop through the pipe increases with the length of pipe and the average foam velocity. The pressure drop for foam flow in pipes is not only due to the wall friction. The effective foam viscosity, and average bubble diameter [21]–[23], [53] also influence  $\Delta P$ .

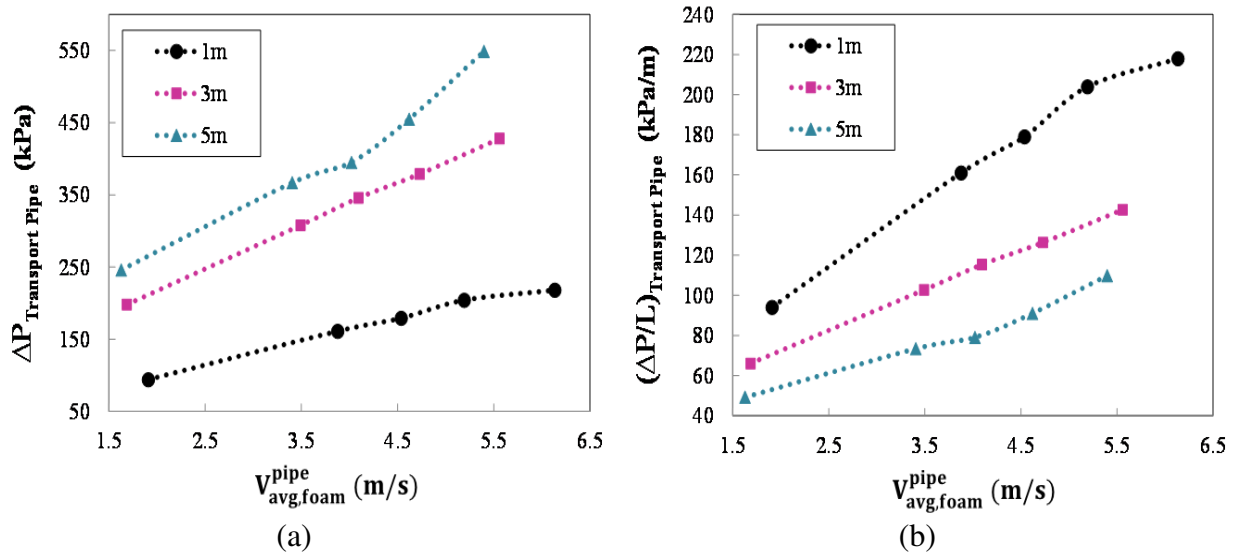


Figure 4.11 Pressure drop for 1, 3 and 5 m foam transport pipe lengths: (a) Pressure drop through the foam transport pipe; (b) Pressure drop per unit length through the transport pipe.

However, it is interesting to note that pressure gradient decreases with increase in pipe length. One possible explanation is that as foam flows through pipes, it flows on a thin liquid layer. As the foam undergoes shear at the walls of the pipes, the bubbles near the walls rupture leading to an increase in the thickness of the liquid layer. This would eventually decrease the effective foam viscosity, resulting in a smaller net pressure gradient.

Figure 4.12 shows the pressure drop across the foam generator for the three lengths of transport pipe. We initially observe a linear behavior of  $\Delta P_{\text{Foam gen.}}$  as a function of average foam velocity, and then it transitions to a non-linear behavior. A similar transition from linear to the non-linear regime is seen for single phase flows through porous media. We observe a linear behavior of pressure drop with respect to the fluid velocity at low flow rates that satisfies Darcy's law. This is because at low flow rates only viscous effects contribute to the energy dissipation in terms of pressure drop. However, at higher velocities, the inertial forces also come into play and the Darcy regime transitions to a non-linear Forchheimer regime.

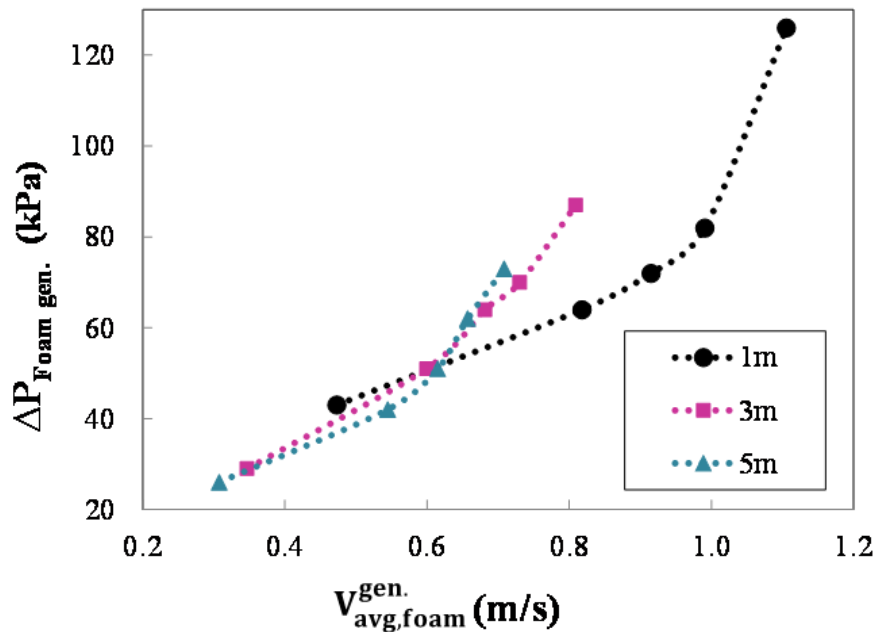


Figure 4.12 Pressure drop across the foam generator for 1, 3, 5 m lengths of foam transport pipe

#### 4.6 Influence of Pressure Chamber

In the second set of experiments, we conducted the pressure chamber tests to replicate the foam injection into the underground soil from the cutter head of a tunnel boring machine. We used three different chamber pressures - 1, 3, and 5 bar. Note that in the first set of experiments we fixed the foam expansion ratio to 15 and we measured it at atmospheric conditions ( $FER_0 = 15$ ). For the pressure chamber tests, we fixed the foam expansion ratio ( $FER_p$ ) to 15 for three chamber pressures ( $P = 1, 3, \text{ and } 5 \text{ bar}$ ) and varied the  $FER_0$ . The  $FER_p$  was calculated using equation 4.7,

$$FER_p = 1 + (FER_0 - 1) \frac{P_{atm}}{P + P_{atm}}, \quad (4.9)$$

where  $P$  is the chamber pressure and  $P_{atm}$  is the atmospheric pressure in the laboratory. For all pressure chamber tests, we used 3 mm beads, 200 mm long foam generator and 1m length of foam transport pipe. The surfactant concentration used for these tests is 5% SLF50.

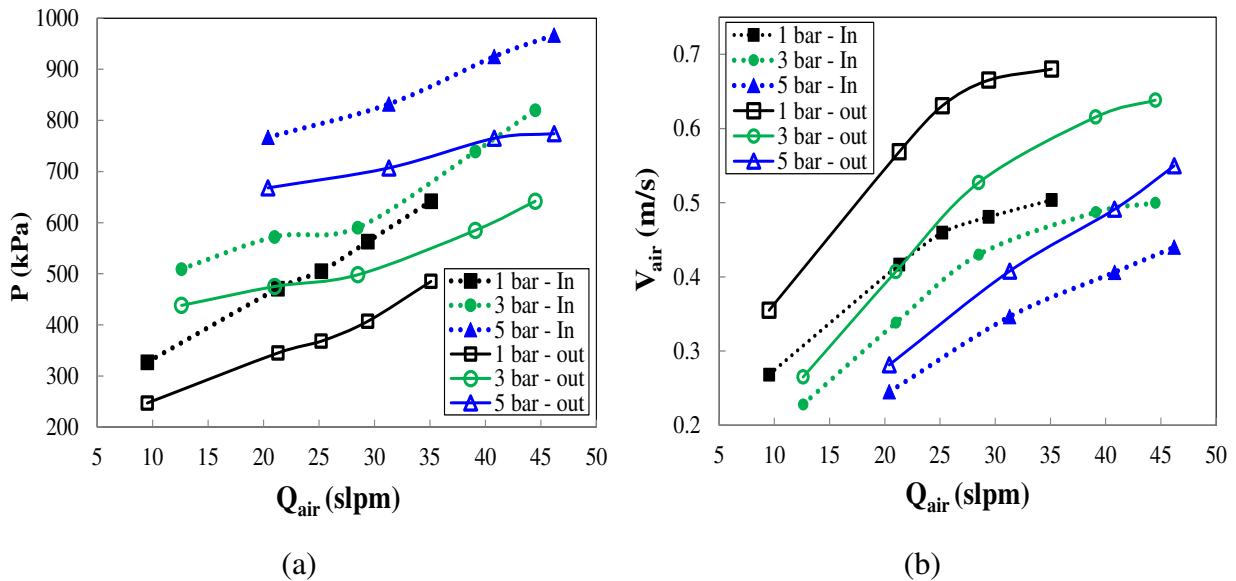


Figure 4.13 Variation of flow parameters in pressure chamber tests: (a) Absolute pressure at the inlet and outlet of foam generator. Dotted lines indicate inlet and solid lines outlet conditions across the foam generator; (b) Variation of superficial air velocity at the inlet and outlet of the generator.

Figure 4.13(a) shows the variation of pressure at the inlet and the outlet of the foam generator for varying air mass flow rates and different chamber pressures. As expected, the pressure throughout the system increases with chamber pressure. Figure 4.13(b) shows the variation of superficial air velocity across the foam generator. In the case of 1 bar and 3 bar chamber pressure, we observe a linear trend up to a certain flow rate, and then it tends to plateau. However, this behavior is not observed for 5 bar chamber pressure.

This is because with increase in  $Q_{\text{air}}$  we see a significant rise in the absolute pressures for 1 and 3 bar chamber pressure. For example, in the case of 1 and 3 bar chamber pressure, as  $Q_{\text{air}}$  increases, the absolute pressures at the outlet of foam generator rise from 230 to 470 kPa, and 420 to 620 kPa respectively. While in the case of 5 bar chamber pressure, the absolute pressures at the outlet of the generator rise from 680 to 770 kPa. Hence, due to the coupled nature of velocity and pressure, we see that the velocity tends to plateau at higher flow rates.

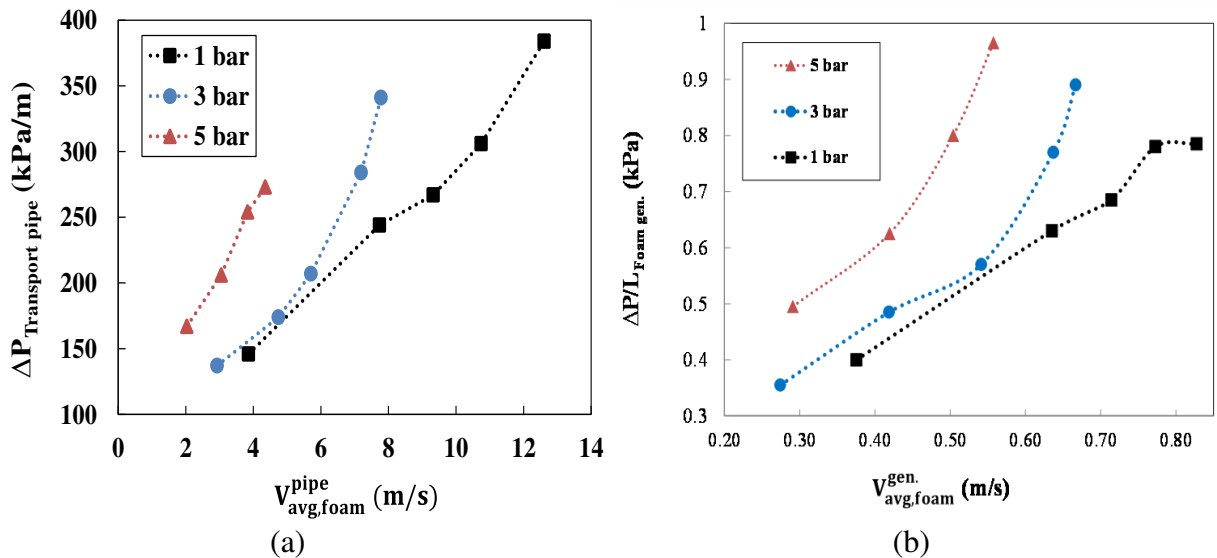


Figure 4.14 Pressure drop for the foam flow across the foam generator and transport pipe for different chamber pressures: (a) Pressure drop through the transport tube for different average foam velocity across the pipe; (b) Pressure drop through the foam generator

Figure 4.14(a) shows the variation of pressure drop across the foam transport pipe as a function of the average foam velocity in the pipe. As the chamber pressure increases, the pressure drop through the foam transport pipe also increases. For example, at  $V_{\text{avg,foam}}^{\text{pipe}} = 4$  m/s,  $\Delta P_{\text{Transport pipe}}$  is approximately 150 and 270 kPa for 1 and 5 bar chamber pressure respectively. We predict that with increase in chamber pressure, the average foam bubble diameter decrease, which leads to higher pressure drop through the transport pipe. We will show this in the bubble size analysis discussion in chapter 5.

The plot in figure 4.12(b) shows the pressure drop across the foam generator for different chamber pressures. The pressure drop increases with chamber pressure. We observe that  $\Delta P_{\text{Foam gen.}}$  follows a linear regime for 1 bar chamber pressure, and it transitions to a non-linear regime for 3 and 5 bar chamber pressure.

#### **4.7 Influence of Transport Pipe Diameter s**

We also performed a study to investigate the influence of the pipe diameter on the pressure and superficial velocity of the foam flow under 1 bar and 3 bar chamber pressure. The flow parameters for this test are the same as ones used in section 4.6; while the surfactant used for the test is 5% SLF47. We consider the following pipe diameter for this test - 6.3, 9.5 and 12.7 mm.

The plot in figure 4.13 shows the pressure drop through varying diameter of the foam transport pipe. It shows that the pressure drop is highest for 6.3mm pipe and it decreases with the increase in the pipe diameter. The pressure drop through the transport pipe is due to foam viscosity, average bubble diameter, the friction factor and the Reynolds number of the flow.

Correlations in the literature show that for foam flow, friction factor is inversely related to the Reynolds number [22], [51]. With the increase in the pipe diameter the Reynolds number of the

flow increases, this in turn decreases the friction factor for foam flow. Hence the pressure drop decreases with increase in pipe diameter.

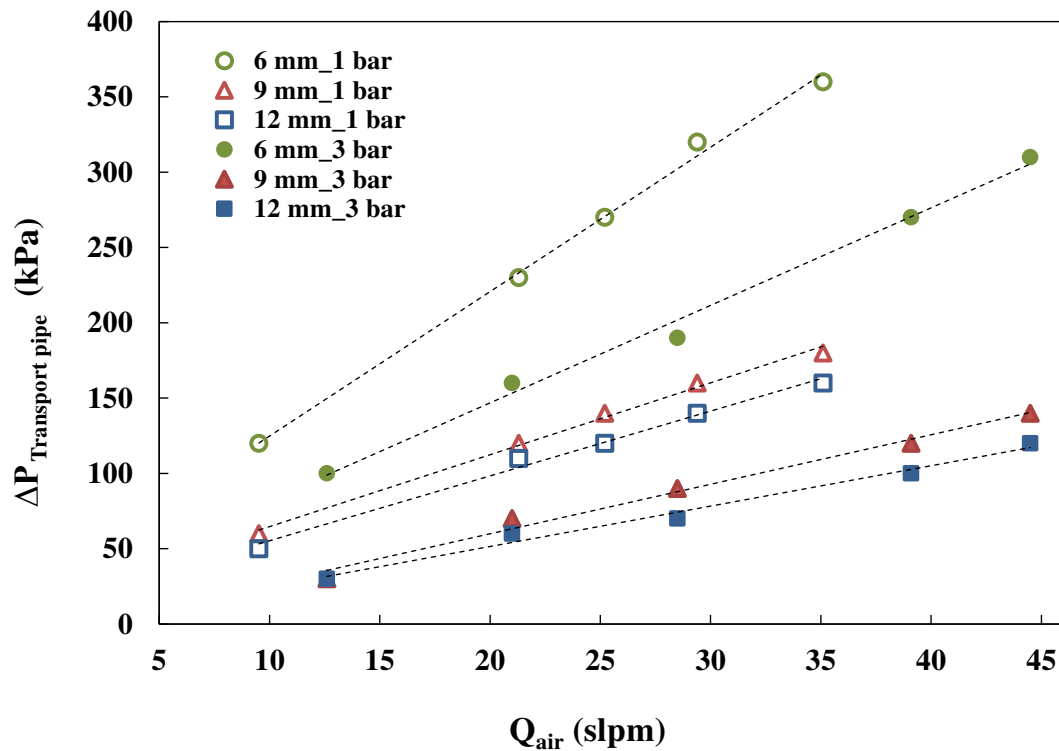


Figure 4.15 Pressure drop across the foam transport pipe for diameters 6.3, 9.5 and 12.7 mm. The length of the transport pipe is fixed at 1m, the FER is 15, and the length of foam generator is 200 mm.

Figure 4.13 show the comparison pressure drop per unit length using different pipe diameter for chamber pressures, 1 bar and 3 bar. The plots show that the diameter of the transport pipe significantly influences the  $\Delta P/L$  through the pipe as mass flow rate increases. This is because increasing the pipe diameter changes the upstream pressures in the system. In the case of 1 bar chamber pressure, we observe that the  $\Delta P/L$  through the pipe decreases with increase in the pipe diameter. This is because with increase in pipe diameter, the surface roughness decreases, and the Reynolds number increases. If we consider the Moody diagram reported by Blauer et al. [22] for foams, then we can suggest that the friction factor decreases with increase in Reynolds number.

As a result, this reduces the pressure drop per unit length through the pipe. Also, Raza et al. and David et al. have reported that the effective foam viscosity decreases with increase in the pipe diameter, hence the change in effective foam viscosity could be another factor influencing  $\Delta P/L$  through the pipe. We observe a similar trend as we increase the chamber pressure increases to 3 bar.

#### 4.8 Pressure drop for single phase and multiphase flow using pressure chamber

We perform some additional tests to measure the pressure drops across the foam generator for single phase flows, and multiphase non-foam flows (air plus water). For this test, we fix the length of foam generator to 200 mm, bead size to 3 mm, the length of transport pipe to 1 m, FERp to 15, and chamber pressure to 1 bar.

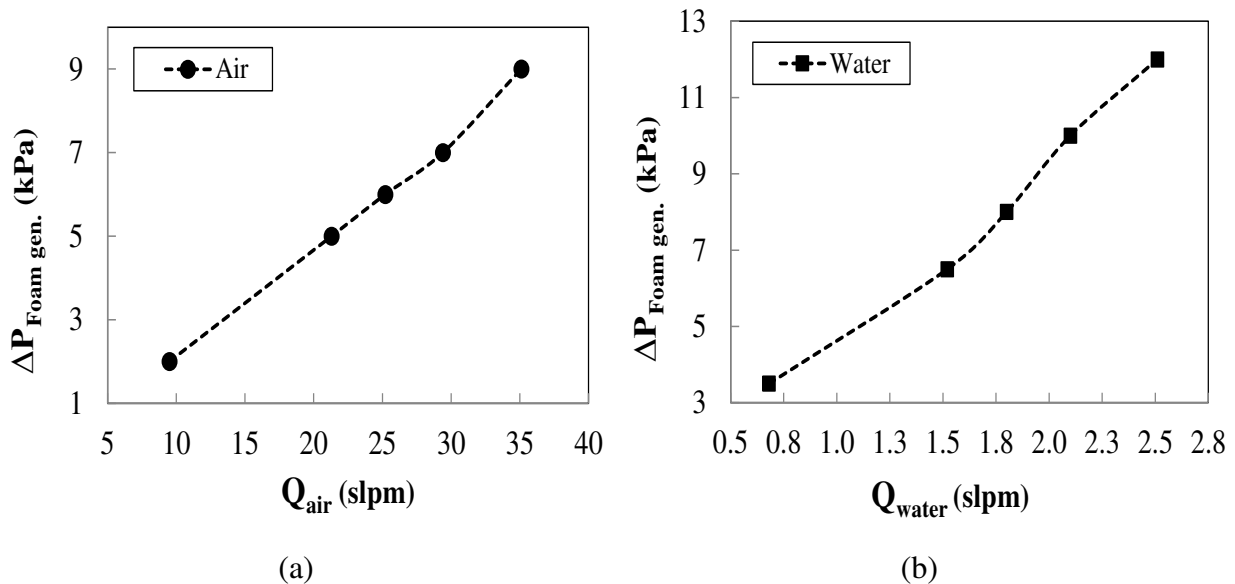


Figure 4.16 Pressure drop for single phase flow across the foam generator under 1 bar chamber pressure with varying mass flow rates: (a) Pressure drop for air flow; (b) Pressure drop for water flow. Length of foam generator is 200 mm, bead size is 3 mm and FERp is

Figure 4.14 (a) and (b) show the pressure drop across the foam generator for only air and water flow respectively. We observe from figure 4.14 that the pressure drop for only air, and liquid flow varies from 1 to 13 kPa.

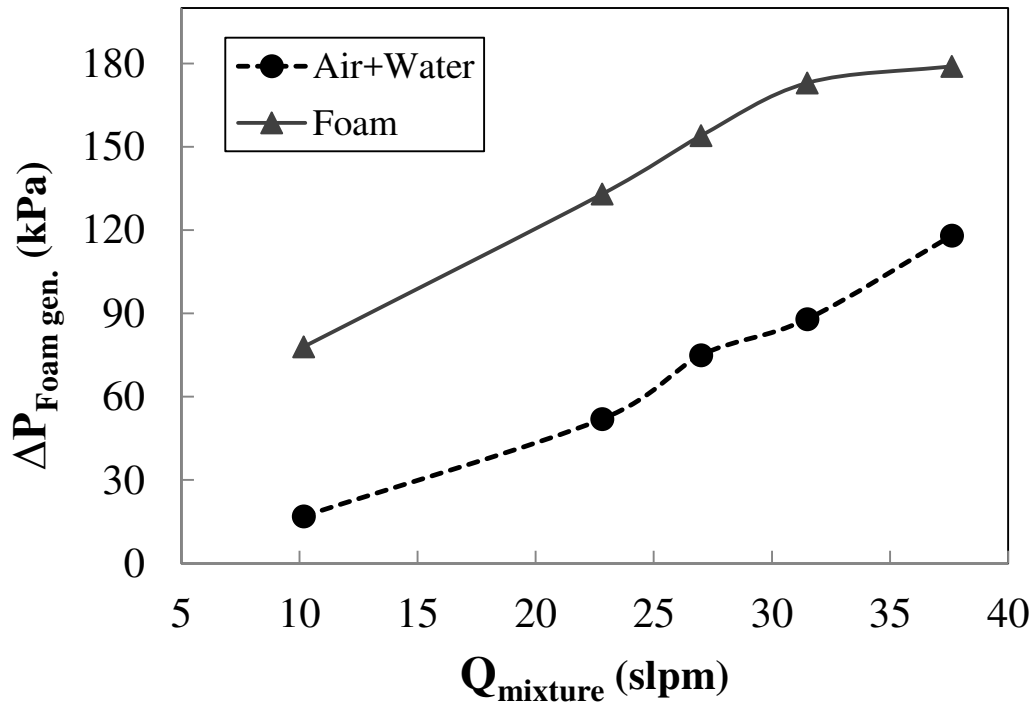


Figure 4.17 Pressure drop across the foam generator for multiphase (air and water) flow - dashed line, and foam flow - solid line. For both the tests the length of the foam generator is 200 mm, the length of transport pipe is 1 m, and bead size is 3 mm.

Figure 4.15 shows the pressure drop across the foam generator for multiphase non-foam flow (air and water) (dashed line), and foam flow (solid line). We see that the pressure drop for foam flow is approximately three times higher than the air-water mixture flow through the porous medium.

This chapter investigates the influence of operating parameters and flow conditions on foam properties for different foam generation conditions discussed in chapter 4. We will discuss the variation of the bubble size distribution, foam compressibility, and foam drainage time. We will also discuss some preliminary tests results on foam generation without a foam generator, and variation of bubble size through the transport pipe.

### **5.1 Foam Capture and Image Analysis**

In our study, we capture the foam bubbles using a foam capture device and photograph it using a microscope. The foam bubble capture procedure is discussed in the appendix A. We analyze the bubble images using software called AmScope that comes along with the microscope. Figure 5.1 shows an example of the image analysis. We carry out the image analysis as follows,

1. Calibrate the microscope using a scale and determine the resolution of the image.
2. Import the foam bubble photograph in AmScope (image analysis software) and set the resolution based on the calibration of the microscope.
3. Select an area in the photograph where all the bubbles are clearly visible. Count a minimum of 700 bubbles manually in this area. This number is based on the convergence study, which indicates that the average bubble diameter becomes constant after 700 bubbles.
4. Export the measurement sheet to excel and carry out the analysis by computing the minimum, maximum and average bubble diameter.

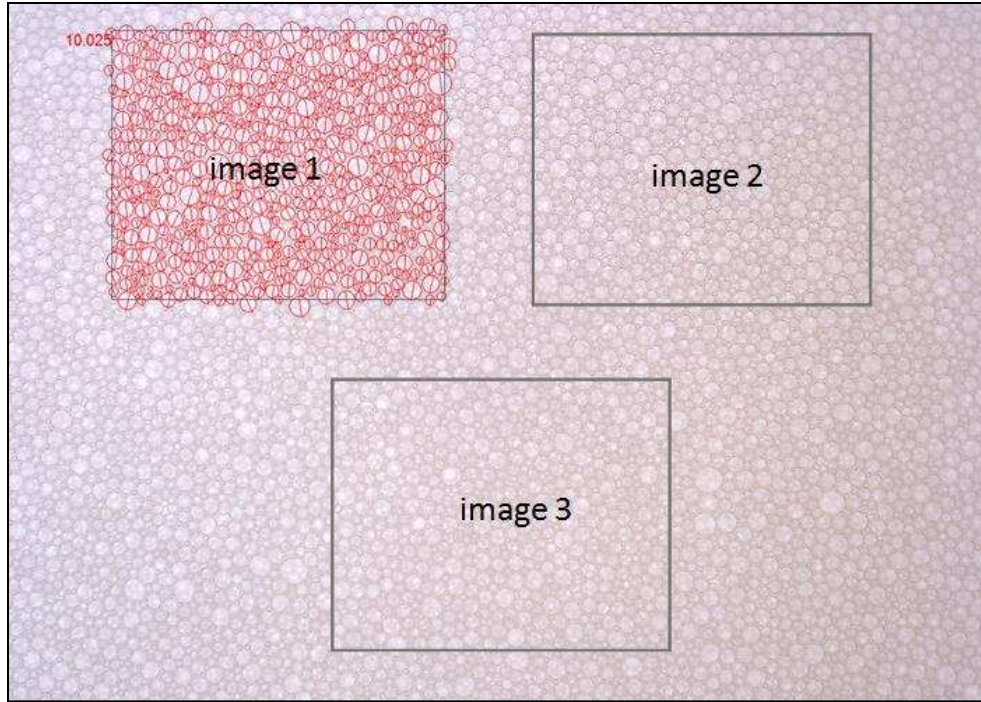


Figure 5.1 Sample photograph of foam bubbles during analysis using Amscope software

## 5.2 Influence of operating parameters on bubble distribution

Foam bubble diameter is important foam characteristic that influences the foam stability, soil foam mixture, and foam compressibility. Small bubble diameter enhances the foam stability by reducing the rate of inter-bubble diffusion. However, for a foam-soil mixture, small bubbles tend to migrate through the soil, as a result, an optimum bubble size is required for the foam soil mixture. Likewise, the bubble size also affects the foam compressibility, as in smaller bubbles are less compressible because they tend to behave as rigid spheres due to high internal pressure.

Previous studies in the literature show that foam bubble diameter has a significant influence on the foam viscosity and pressure drop through the foam transport pipe [7], [21], [35], [67]. Wenzel et al. have shown that as foam flows through a pipe the foam bubble diameter decreases due to shear rate. While some studies have modeled foam flow by assuming that the foam bubbles

expands as they flow in a pipe from a high pressure to lower pressure region [22]–[24], [51], [68]–[71]. All these studies focus on the variation of the foam bubbles as they flow through the pipe. There are few published studies in the tunneling community that discuss the influence of system design (geometry foam generator and transport pipe, porous media, chamber pressure) and operating conditions (pressure and velocity) across the porous media on the foam bubble size [8], [19].

In this study, we investigate the influence of flow parameters on the bubble size distribution for the same experiments discussed in chapter 4 for varying bead diameter, the length of foam generator, the length of foam transport pipe, and pressure chamber experiments (section 4.3 to 4.6).

### **5.2.1 Variation of bubble size with bead diameter**

We will discuss the bubble distribution for foam generation using different bead diameters. This is the same test as the one performed in section 4.3 where the length of foam generator is 110 mm, and length of transport pipe is 1 m. We also control the air and liquid mass flow rates. Note that all the plots in this chapter have 5 % error bars for the bubble diameter measurements.

Figure 5.2 shows the variation of average bubble diameter with average superficial velocity ( $V_{\text{avg,air}}$ ) across the foam generator for 1 mm, 2 mm and 3 mm bead diameter. The average bubble diameter for 1, 2 and 3 mm beads at  $V_{\text{avg,air}} = \sim 0.4$  m/s is approximately 0.045, 0.07, and 0.11 mm respectively. As expected the average foam bubble diameter decreases with a decrease in the bead diameter. This reduction is likely due to the decrease in pore size. Figure 5.3 shows the bubble images for the three bead diameters at  $V_{\text{avg,air}} = \sim 0.4$  m/s.

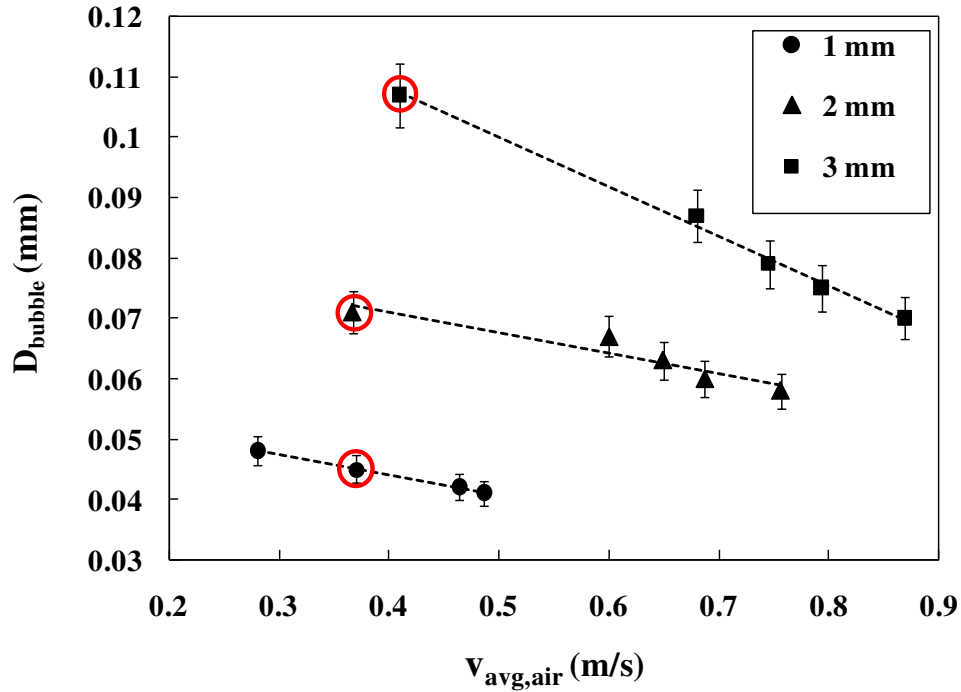


Figure 5.2 Average bubble diameter as a function of average superficial air velocity ( $V_{avg,air}$ ) across the foam generator for three different bead diameters 1 mm, 2 mm and 3 mm. The dashed lines indicate linear fit for the data points. For this experiment the length of foam gun is 110 mm, length of foam transport tube is 1 m, and FER is 15

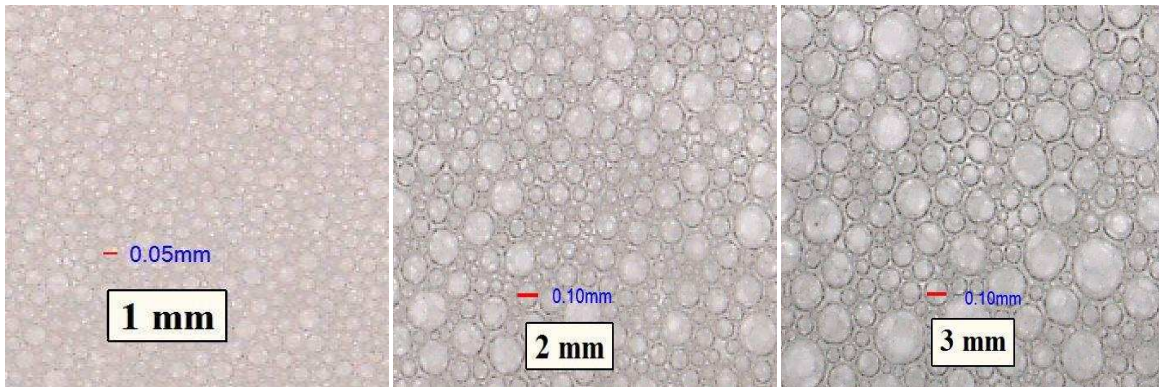


Figure 5.3 Bubble images for three bead diameters at  $V_{avg,air} = \sim 0.4$  m/s. The average bubble diameter for these three cases is shown by red circles in figure 5.2

Figure 5.2 also shows that the average bubble diameter decreases with increase in superficial air velocity. For example, in case of 3 mm beads, the average bubble diameter decreases from 0.11 mm at  $V_{\text{avg,air}} = 0.4$  m/s to 0.075 mm at  $V_{\text{avg,air}} = 0.88$  m/s. This reduction likely occurs because with an increase in superficial air velocity, the pore-scale Reynolds number increases, which leads to increase in pore-scale mixing. Note that we get higher superficial velocities with higher flow rates up to 35 slpm. But we reach a maximum of 25 slpm with 1 mm beads due to the limitation of the system.

The linear fits in figure 5.2 show that the slope of the line decreases as bead size decreases from 3 mm to 1 mm. This shows that the rate of change in bubble diameter with  $V_{\text{avg,air}}$  is decreasing with decrease in bead size. This is likely due to the higher influence of vigorous mixing on the bubble diameter as the bead size increases. Also, bigger bubbles are easy to divide in comparison to smaller bubbles because based on the Young-Laplace law, the pressure inside the larger bubbles is lower compared to the pressure inside the smaller bubbles. As the bubble diameter decreases the pressure inside the bubble increases, and it behaves as a rigid sphere. This makes it more difficult to divide smaller bubbles.

Bubble size distribution is another way of understanding the foam properties such as homogenous bubble size, and foam stability under different flow conditions, and operating parameters. Previous studies on foam bubble size distribution have been performed to understand the foam stability due to drainage, coarsening, and inter-bubble gas diffusion [41], [67], [72], [73]. Generally, we use histograms and bubble frequency plots to understand the bubble size distribution. However, they are difficult to compare with a varying range of bubble sizes even though histograms provide a useful trend for a certain single data-set. Generally, we use histograms and bubble frequency plots to understand the bubble size distribution. However, they are difficult

to compare with a varying range of bubble sizes even though histograms provide a useful trend for a certain single data-set. A more useful way of comparing data is using the log-normal distributions and fitting them in an effective way by normalizing them as probability density functions. The histograms overlaid with their log-normal distributions for all the experiments discussed in section 4.3 to 4.6 are given in appendix B.

For the bubble size distributions in this study, we represent the bubble size data as a probability density functions (PDF) by normalizing the bubble frequency. A probability density function provides the relative likelihood of an event will occur in a single data point in a sample. A PDF is a useful tool for describing the probability of data because it allows the direct comparison of a fit distribution with a histogram. The PDF value of histogram bin is just the probability as a decimal divided by the bin size, which is a relatively simple transformation.

To initially plot the histograms for showing the frequency distribution of bubble diameter, the most important parameter to consider is the bin size. A bin (class interval) is a way of sorting the data in a histogram, and the bin size is usually a function of the number of bins, and the “data range” of the set (the difference between the maximum and minimum bubble diameter). There is no ideal method for selecting the number of bins and the bin size, however, one must consider the three most important data characteristics, which are the data range, and the maximum measured the diameter and the resolution of the measurement (smallest step size of the measurement). In our analysis, the minimum resolution of the measurement is 0.01. Since in most of the cases, the range of the data is twenty times less than the resolution of the measurement, we use a bin size that is equivalent to the data resolution. In case if the data range is greater than 20 times the measurement resolution, we choose a bin size that is a multiple of the resolution. We use a MATLAB code to plot the log-normal distributions and normalize them as PDFs. The log-normal distribution is

basically a function of the mean and the variance of a given data set. We create the log-normal distributions using the “fitdist” function, and create the PDF of that distribution using the “pdf” function in MATLAB.

Figure 5.4 shows the bubble size distribution for 1, 2, and 3 mm beads at  $V_{\text{avg,air}} = 0.4$  m/s. We observe that with a decrease in bead size the distribution becomes narrower, and the peak of the distribution shifts towards the left and grows higher. This indicates that for 3 mm beads there is a wide variation of bubble size from 0.3 to 0.05 mm, and as the bead size reduces to 2 mm and 1 mm, the variation in bubble diameter also decreases. It is clearly evident that the foam bubbles are smaller and homogenous for the case of 1 mm beads.

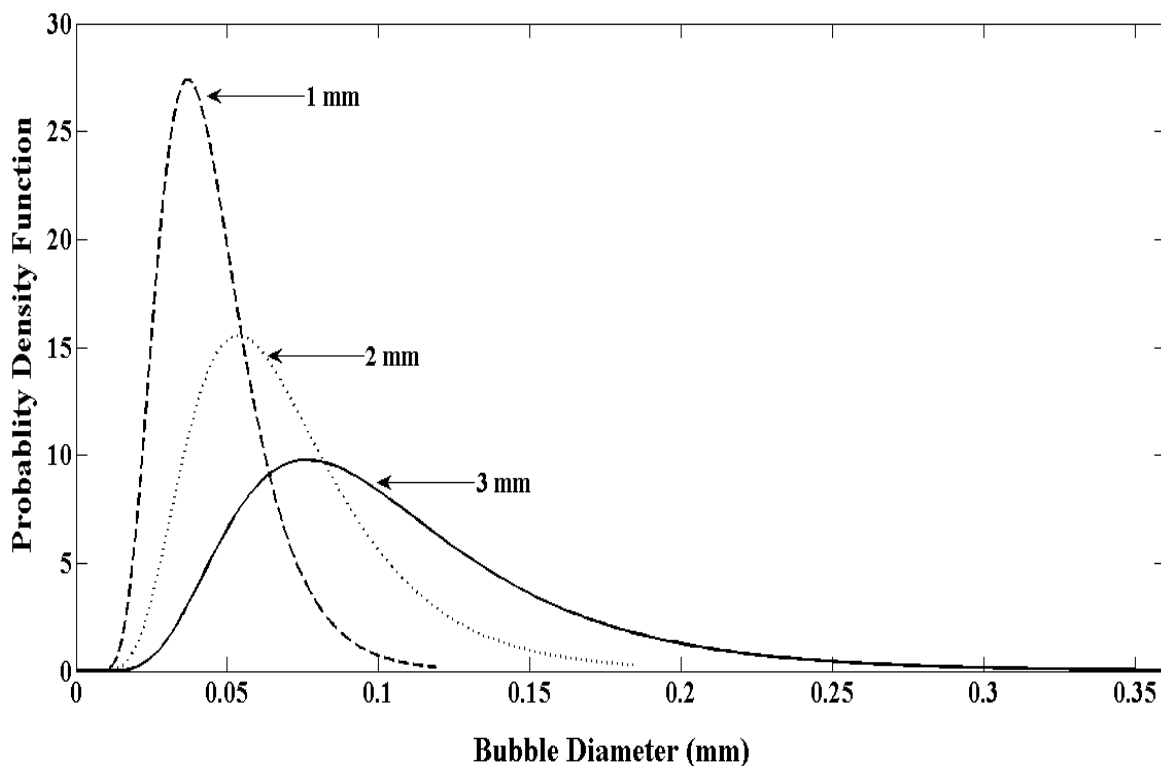


Figure 5.4 Bubble size distribution for the three bead diameters at  $V_{\text{avg,air}} = 0.4$  m/s. These distributions are for the bubble images shown in figure 5.3

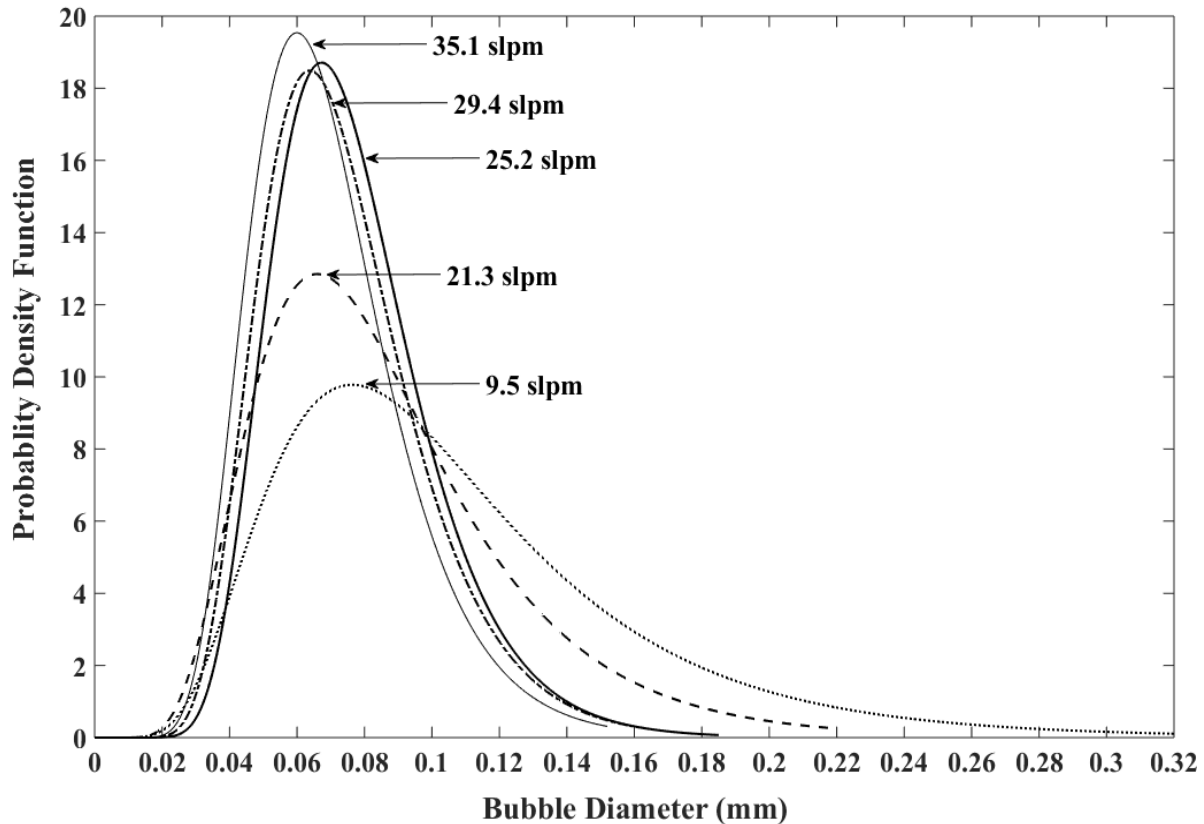
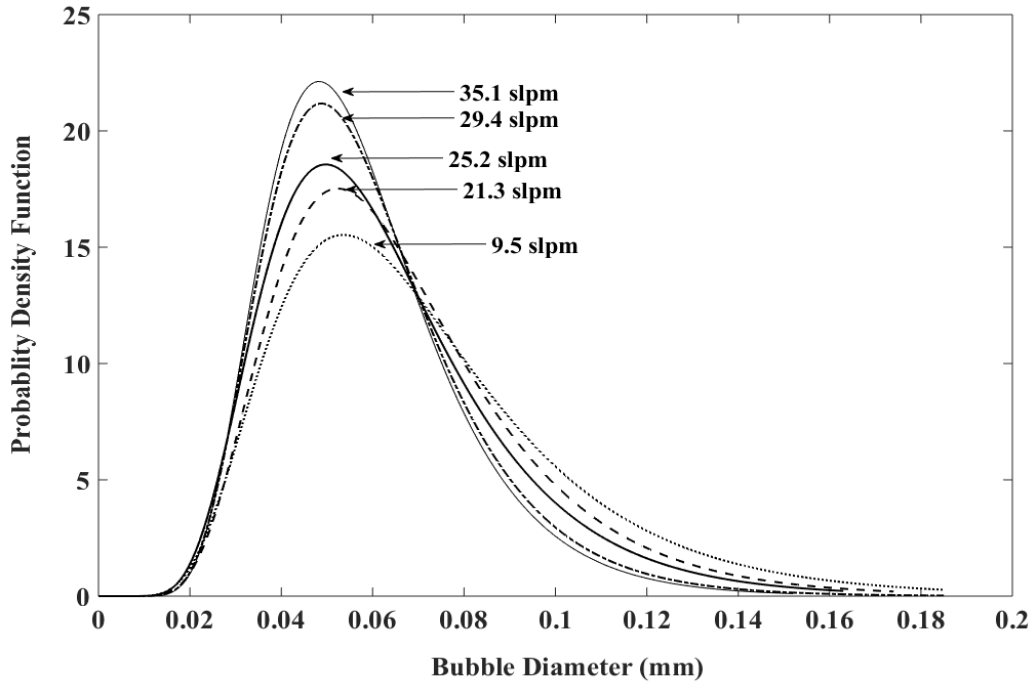
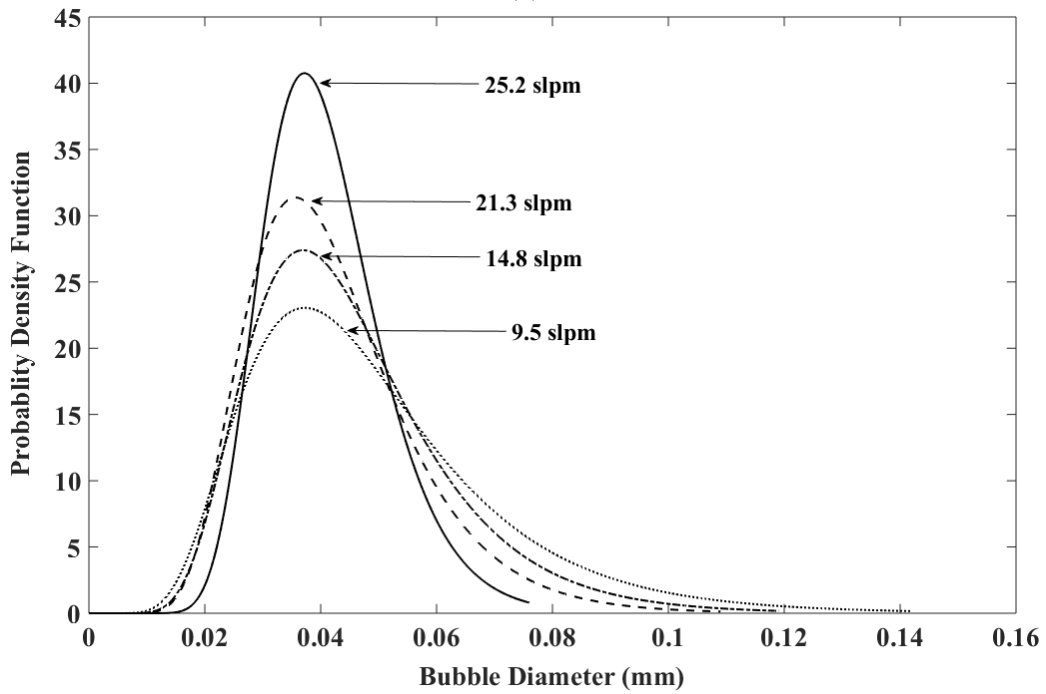


Figure 5.5 Bubble size distribution for foam bubbles generated using 3 mm beads. The length of foam generator is 110 mm, length of transport pipe is 1 m and the FER is 15

Figure 5.5 shows the bubble size distribution for foam bubbles generated using 3 mm beads foam generator for different air mass flow rates. We observe a wide-spread of the distribution at lower flow rates having a wide range of small and large bubbles, for example at  $Q_{\text{air}} = 9.5$  slpm the bubble diameter ranges from 0.05 to 0.3 mm. Note that the peak of the curve for  $Q_{\text{air}} = 9.5$  slpm is at a bubble diameter of 0.08 mm having a probability density of 10 %. As  $Q_{\text{air}}$  increases, the distribution becomes narrower and the peak of curve grows higher, for example at  $Q_{\text{air}} = 35.1$  slpm, the bubble diameter ranges from 0.02 to 0.15 mm, and the peak of the distribution is at 0.05 mm with a probability density of 19 %.



(a)



(b)

Figure 5.6 (a) and (b) Bubble size distribution for 2 mm and 1 mm bead diameter at different air mass flow rates, (a) bubble size distribution for 2 mm beads; (b) bubble size distribution for 1 mm beads. The length of foam generator is 110 mm, length of transport pipe is 1 m

Figure 5.6 (a) and (b) show the bubble size distribution for 2 mm and 1 mm beads respectively. In the case of 2 mm beads in figure 5.6(a), we do not observe a wider distribution for  $Q_{\text{air}} = 9.5$  and 21.3 slpm, in comparison to 3 mm beads. Also, the peaks of the curves are higher in the case of 2 mm compared to 3 mm showing that the occurrence of smaller bubbles is higher for 2 mm bead foam generator. This is because for the same volume of foam generator there will be more number of beads as the bead diameter decreases. This would result in many pores having a smaller size that leads to more developed bubble pattern at the outlet of the foam generator. Also, we see that the distributions become narrow and shift towards the left, suggesting smaller and uniform bubbles. A similar behavior is seen when we compare the distribution for 1 mm in figure 5.6(b) with that of 3 mm. The distribution curves for 1 mm become narrower and shift towards smaller diameter having higher peaks compared to both 2 and 3 mm beads results. This suggests that we could obtain small and homogenous bubbles by decreasing the bead size.

### **5.2.2 Variation of average bubble diameter with length of foam generator**

Figure 5.7 shows the variation of the average bubble diameter with average superficial air velocity for three different lengths of foam generator - 110, 200, and 400 mm. We observe that with increase in the length of transport pipe the average bubble diameter decrease. For example, at  $V_{\text{avg,air}} = \sim 0.4$  m/s, the average bubble diameter for 110, 200, and 400 mm length of generator is approximately 0.11, 0.095, and 0.05 mm respectively. The bubble diameter decrease with increase in the length of the generator because the residence time for the bubble to travel from the inlet to the outlet increases, which leads to the breakdown of bubbles as they travel through a longer tortuous path [74], [75].

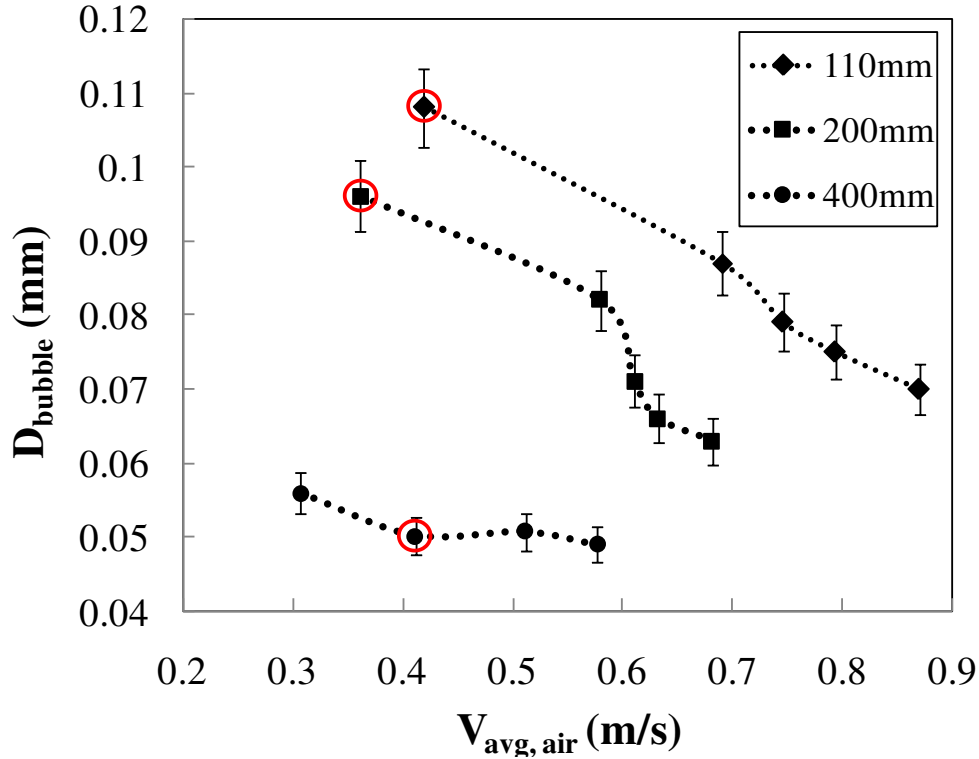


Figure 5.7 Average bubble diameter as a function average superficial air velocity across the generator. The FER is 15, length of foam transport pipe is 1 m, and bead size is 3 mm

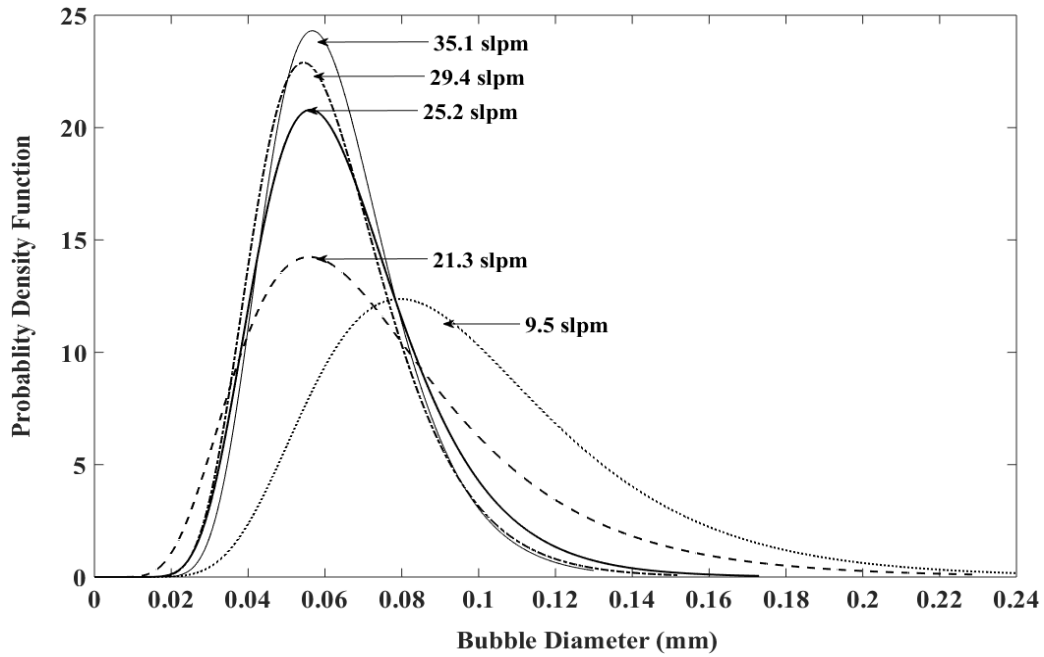
We also observe that the average bubble diameter decreases with average superficial velocity for 110 and 200 mm length of foam generator. For example, with 110 mm foam generator, as the average superficial air velocity increases from 0.41 to 0.87 m/s, the average bubble diameter decreases from 0.11 to 0.07 mm. And for 200 mm length of generator, the average bubble diameter decreases from 0.095 mm at  $V_{avg,air} = 0.35$  m/s to 0.06 mm at  $V_{avg,air} = 0.7$  m/s. This is likely due to pore-scale mixing with increase in the superficial air velocity across the generator [76], [77]. We also observe that with 400 mm length of foam generator the average bubble diameter decreases from 0.055 mm at  $V_{avg,air} = 0.3$  m/s to 0.05 mm at  $V_{avg,air} = 0.6$  m/s. This suggests that we reach a limiting condition for the average bubble diameter with increase in the length of foam generator. This is because as the bubble diameter decreases, the internal pressure inside the bubbles becomes

significantly higher, and the bubbles behave as rigid spheres [78], [79]. As a result, they are difficult to subdivide as they flow through the 400 mm foam generator.

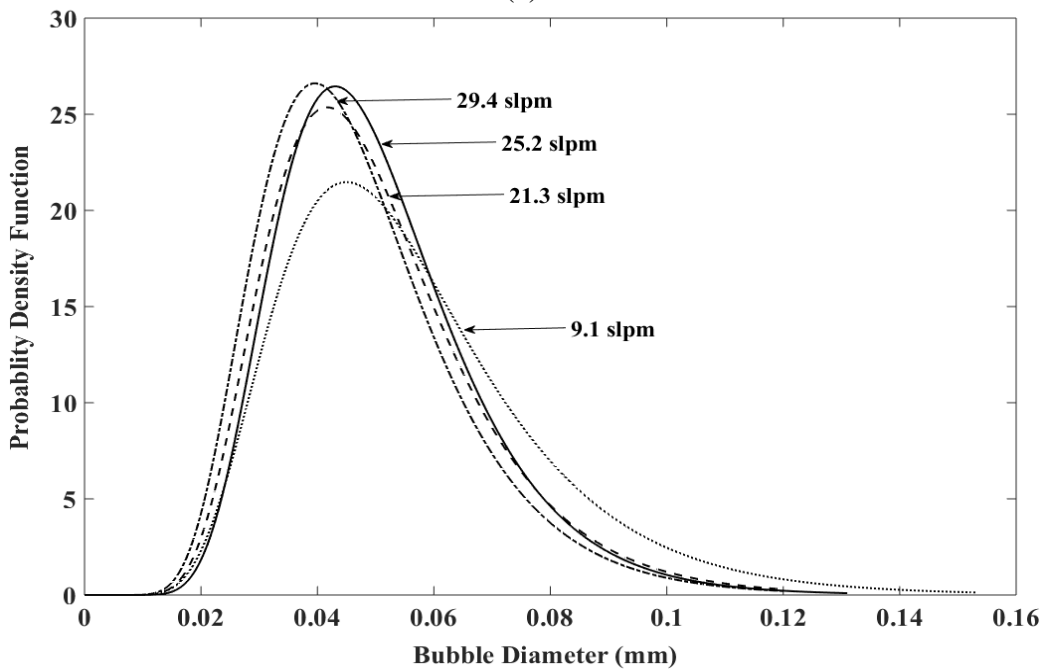
Figure 5.8 (a) and (b) show the bubble size distribution for 200 and 400 mm length of foam generator respectively. In figure 5.8 (a), we see a wide-spread of the distribution for  $Q_{\text{air}} = 9.5$  slpm, and it shifts towards the left for  $Q_{\text{air}} = 21.3$  slpm. A wider distribution suggests a combination of smaller and larger bubbles. For  $Q_{\text{air}} > 21.3$  slpm, the distribution becomes narrower, and its peak moves higher, indicating smaller foam bubbles at higher mass flow rates.

Figure 5.8(b) shows the bubble size distribution for 400 mm length of foam generator. We do not see wider distributions for 400 mm length of foam generator at  $Q_{\text{air}} = 9.5$  slpm. The distribution shifts towards the left in comparison to 110 and 200 mm foam generators. This is because, with increase in the length of foam generator, the bubbles must travel through a longer tortuous path, leading to breakdown/division of larger bubbles into smaller and uniform foam bubbles at the outlet of the generator.

Note that when  $Q_{\text{air}}$  increases from 9.5 to 21.3 slpm, we see that the distribution becomes slightly narrower, and the peak of the curve shifts from 22 to 25 %. This is likely due to the increase in the air mass flow rate, which increases the superficial air velocities through the generator and leads to some level of pore-scale mixing in the generator. However, for  $Q_{\text{air}} > 9.5$  we do not observe a significant change in the distribution. This suggests that the bubble size is highly governed by the length of the porous medium in the generator and not the superficial air velocities.



(a)



(b)

Figure 5.8 Bubble size distributions for a different length of foam generator with varying air mass flow rates, (a) bubble size distribution for 200 mm foam generator; (b) bubble size distribution for 400 mm foam generator. The length of transport pipe is 1 m and bead size is 3 mm.

### 5.2.3 Variation of average bubble diameter with length of foam transport pipe

The variation of the average bubble diameter for the different lengths of foam transport pipe, 1, 3, and 5 m is shown in figure 5.9. We observe that with increase in the length of the foam transport pipe, the average bubble diameter decreases for the same average superficial air velocity.

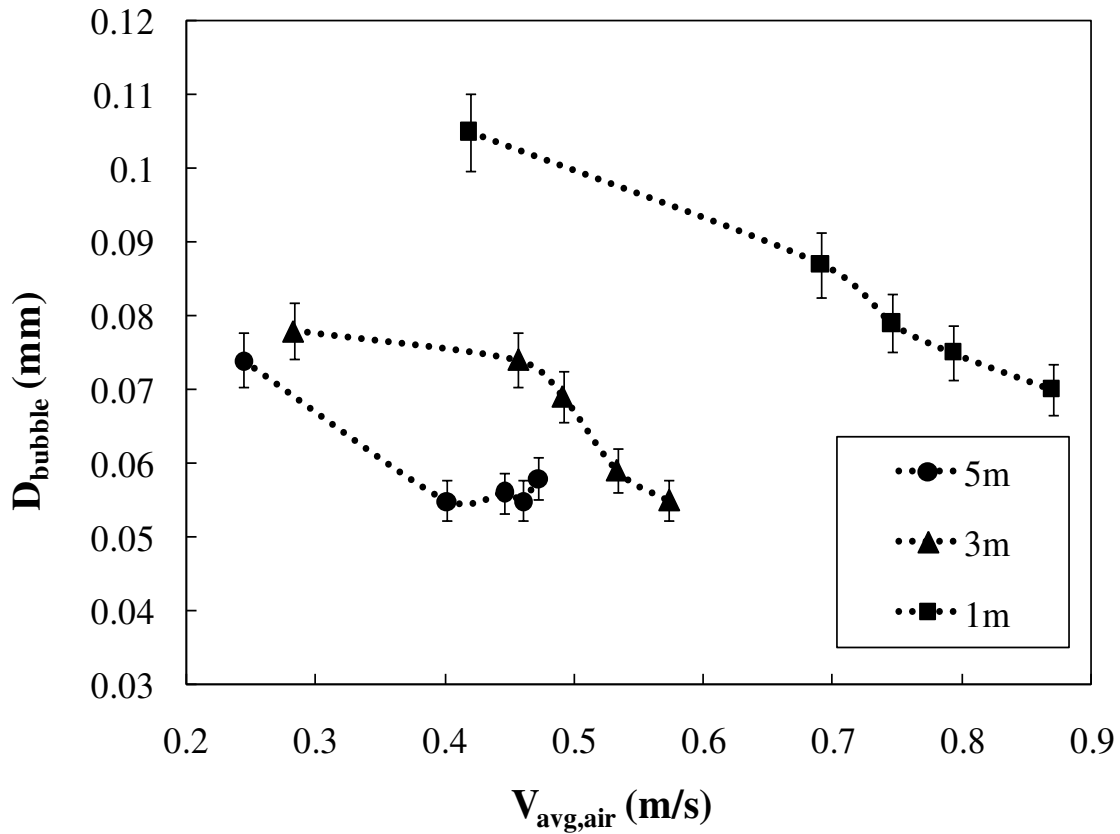


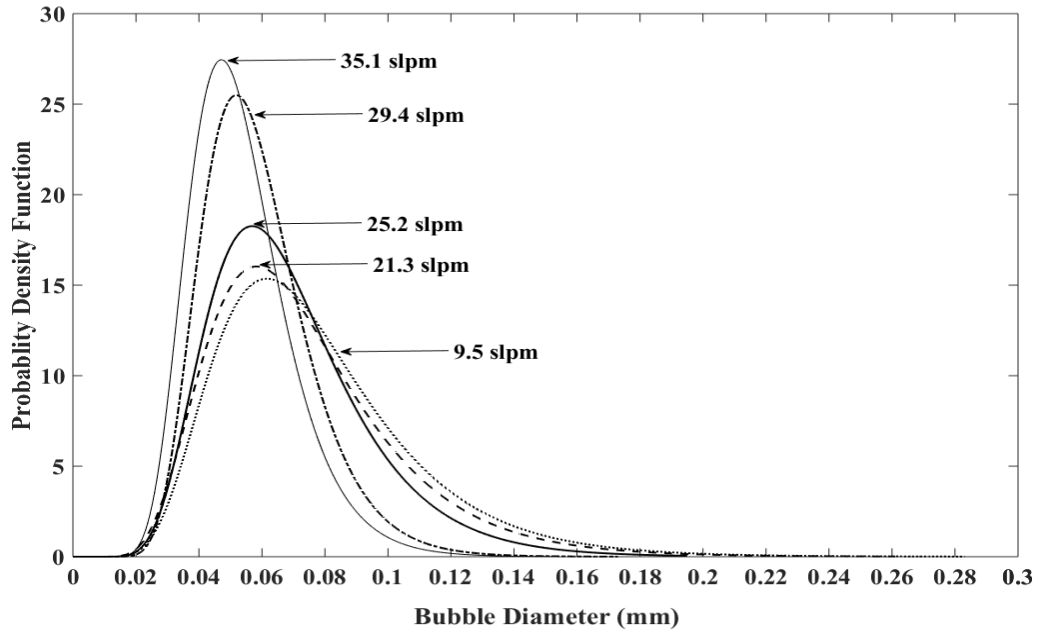
Figure 5.9 Average bubble diameter as a function of average superficial air velocity ( $V_{avg,air}$ ) across the foam generator for different lengths of foam transport pipe. The length of foam generator = 110 mm, and bead diameter = 3 mm

This is because, with increase in the length of transport pipe, the pressure drop through the pipe increases due to increase in the absolute pressure downstream of the foam generator. For example, at  $V_{\text{avg,air}} = \sim 0.4$  m/s, the pressure drop through 1, 3, and 5 m pipe is 90, 300, and 380 kPa respectively. The higher pressure drop is likely due to the smaller bubbles created at the outlet of the foam generator. The behavior has also been reported by Wenzel et al. [21].

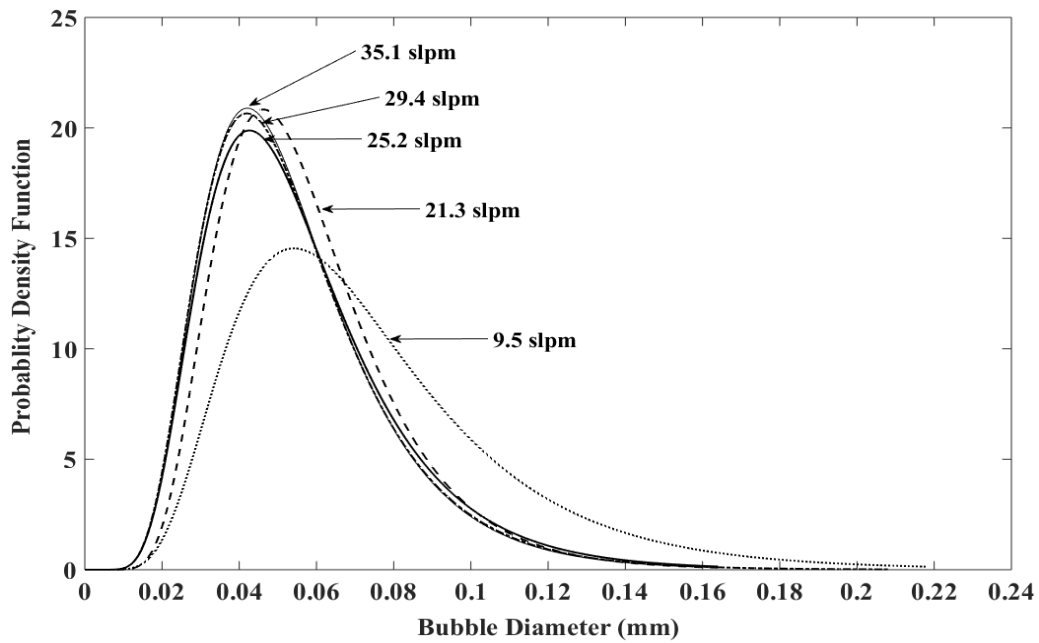
Figure 5.9 also shows that for 5 m transport pipe, as the average superficial air velocity increases, the average bubble diameter tends to decrease initially, and then tends to become constant at approximately 0.05 mm for  $V_{\text{avg,air}} > 0.4$  m/s. This suggests that the initial decrement in bubble diameter with  $V_{\text{avg,air}}$  across the generator is likely due to the pore-scale mixing. And once the bubbles become small enough, the internal pressure of the bubble becomes significantly higher compared to larger bubbles. As a result, after a certain point, the bubble diameter does not decrease any further.

Figure 5.10 (a) and (b) show the bubble size distribution for 3 m and 5 m transport pipe respectively. The distribution for 1 m pipe is shown in figure 5.7. In the case of 3 m transport pipe, we see wide bubble size distributions in figure 5.10(a) for  $Q_{\text{air}} = 9.5$  to 25.2 slpm that indicates the presence of large and small bubbles. As  $Q_{\text{air}}$  increases to 29.4 and 35.1 slpm, the distribution curves become narrower, showing a higher probability of smaller bubbles.

Figure 5.10(b) shows the bubble size distribution for 5 m pipe. The bubble size distribution shifts towards the left (smaller diameter) in comparison to 1 and 2 m pipe. For  $Q_{\text{air}} > 9.5$  slpm, the distribution does not change much indicating that the average bubble diameter does not change much with mass flow rate, and the homogeneity of the bubbles is similar for all flow rates.



(a)



(b)

Figure 5.10 Bubble size distributions for different lengths of foam transport pipe with varying air mass flow rates, (a) Bubble size distribution for 3 m foam transport pipe; (b) bubble size distribution for 5 m pipe. The length of foam gun is 110 mm, and bead size is 3 mm.

### 5.2.4 Variation of average bubble diameter for different chamber pressure

Figure 5.11 shows the average bubble diameter with respect to the average superficial air velocity across the foam generator for chamber pressures - 1, 3, and 5 bar. The data labels indicate the absolute pressure (bar) at which the foam bubbles are captured (outlet of the foam generator).

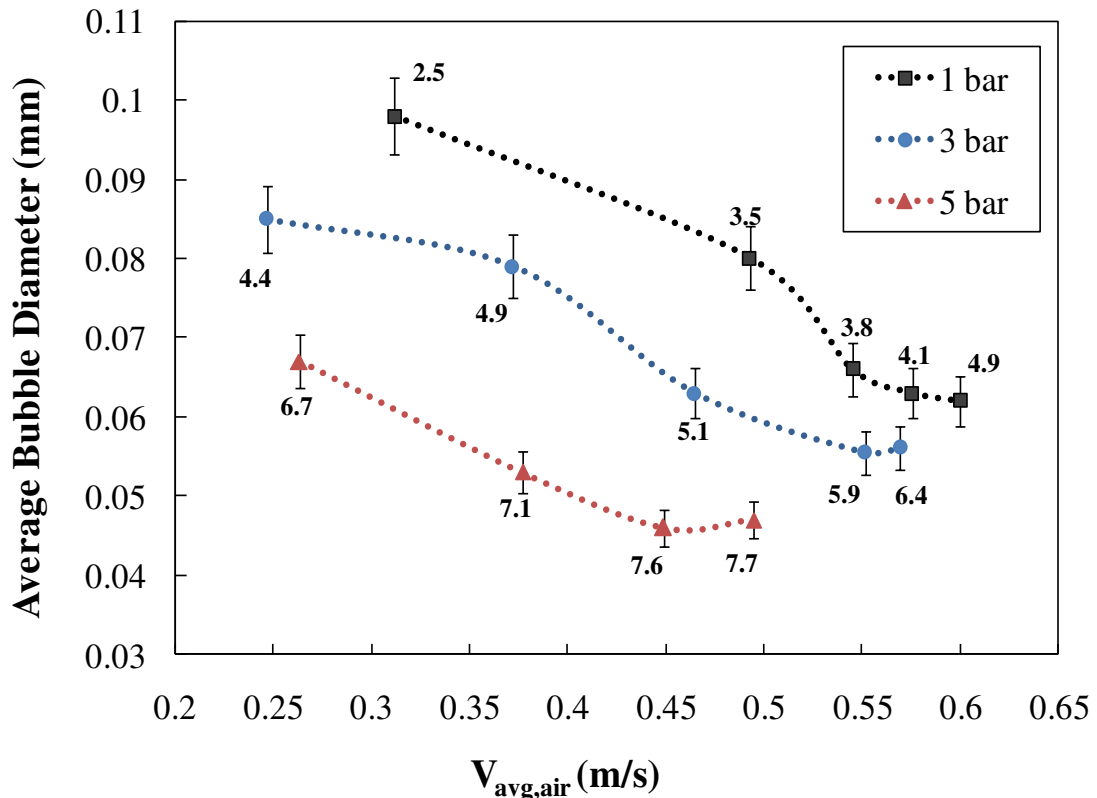


Figure 5.11 Average bubble diameter measured at the outlet of the foam generator when the foam is injected into a pressure chamber under 1, 3 and 5 bar pressure. The length of foam generator is 200 mm, bead diameter is 3 mm and FERp = 15.

Note that FERp is the foam expansion ratio reported at a pressure at which the foam is delivered into the excavation chamber, and it can be referred in section 4.6. As expected, the average bubble diameter decreases with increase in the average superficial air velocity across the generator due to pore-scale mixing.

We also observe that the average bubble diameter decreases with chamber pressure. For example, at  $V_{\text{avg,air}} = \sim 0.45$  m/s, the average bubble diameter for 1, 3, and 5 bar chamber pressure is 0.08, 0.065 and 0.05 mm respectively. This is because the pressure drop through the transport increases and the pressure in the system upstream of the chamber also increases. And to create such high pressure drop through the same length of transport pipe, small foam bubble are required based on the results of Wenzel et al.

Figure 5.12 shows the bubble size distribution for 1 bar chamber pressure. We observe that the distribution is wider for  $Q_{\text{air}} = 9.5$  slpm, and as  $Q_{\text{air}}$  increases, the distributions become narrower, the shift towards left, and their peak also increases. Note that we do not observe a significant change in the distribution for  $Q_{\text{air}} = 25.2$  to 35.1 slpm, though their peaks tend to grow upwards with flow rate.

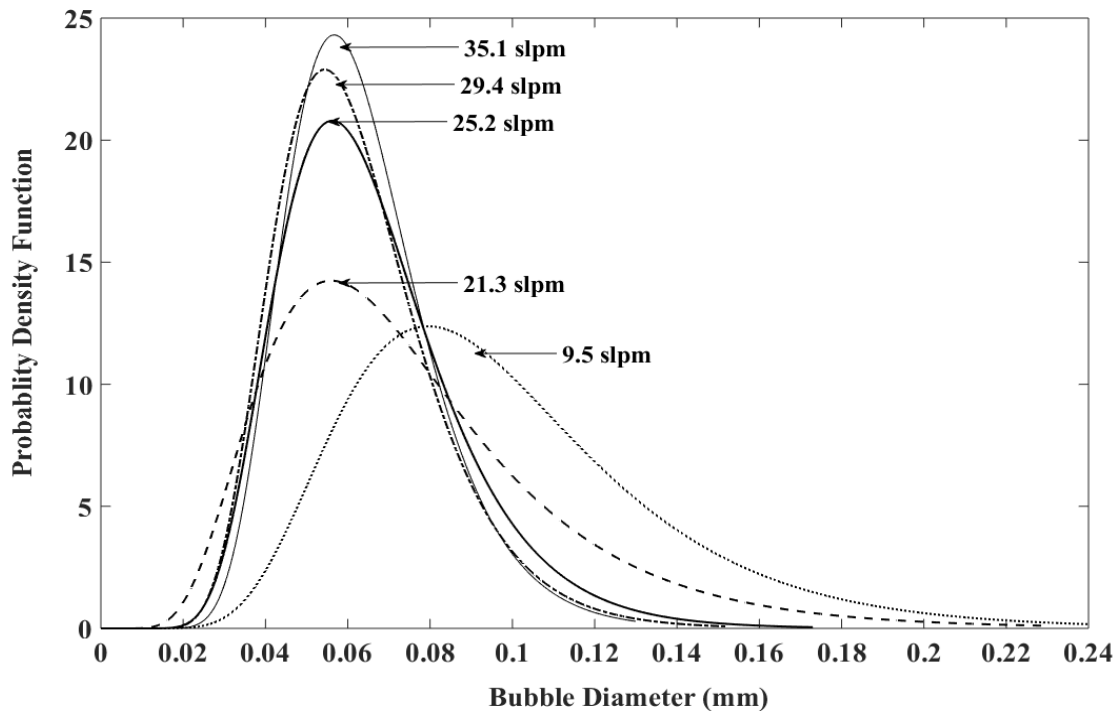
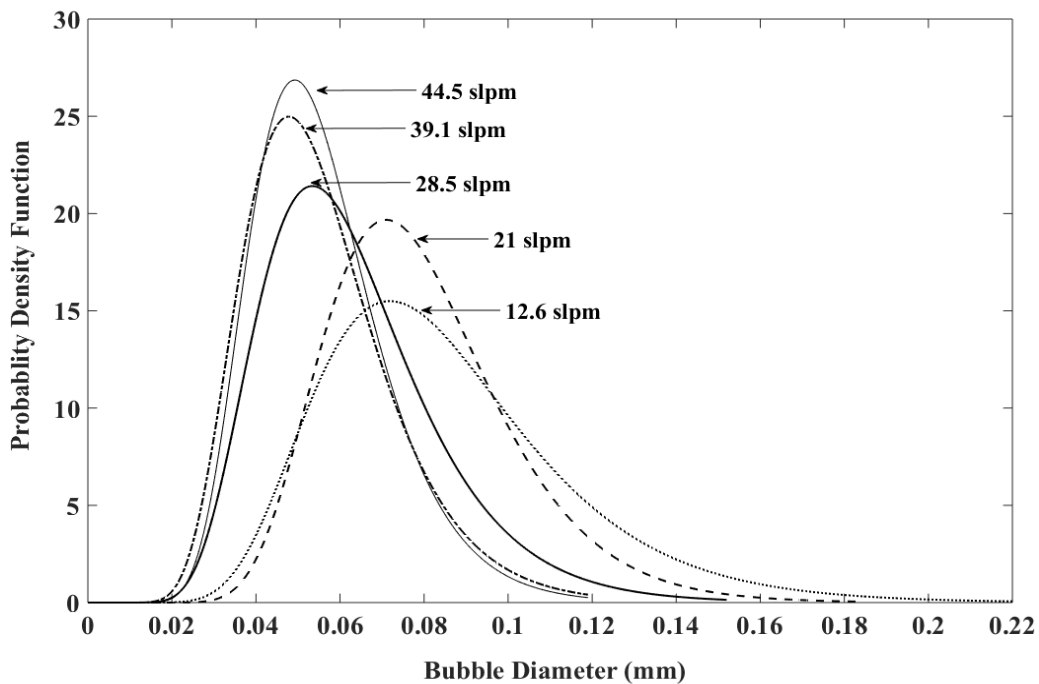


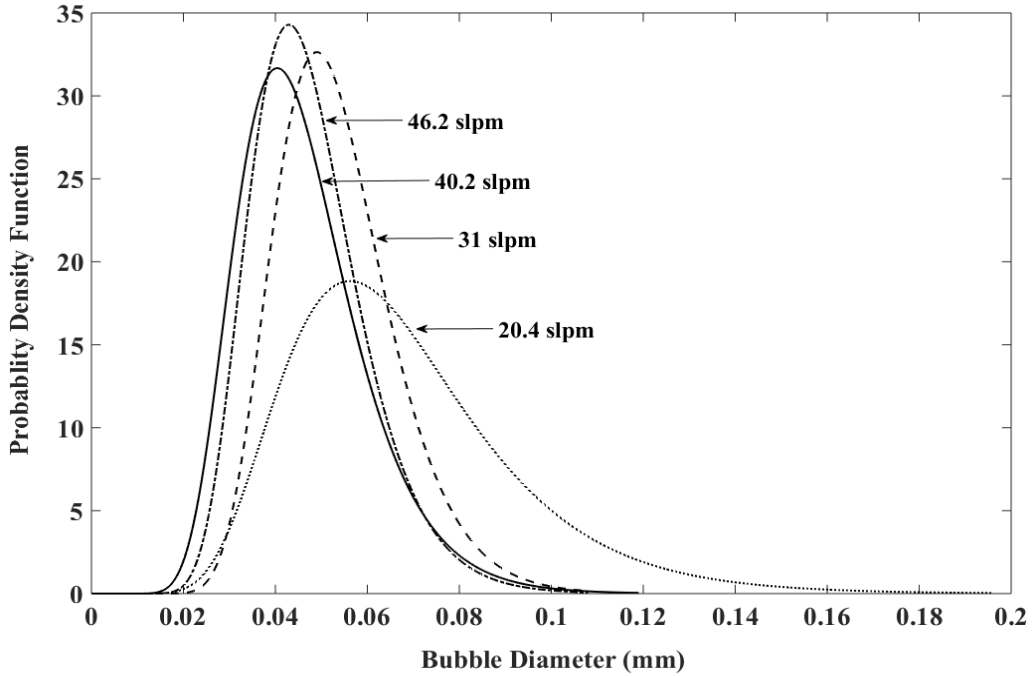
Figure 5.12 Bubble size distribution at 1 bar chamber pressure for various air flow rates. Length of foam gun is 200 mm, length of transport pipe is 1 m, bead size = 3 mm, and FERp = FER = 15

Figure 5.13 (a) and (b) shows the bubble size distribution for 3 bar and 5 bar chamber pressure respectively. We observe that, as we increase the chamber pressure in which the foam is injected, the distribution becomes narrow, and the peak shifts slightly upwards. This is because of the absolute pressures throughout the system increase with chamber pressure, leading to high compression of the same volume of gas, and resulting in smaller bubbles. For example, in the case of 3 bar chamber pressure, for  $Q_{\text{air}} = 21$  and 28 slpm, the distribution gets narrow and peak shifts upwards, in comparison to 1 bar chamber pressure. They tend to become more narrow with a higher peak as we further increase the chamber pressure to 5 bar, as shown in figure 5.13 (b). These results indicate that with increase in chamber pressure the bubble diameter decreases and foam bubbles might become more uniform.



(a)

Figure 5.13 Bubble size distributions for different chamber pressures, (a) bubble size distribution for 3 bar chamber pressure; (b) bubble size distribution for 5 bar chamber pressure. The length of foam generator is 200 mm, bead size is 3 mm, and FER = 15.



(b)  
Figure 5.13 Continued

### 5.3 Foam Compressibility

Foam compressibility is defined as the relative change in the foam volume as a response of change in pressure. Figure 5.14 shows the compressibility of foam for different chamber pressures. We measure the compressibility by loading the chamber pressure by 1 bar. The data points in the plot show the actual values from the experiment, while the dashed lines show the theoretical air compressibility. We observe that the experimental values of foam compressibility match with the theoretical air compressibility. We observe that the experimental values of foam compressibility match with the theoretical air compressibility. This shows that the bubble size does not influence the foam compressibility because smaller bubbles should be less compressible as they have a greater internal pressure compared to larger bubble. We also observe that foam compressibility does not change with air velocity for a given chamber pressure. David and Marsden [48] developed

a relationship of foam compressibility and found that the foam compressibility is equal to the product of foam quality and air compressibility.

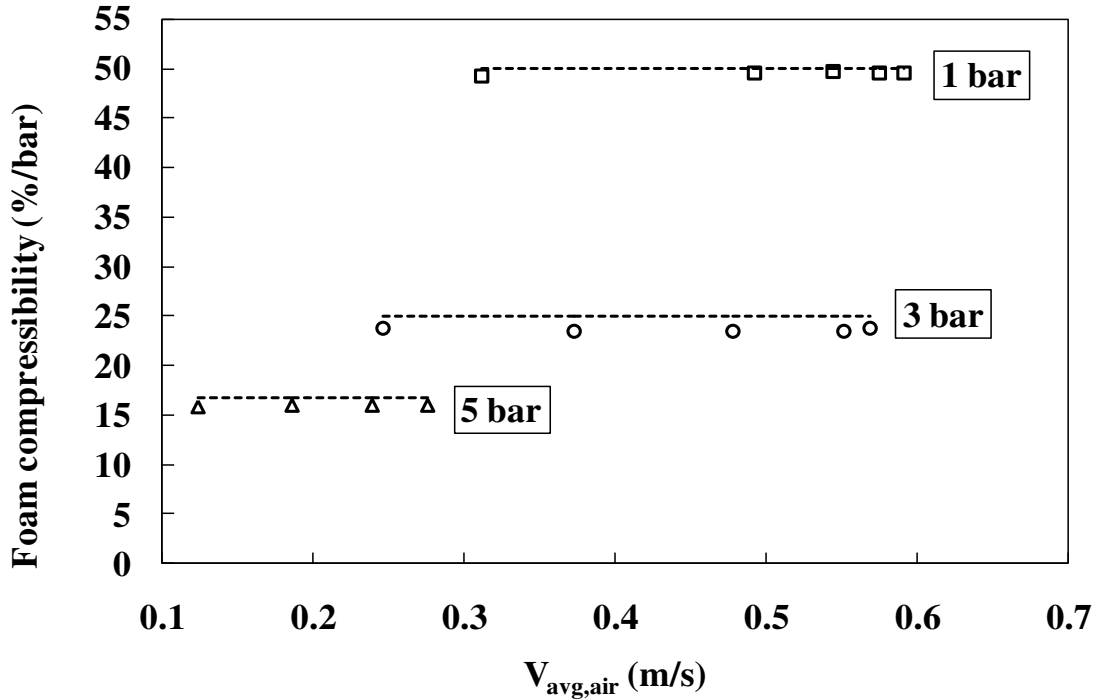


Figure 5.14 Foam compressibility at time = 5 minutes for various range of flow rates at different chamber pressures. The bead size is 3 mm, the length of transport pipe is 1 m, and length of foam generator is 200 mm.

#### 5.4 Foam Drainage

As discussed earlier in chapter 3, we determine foam drainage by measuring liquid volume loss over a time of 30 minutes after foam generation. Figure 5.15 shows the liquid volume loss at various air flow velocities under three chamber pressures. The air velocity has a small influence on stability in that higher velocities lead to more stable foam. The chamber pressure, on the other hand, has a significant influence on stability. Foams generated and deposited into higher pressure environments experience significantly greater stability. The reason for the increased stability is due to the smaller, and more uniform bubbles at higher pressure, which is evident from the bubble

size distribution discussed in section 5.2.4. Smaller and more uniform bubbles are more stable than large bubbles because they do not rupture, or coalesce with neighboring bubbles due to high internal pressure.

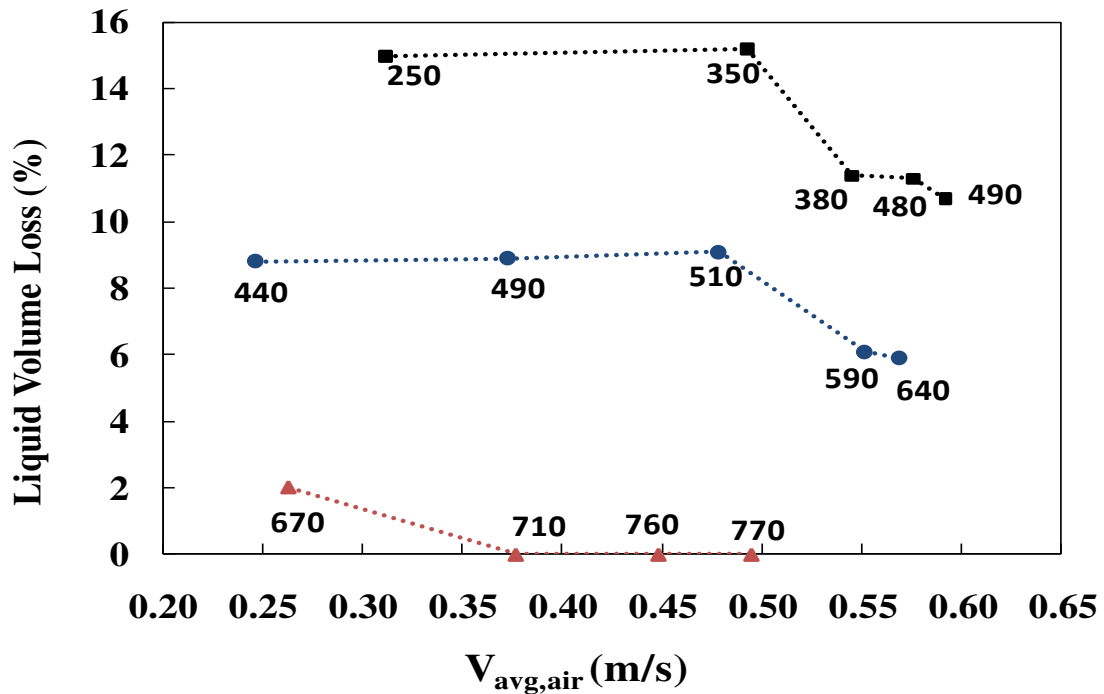


Figure 5.15 Foam liquid volume loss after 30 minutes as a function of the average superficial velocity across the foam generator for different chamber pressure

### 5.5 Variation of foam bubble diameter through transport pipe

We have performed a couple of preliminary tests to understand the variation of foam bubbles through a transport pipe. In the first experiment, we produced foam using a foam generator and allowed it to flow through a 1 m long pipe. The foam bubbles are captured at the inlet and outlet of the transport pipe for the same mass flow rate. The second experiment was performed to understand if we could create foam without a foam generator, and study the variation in foam bubble diameter as the foam flows through the pipe.

For the first experiment, we used a 200 mm long foam generator with 3 mm bead size, and 1 m long transport pipe connected to a pressure chamber at 3 bar. The test was done for  $Q_{\text{air}} = 12.6$  slpm. We observe from the results that when we produce foam using a foam generator and allow it to flow through the transport pipe, the average bubble diameter decreases as the foam flow from the inlet to the outlet of the pipe. The average bubble diameter is  $\sim 0.08$  mm at the inlet and decreases to  $\sim 0.06$  mm at the outlet. Note that we obtain similar results when the chamber pressure is at 1 bar (atmospheric condition).

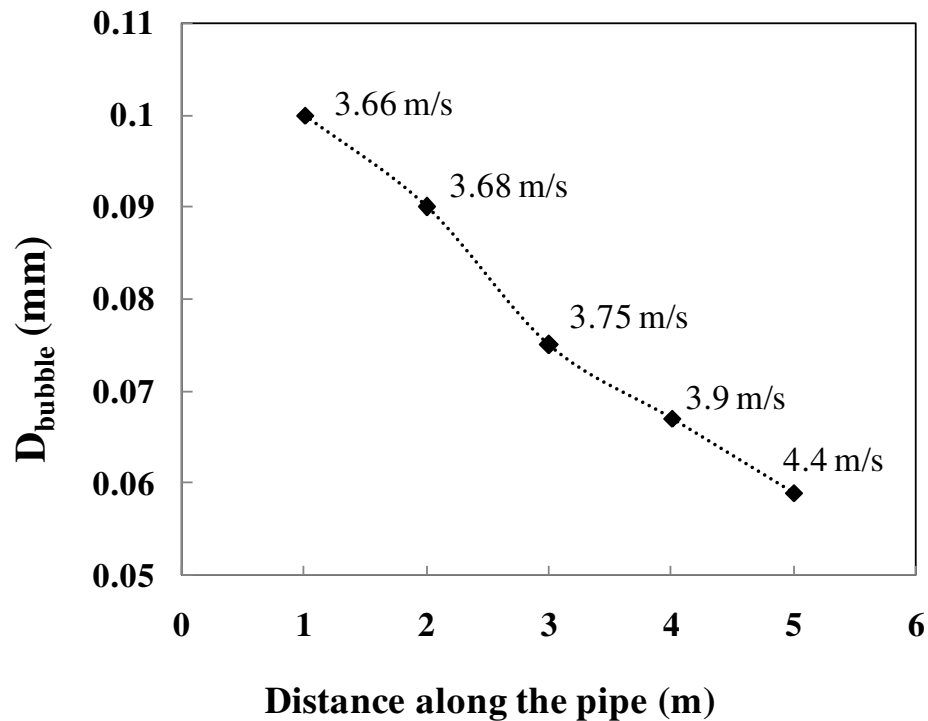


Figure 5.16 Average bubble diameter at every 1 m distance through a 5 m long transport pipe. The data labels indicate the average foam velocity at that instance. Foam is produced without a foam generator.

For the second experiment, we did not use a foam generator to produce foam. Initially we allowed the air and surfactant solution mixture to flow through a 1 m long transport pipe; however, we did not get foam at the outlet of a 1 m pipe. Hence, we replaced the 1 m transport pipe with a

5 m pipe. Note that the 5 m long transport pipe was connected to a pressure chamber at 3 bar. We allowed the air and surfactant solution mixture to flow through the 5 m pipe, and observed that we could create foam without a foam generator at the outlet of the pipe. In order to understand the foam bubble transformation process, we captured foam at every 1 m distance along the 5 m pipe. We provided plumbing connections at five locations to bleed off foam. A foam capture device with a back pressure regulator were used to capture foam at the respective outlet pressure. Figure 5.16 shows the variation in the average bubble diameter as a function of the average foam velocity in the pipe. We capture bubble images at every 1 m distance. As the foam flows through the pipe the average bubble diameter decreases from 0.1 mm at  $V_{\text{avg,foam}}^{\text{pipe}} = 3.7 \text{ m/s}$  to 0.06 mm at  $V_{\text{avg,foam}}^{\text{pipe}} = 4.4 \text{ m/s}$ .

Dimensional analysis is a technique that is used to reduce the complexity of an experimental setup, and increase the generality of the experimental information. Dimensional analysis leads to a group of non-dimensional terms that can provide information on the flow regimes, or ratios of different properties that could influence the outcome of the experiment. In case if a system has many parameters, then dimensional analysis helps in reducing the number of parameters in form of pi-terms. Dimensional analysis is also used for scaling large experiments into a smaller form, for example one can scale the wings of an aircraft and testing the airfoil wings in a laboratory [80].

Our experimental setup is a complicated system with various parameters. For better understanding of these parameters we carry out an exploratory study to perform a dimensional analysis after the experiments have been performed. Based on the physical intuition of the system and the brute-force analysis, we now carry out a posteriori dimensional analysis of our system. We perform the dimensional analysis of the generator and transport pipe separately.

### **6.1 Dimensional analysis for foam generator**

One way of carrying out the dimensional analysis is by using the Buckingham Pi theorem. First, we list all the variables of the experiment and determine the independent and dependent variables. For our system the differentiation between dependent and independent is not necessarily obvious. Consider for example the foam generator system shown in figure 6.1, where air and liquid enter separately from the right and foam exits at the left. One could imagine fixing  $P_{in}$  and  $P_{out}$  in

which case  $\dot{m}_A$  and  $\dot{m}_L$  are dependent variables. Though, in this case the ratio of  $\dot{m}_A$  and  $\dot{m}_L$  would be the required independent variables.

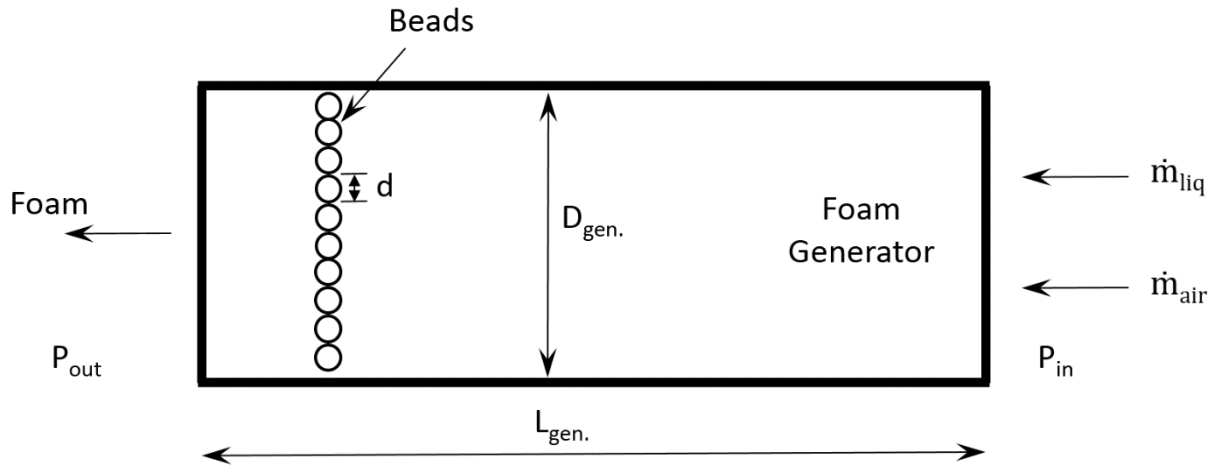


Figure 6.1 Foam generator with different parameters considered for dimensional analysis

For our analysis we consider  $\dot{m}_A$  and  $\dot{m}_L$  to be independent variables because this reflects our experimental procedure. Due to compressibility, we also consider  $P_{in}$  and  $\rho_A$  to be controlled independent variables. In that case  $P_{out}$  and foam velocity becomes the dependent variable. For ease of analysis, we replace  $\dot{m}_A$  and  $\dot{m}_L$  with the superficial inlet velocities  $V_A^{in}$  and  $V_L$ . This gives us the velocities scales that are easier to work with.

For the case of our generator, the obvious independent variables are liquid density ( $\rho_L$ ), air density at the inlet of the generator ( $\rho_A$ ), dynamic viscosity of liquid ( $\mu_L$ ), dynamic viscosity of air ( $\mu_A$ ), diameter of the foam generator ( $D_{gen.}$ ), bead diameter ( $d$ ), generator length ( $L_{gen.}$ ), surface tension ( $\sigma$ ), and contact angle ( $\theta$ ) between solid, liquid, and air. The less obvious independent variables are inlet air velocity ( $V_A^{in}$ ) liquid velocity ( $V_L$ ), and inlet pressure ( $P_{in}$ ). The independent variables that have not been considered for this study are the surfactant concentration, and temperature (isothermal conditions). The surfactant concentration is not included because it is

considered in the liquid density and surface tension. The dependent variables are the pressure drop through the transport pipe ( $\Delta P_{\text{pipe}}$ ), the bubble diameter ( $D_{\text{bubble}}$ ), and average foam velocity ( $V_{\text{avg}}^{\text{foam}}$ ). We consider them as dependent variables because they result from the change in pressure and velocity through the porous media. Considering again the experimental measurement of  $\Delta P$  in figure 6.1, the functional relationship is,

$$\Delta P = f(\rho_L, \rho_A, \mu_L, \mu_A, D_{\text{gen.}}, d, L_{\text{gen.}}, \sigma, \theta, V_A^{\text{in}}, V_L, P_{\text{in}}) \quad (6.1)$$

Then we select the repeating variables from the list of independent variables that include the dimensions of length, mass, and time. As repeating variables for this analysis we choose  $V_A^{\text{in}}$ ,  $d$ , and  $\rho_A$ . We choose the bead diameter because our experiments show that it plays a dominant role in creating the foam bubbles. We select the inlet air velocity because we consider high expansion foams and our experiments also show that air velocity more closely relates to the foam velocity than the liquid velocity. For the same reason we choose the density of air, because it closely matches to the actual foam density.

Using the repeating variables  $V_A^{\text{in}}$ ,  $d$ , and  $\rho_A$  to non-dimensionalize the relation in equation 6.1, we find that

$$\frac{\Delta P}{0.5 \rho_A (V_A^{\text{in}})^2} = f \left\{ \frac{\rho_L}{\rho_A}, \frac{\mu_L}{\rho_A V_A^{\text{in}} d}, \frac{\mu_A}{\rho_A V_A^{\text{in}} d}, \frac{D_{\text{gen.}}}{d}, \frac{L_{\text{gen.}}}{d}, \theta, \frac{\sigma}{\rho_A (V_A^{\text{in}})^2 d}, \frac{V_L}{V_A^{\text{in}}}, \frac{P_{\text{in}}}{0.5 \rho_A (V_A^{\text{in}})^2} \right\} \quad (6.2)$$

The first non-dimensional term on the right-hand side is the ratio of liquid density to the inlet air density. The second and the third terms represent  $1/Re$ , where  $Re$  is the Reynolds number, which is the ratio of the inertial forces to viscous forces. The fourth and fifth terms give the ratio of the length and diameter of the generator. The contact angle ( $\theta$ ) is already in a non-dimensional form.

The seventh term,  $\frac{\sigma}{\rho_A (V_A^{in})^2 d}$ , represents  $1/We$  where  $We$  is the Weber number, which is the ratio of the inertial forces to interfacial tension. The last two terms are the ratios of velocity and pressure respectively.

The non-dimensional relation in equation 6.2 is not necessarily the most practical. However, any pi-term can be replaced with a product of powers between itself and the other pi-terms. In this way we can rewrite equation 6.2 as,

$$\frac{\Delta P}{P_{in}} = f \left\{ \frac{\rho_L}{\rho_A}, \frac{\mu_L}{\mu_A}, \frac{\rho_A V_A^{in} d}{\mu_A}, \frac{D_{gen.}}{d}, \frac{L_{gen.}}{d}, \theta, \frac{\mu_L V_A^{in}}{\sigma}, \frac{V_L}{V_A^{in}}, \frac{P_{in}}{0.5 \rho_A (V_A^{in})^2} \right\} \quad (6.3)$$

In this form, we replace  $0.5 \rho_A (V_A^{in})^2$  with  $P_{in}$  so that it gives us a better idea about the variation of pressure in the generator. As there are two Reynolds number in equation 6.2, we use the Reynolds number having the air viscosity and velocity, because air velocity plays a dominant role in generating the inertial forces through the generator. For simplicity, we convert the Reynolds number equation with the term of liquid viscosity to the ratio of liquid to air viscosities. We also replace the Weber number with the capillary number because the liquid viscosity plays a major role in creating the thin films during bubble formation. The capillary number measures the relative importance of viscous forces over the interfacial tension.

## 6.2 Reynolds number and flow regimes in the foam generator

A major objective of our study is to characterize the flow regimes in the foam generator. As discussed in chapter two for example, single phase flow through porous media exhibits a Darcy regime dominated by viscous effects, a Forchheimer regime in which inertial effects become important, and finally, a turbulent regime. Transition between these regimes is typically characterized by some Reynolds number.

As discussed in chapter 2, we observe different flow regimes through porous media. There is Darcy regime that is observed at low velocities, where viscous effects are dominant in governing the flow. As the flow velocities increase, the inertial effects tend to become more dominant than the viscous effects, and the flow transitions to Forchheimer regime. Note that in both the Darcy and Forchheimer regime, the flow is laminar. Further increasing the velocities lead to a transition to turbulent flow. Based on the literature, different characteristic lengths area used to compute the Reynolds number of the flow through porous media. The bead diameter and the square root of permeability are commonly used in literature.

For our system, the choice of Reynolds number is not obvious. As a first attempt we begin by computing the local Reynolds number for air and liquid. We first compute the local Reynolds number for air flow through the porous media using the bead diameter as the characteristic length, as shown in equation 6.4,

$$Re_{d,air} = \frac{\rho_A V_A^{in} d}{\mu_A}. \quad (6.4)$$

We consider only one set of experiments, for which the bead size is 3 mm, the length of the generator is 110 mm, and length of transport pipe is 1 m, as discussed in section 4.3. The Reynolds number for air flow using the bead diameter varied from 170 to 640. Similarly, we compute the Reynolds number for liquid flow as shown in equation 6.5. We choose the air density because it is a better representative of foam density. Also, we select the velocity of air, because it likely represents the velocity of the two-phase mixture through the porous media. The local Reynolds number for liquid flow varies as 1.5 to 2.9.

$$Re_{d,liq} = \frac{\rho_A V_A^{in} d}{\mu_L}. \quad (6.5)$$

In literature, studies have reported Reynolds number using the square root of permeability ( $k$ ). The square root of permeability is preferred because it more accurately characterizes the pore length scale. Note that we experimentally determine the permeability of 3 mm beads by flowing water at low velocities through the porous material. We find that the permeability for 3 mm beads is  $2.5E-9 \text{ m}^2$ . Table 6.1 shows the permeability and porosity for the respective bead diameters.

Table 6.1 Permeability and porosity for bead diameter 1, 2, and 3 mm. Both permeability and porosity are determined experimentally by performing repeated number of tests

Bead Size (mm)	Permeability ( $\text{m}^2$ )	Porosity
1	1.7E-10	0.31
2	8.6E-10	0.33
3	2.5E-09	0.36

We compute the Reynolds number using the square root of permeability as,

$$Re_k = \frac{\rho_A V_A^{\text{in}} \sqrt{k}}{\mu_L}. \quad (6.6)$$

We use the inlet air velocity because it closely represents the foam velocity through the porous media. We choose the viscosity of liquid because it represents the viscosity of foam in a better manner compared to the viscosity of air. The Reynolds number in this case varies as 1.58 to 4.7.

The Darcy, Forchheimer, and turbulent regimes are well understood for single-phase flows, though there remains some debate [81]–[86]. For multiphase flows, the literature is comparatively scarce [87]. Because this is foam flows, it is attractive to treat it as an effective single-phase fluid characterized by an effective Reynolds number,

$$Re_{\text{eff}} = \frac{\rho_{\text{foam}}^{\text{avg}} V_{\text{avg,foam}}^{\text{gen}} \sqrt{k}}{\mu_{\text{eff}}}. \quad (6.7)$$

And the effective viscosity can be computed using the Darcy equation,

$$\mu_{\text{eff}} = \frac{k \Delta P}{V_{\text{avg,foam}}^{\text{gen.}} L_{\text{gen.}}} \quad (6.8)$$

The Reynolds number for all the four cases discussed above are given in the table 6.2,

Table 6.2 Reynolds number for air and liquid flow through porous media based on the particle diameter and permeability. The minimum and maximum values are computed based on the flow velocities

Approach	Reynolds Number	Minimum	Maximum
Particle Diameter	$Re_{d,\text{air}} = \frac{\rho_A V_A^{\text{in}} d}{\mu_A}$	170	620
	$Re_{d,\text{liq}} = \frac{\rho_A V_A^{\text{in}} d}{\mu_L}$	1.5	2.9
Permeability	$Re_k = \frac{\rho_A V_A^{\text{in}} \sqrt{k}}{\mu_L}$	0.02	0.05
Effective Single-phase fluid	$Re_{\text{eff}} = \frac{\rho_{\text{foam}}^{\text{avg}} V_{\text{avg,foam}}^{\text{gen.}} \sqrt{k}}{\mu_{\text{eff}}}$	1.58	4.70

Previous studies in literature show different Reynolds number for transition of flow from Darcy to Forchheimer regime, and Forchheimer to turbulent regime, when the Reynolds number is computed using the particle diameter [54], [64], [81], [82], [88], [89]. In the case of single-phase flow through porous media the fluid flow transitions from a linear Darcy regime to a non-linear Forchheimer regime as the Reynolds number becomes greater than one ( $Re_d > 1$ ). This behavior is due to the dominance of inertial forces compared to viscous effects. It is also suggested in some studies that the flow transitions to a non-Darcy regime at a critical Reynolds number of 3 to 10 [81], [83], [84], [86], [89], while other studies suggested  $Re_d = 40$  to 150 as the critical Reynolds

number for non-Darcy flow [90]. Bagci et al. [64] experimentally flowed liquid at different velocities through 3 mm beads and observed that the Darcy regime exists for a range of Reynolds number at  $0.9 < Re_d < 23$ , the Forchheimer regime at  $68 < Re_d < 233$ , and the turbulent regime at  $Re_d > 268$ .

Zeng et al. [81] has summarized the critical Reynolds number for transition of flow from Darcy to non-Darcy regime, when the Reynolds number ( $Re_k$ ) is computed using the permeability and the non-Darcy coefficient. He suggested that the critical value for non-Darcy flow vary from 0.01 to 0.2. Bagci et al. [64] computed the Reynolds number using the square root of permeability and observed different value for the transition of flow regimes. He suggested that the Darcy regime is observed for range of Reynolds number form  $0.02 < Re_k < 0.6$ , the Forchheimer regime at  $1.81 < Re_k < 6.21$ , and turbulent regime at  $Re_k > 7.2$ .

It should be noted that these studies are for single phase flow through porous media, and it is still debatable what characteristic length-scale is suitable for computing the Reynolds number. In case of a two-phase flow, it becomes more complicated because two fluids with different densities flow through the porous medium. Since this is a preliminary study, it is difficult to comment on the exact flow regime through the foam generator based on the computed Reynolds number. We can likely suggest that the flow is in the non-Darcy regime, where there are both viscous and inertial effects, and the inertial effects play a dominant role. Also, based on the visual observations, we see a chaotic behavior of the air-liquid mixture through the porous media with considerable flow through the walls due to edge effects, suggesting the dominance of inertial effects.

### 6.3 Dimensional analysis for foam transport pipe

As mentioned earlier, the dimensional analysis of the foam transport pipe is carried out separately from the foam generator. We consider the same case as discussed in the analysis of the generator in which the bead size is 3 mm, the length of generator is 110 mm, the length of transport pipe is 1 m, and the chamber pressure is atmospheric. In the case of the transport pipe, the independent variables are the air and liquid viscosities ( $\mu_A$ ,  $\mu_L$ ), diameter of the pipe ( $D_{\text{pipe}}$ ), length of pipe ( $L_{\text{pipe}}$ ), density of liquid ( $\rho_L$ ), density of air at the outlet of pipe ( $\rho_A^{\text{out}}$ ), surface roughness ( $\varepsilon$ ), air velocity at the outlet of pipe ( $V_A^{\text{out}}$ ), liquid velocity at the outlet of pipe ( $V_L^{\text{out}}$ ), chamber pressure ( $P_{\text{ch.}}$ ) at the outlet of the pipe, surface tension ( $\sigma$ ), and contact angle in between the pipe walls, liquid and air ( $\Theta$ ). We consider the pressure drop through the pipe  $\Delta P_{\text{pipe}}$  as the dependent variable, and  $D_{\text{pipe}}$ ,  $V_A^{\text{out}}$ , and  $\rho_A^{\text{out}}$  are the repeating variables.

Considering again the experimental measurement of  $\Delta P_{\text{pipe}}$ , the functional relationship is,

$$\Delta P = f(\rho_L, \rho_A^{\text{out}}, \mu_L, \mu_A, D_{\text{pipe}}, L_{\text{pipe}}, \sigma, \theta, \varepsilon, V_A^{\text{out}}, V_L^{\text{out}}, P_{\text{ch.}}) \quad (6.9)$$

The non-dimensional form using the repeating variables is obtained in a similar way as it was obtained for the case of foam generator,

$$\frac{\Delta P}{P_{\text{ch.}}} = f \left\{ \frac{\rho_L}{\rho_A^{\text{out}}}, \frac{\mu_L}{\mu_A}, \frac{\rho_A^{\text{out}} V_A^{\text{out}} D_{\text{pipe}}}{\mu_A}, \frac{\varepsilon}{D_{\text{pipe}}}, \frac{L_{\text{pipe}}}{D_{\text{pipe}}}, \theta, \frac{\mu_L V_A^{\text{out}}}{\sigma}, \frac{V_L}{V_A^{\text{out}}}, \frac{P_{\text{ch.}}}{0.5 \rho_A^{\text{out}} (V_A^{\text{out}})^2} \right\} \quad (6.10)$$

As mentioned earlier, the choice of Reynolds number is not obvious for our system, so we first compute the local Reynolds number for air obtained from the dimensional analysis,

$$Re_{d,\text{air}} = \frac{\rho_A^{\text{out}} V_A^{\text{out}} D_{\text{pipe}}}{\mu_A} \quad (6.11)$$

The Reynolds number varies from 1783 to 6574, for varying flow rates from 9.5 to 35.1 slpm. Similarly, one can compute the Reynolds number by replacing the air viscosity with the liquid viscosity, because the liquid viscosity compares better with the foam viscosity. So the Reynolds could be computed using equation 7.2. The Reynolds number varies from 37 to 137.

$$Re_d = \frac{\rho_A^{\text{out}} V_A^{\text{out}} D_{\text{pipe}}}{\mu_L}. \quad (6.12)$$

However, since this is foam flow through pipe, one can treat the foam as an effective single-phase fluid characterized by an effective Reynolds number,

$$Re_{\text{eff}} = \frac{\rho_{\text{avg,foam}}^{\text{pipe}} V_{\text{avg,foam}}^{\text{pipe}} D_{\text{pipe}}}{\mu_{\text{eff}}}. \quad (6.13)$$

Since we use the foam generator to create foam, we could treat the generator as a viscometer and use the effective foam viscosity computed in the foam generator. Based on equation 7.3, the Reynolds number for foam flow through pipe varies from 590 to 2039.

Previous studies in literature have focused on foam flow through pipes, however, they use different methods to compute the Reynolds number of the flow, and it is also not clear how to compute an effective foam viscosity [22], [51]. Briceno et al. used the liquid viscosity and velocity to compute the Reynolds number for foam flow through pipes and channels [52]. As a part of a preliminary study, we computed the Reynolds number for the foam flow through pipe, and we can only suggest that the flow could be in the transition regime at high flow rates based on the critical Reynolds number (2000 to 2500) suggested by Blauer et al. [22]. The investigation of the flow regimes would be a part of the future studies.

### 7.1 Summary of key findings

We performed an experimental study of foam generation on underground tunnel boring machines (TBM). For this purpose, we built a laboratory scale foam generation machine that mimics the system on the TBM's. Foam is generated by flowing a mixture of pressurized air and water through a foam generator filled with randomly packed beads. As the mixture flows through the generator, foam is produced in the generator, and obtained at the outlet of the generator. The foam is further transferred into a pressure chamber using a transport pipe.

We carried out a parametric study in which we varied the mass flow rate of air and liquid between their minimum and maximum allowable values while maintaining a constant foam expansion ratio ( $FER = 15$ ), a constant surfactant concentration (5 %), and a fixed generator diameter ( $D_{gen.} = 15.2$  mm). We systematically varied the bead size as (1, 2, 3 mm), the length of the transport pipe as (1, 3, 5 m), the length of the foam generator as (110, 200, and 400 mm), and the chamber pressure as (1, 3, 5 bar). The influence of these conditions and the operating parameters (mass flow rates, pressures, and superficial velocities) were experimentally investigated.

From our experimental results it was observed that with increase in the air flow rates, the pressures and the velocities tend to increase across the foam generator. We observed that the pressure at the inlet of the generator is higher than the pressure at the outlet, and as a result the velocities tend to increase from the inlet to the outlet. This is because with decrease in pressure the air expands and its density decreases. Also, it was noted that the pressures at the outlet of the

generator was governed by the downstream conditions of the transport pipe. The pressures in the system are built up due to the outlet conditions of the pipe (chamber pressure), which further influence the pressures at the inlet and outlet of the generator. It was also observed that with increase in flow rates, the foam bubble diameter decreased. This was likely due to increase in the pore-scale Reynolds number that lead to pore-scale mixing through the generator.

The experimental study using different bead size showed that with decrease in bead size, the pressures through the system tend to increase because the resistance to the flow increases or the permeability decreases. It was observed that the foam bubble size decrease with decrease in bead size because the pore size reduces. It was also noted that the slopes of the variation of bubble diameter with air velocity decreases as the bead size decrease from 3 mm to 1 mm. This likely suggested that the pore-scale mixing dominated the bubble size for 3 mm, while, pore size played a major role in governing the bubble size for 1 mm beads. Similar results as Wenzel et al. [21] were observed, in which the foam bubbles decrease with increase in velocity that lead to high pressure drops through the transport pipe.

In the case of different lengths of foam generator, high pressure drops were observed across the generator with increase in the length of the generator. This was because the mixture has to flow through a longer tortuous path with increase in length of generator. Also, the residence time for the flow through the generator increased. It was also observed that with increase in the length of the foam generator, the foam bubble size decreased. One possible explanation for this result is with increase in the length of generator the residence time for the flow increase, and as a result the large bubbles tend to subdivide into smaller bubbles due to increased pore-scale mixing. For the case of 400 mm generator it was observed that the foam bubbles remained nearly constant with increase in velocity. We hypothesize that once the foam bubbles become smaller, the internal

pressure inside the bubbles becomes significantly higher and the bubbles tend to behave as rigid spheres. Hence, they further do not subdivide with increase in velocity.

Similarly, when the length of transport pipe was varied, the absolute pressures upstream of the transport pipe increased significantly. This resulted in higher pressure drops through the pipe because with increase in the length of pipe, the resistance for the flow increases, and as a result more energy was expended in terms of pressure loss to flow from inlet to the outlet of the pipe. It was also observed that the bubbles decreased with increase in the length of pipe. This could be due to expansion of air across the foam generator in which it was observed that bubbles expand nearly 3 times more in the generator for the case of 1 m pipe than for 5 m pipe. This suggests that pressures play a significant role in governing the size of the foam bubbles.

We have hypothesized a combination of three mechanisms that would lead to foam generation through porous media. The first mechanism shown in figure 7.1 suggests that the foam bubbles subdivide as they flow downstream the generator. This could be due to the decrease in the bead size (pore size), increase in velocities (pore-scale mixing), and increase in the length of generator. The second mechanism shown in figure 7.2 suggests that there is a minimum bubbles diameter, which is likely because the small bubbles behave as rigid spheres and do not subdivide further. Conversely, the third mechanism shown in figure 7.3 suggests that the foam bubbles increase as they flow downstream the generator. This is likely due to the expansion of bubbles across the generator from high to low pressure.

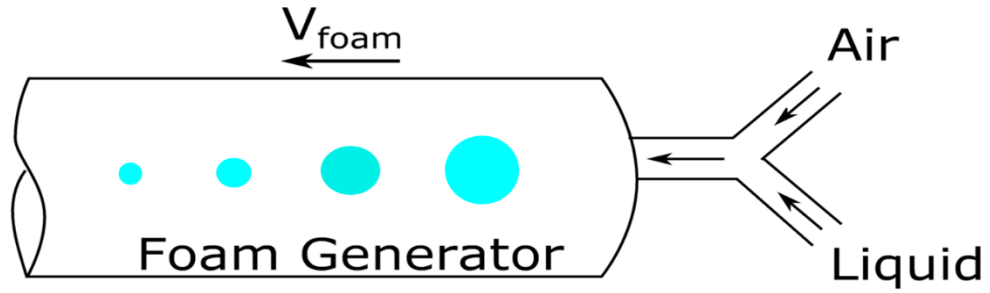


Figure 7.1 Subdivision of foam bubbles as they flow downstream of the generator

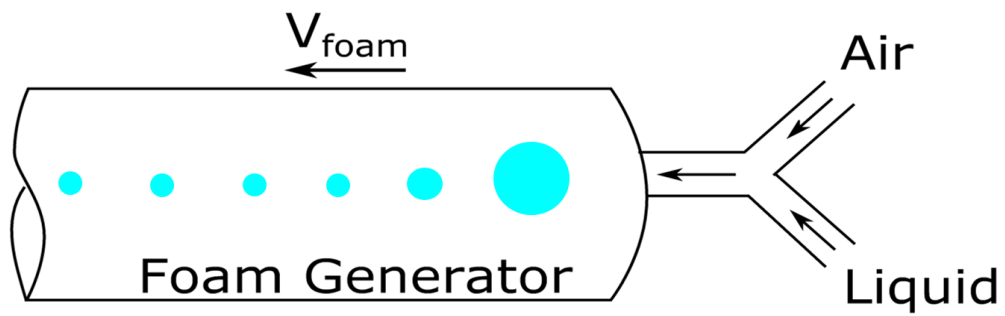


Figure 7.2 Limitation in the minimum bubble diameter

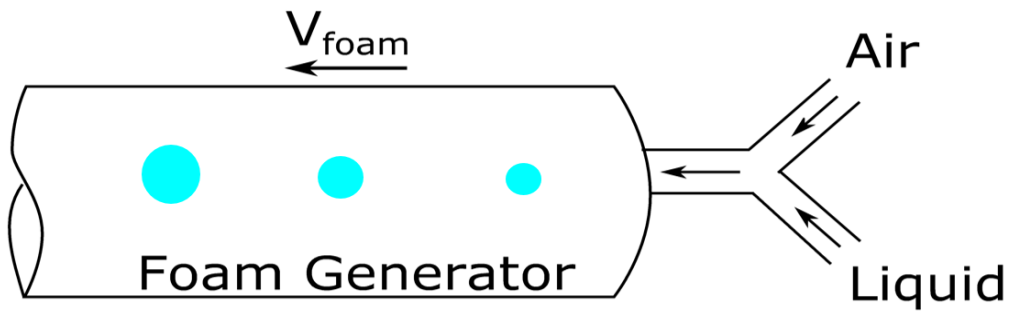


Figure 7.3 Expansion of foam bubbles as they flow downstream of the generator

The pressure chamber tests provided an actual idea about the behavior of foam in the excavation chamber, when it was injected under pressure. The chamber pressures had a significant influence on the average foam bubble diameter. The bubble diameter reduced with increase in the chamber pressure, and this may be due to less expansion of foam bubbles with increase in chamber pressure. A non-linear behavior of pressure drop as a function of average foam velocity is observed for the pipe and generator respectively. Foam compressibility was investigated for the same tests, and it was observed that the foam compressibility decreases with increases in chamber pressure. The foam compressibility matches the theoretical air compressibility and the foam bubble size do not influence the foam compressibility. The foam stability increased with increase in the chamber pressure. This is likely due to small and uniform foam bubbles at high chamber pressures. And also the rate of inter-bubble diffusion decreases as the bubbles become small and uniform. It was also observed that foam stability increases at higher flow velocities.

The diameter of the transport pipe was also varied, and it was observed that the pressure drop through the transport pipe decreases with increase in pipe diameter. One could qualitatively suggest that with increase in the pipe diameter, the Reynolds number and the surface roughness decreases and result into smaller pressure drop. This result matches with results shown by Raza et al. [46] and David et al.[48], and they suggest that the foam viscosity decreases with increase in the pipe diameter, and lead to smaller pressure drops.

Our preliminary studies indicated that the foam can be generated without a foam generator. In our study, we generated foam by flowing the mixture of air and surfactant solution through a 5 m long transport pipe. This was likely due to vigorous mixing through the pipe because the foam velocity increase as it flows downstream of the pipe.

Dimensional analysis was carried out for the foam generator and the transport pipe to determine the flow regimes using the Reynolds number. Based on the values of the Reynolds number one can suggest that the flow through the porous media follows a non-Darcy regime where the inertial effects are more dominant than the viscous effects. In the case of foam flow through transport pipe, the results were inconclusive because it is unclear from literature regarding an appropriate critical Reynolds number for foam flow through pipes.

Overall, these findings will be helpful to the tunneling community and other researchers. It will also provide an understanding of the foam generation mechanism for varying system parameters. Further, it will also enable researchers to understand the impact on foam properties when the foam is injected into a chamber under pressure.

## **7.2 Recommendation for Future Work**

The following is a list of recommended future studies:

- a. The impact of foam generator diameter should be studied to completely understand the foam generation system on a TBM
- b. Foam rheology should also be investigated for a better understanding of foam properties that relate to foam flow through pipes.
- c. The preliminary test for generating foam without foam generator should be carried for a wide range of flow rates, and transport pipe to determine the flow regime for foam generation.
- d. Foam bubbles should be analyzed at the outlet of the transport pipe because the bubble diameter decreases as foam flows through a longer pipe.

## REFERENCES

- [1] EFNARC, “Specification and Guidelines for the use of specialist products for Mechanised Tunnelling ( TBM ) in Soft Ground and Hard Rock,” 2005.
- [2] S. Psomas, “Properties of Foam / Sand Mixtures for Tunnelling Applications,” University of Oxford, 2001.
- [3] D. Peila, “Soil conditioning for EPB shield tunnelling,” *J. Civ. Eng.*, vol. 18, pp. 831–836, 2014.
- [4] M. Á. P. Duarte, “Foam as a soil conditioner in tunnelling: physical and mechanical properties of conditioned sands,” University of Oxford, 2007.
- [5] A. S. Merritt, “Conditioning of clay soils for tunnelling machine screw conveyors,” University of Cambridge, 2005.
- [6] E. Farrokh and J. Rostami, “Effect of adverse geological condition on TBM operation in Ghomroud tunnel conveyance project,” *Tunn. Undergr. Sp. Technol.*, vol. 24, pp. 436–446, 2009.
- [7] B. Herzhaft, S. Kakadjian, and M. Moan, “Measurement and modeling of the flow behavior of aqueous foams using a recirculating pipe rheometer,” *Colloids Surfaces A Physicochem. Eng. Asp.*, vol. 263, pp. 153–164, 2005.
- [8] M. Thewes, C. Budach, and A. Bezuijen, “Foam conditioning in EPB tunnelling,” *Geotech. Asp. Undergr. Constr. Soft Gr. - 7th Int. Symp.*, pp. 127–135, 2011.
- [9] G. Milligan, L. Erickson, P. Raleigh, V. Romero, A. Sramoon, and M. Okazaki, “Lubrication and Soil Conditioning in Tunneling, Pipe Jacking, and Microtunneling,” *Rev. Lit. Arts Am.*, vol. 44, pp. 1–46, 2000.
- [10] M. Mooney, N. Tilton, D. Parikh, and Y. Wu, “EPB TBM Foam Generation,” in *Rapid Excavation and Tunneling Conference*, 2017.
- [11] L. L. Schramm, *Emulsions, Foams, and Suspensions: Fundamentals and Applications*. 2006.
- [12] M. Mooney, Y. Wu, D. Parikh, and L. Mori, “Granular Soil Conditioning under Pressure,” in *9th Intl. Symp. Geotechnical Aspects of Underground Construction in Soft Ground*, 2017.
- [13] L. Mori, “Advancing understanding of the relationship between soil conditioning and earth pressure balance tunnel boring machine chamber and shield annulus behavior,” Colorado School of Mines, 2016.
- [14] S. Quebaud, M. Sibai, and J.-P. Henry, “Use of chemical foam for improvements in drilling by earth-pressure balanced shields in granular soils,” *Tunn. Undergr. Sp. Technol.*, vol. 13,

- pp. 173–180, 1998.
- [15] L. Mori and M. Mooney, “Laboratory Tests to determine the Relationship between Pressure and Foam Conditioned Sand Behavior in EPB Tunneling,” *Tunnels Undergr. Sp. Technol.*, 2017.
  - [16] Y. Wu and M. Mooney, “An experimental examination of foam stability for EPB TBM tunneling,” *Tunn. Undergr. Sp. Technol.*, 2017.
  - [17] M. Thewes and C. Budach, “Konditionierung von Lockergesteinen bei Erddruckschilden,” *Geomech. und Tunnelbau*, vol. 3, no. 3, pp. 256–267, 2010.
  - [18] A. Bezuijen, M. Hajialilue-bonab, H. Sabetamal, S. Psomas, and G. T. Houlsby, “Experimental study on foamed sandy soil for EPBM tunnelling,” *Proc. Undergr. Constr.*, vol. 2, pp. 128–138, 2001.
  - [19] C. Budach and M. Thewes, “Application ranges of EPB shields in coarse ground based on laboratory research,” *Tunn. Undergr. Sp. Technol.*, vol. 50, pp. 296–304, 2015.
  - [20] M. Mooney, Y. Wu, L. Mori, R. Bearce, and M. Cha, “Earth Pressure Balance TBM Soil Conditioning: It’s About the Pressure,” in *World Tunnel Congress*, 2016.
  - [21] H. Wenzel, T. Stelson, and R. Brungraber, “Flow of High Expansion Foam in Pipes,” *Am. Soc. Civ. Eng.*, vol. 93, pp. 153–165, 1967.
  - [22] R. E. Blauer, B. J. Mitchell, and C. A. Kohlaas, “Determination Transitional of Laminar , Foam Flow Turbulent , Losses in and,” *44th Annu. Calif. Reg. Meet.*, 1974.
  - [23] N. N. Thondavadi and R. Lemlich, “Flow properties of foam with and without solid particles,” *Ind. Eng. Chem. Process Des. Dev.*, vol. 24, pp. 748–753, 1985.
  - [24] J. R. Calvert, “Pressure drop for foam flow through pipes,” *Int. J. Heat Fluid Flow*, vol. 11, pp. 236–241, 1990.
  - [25] J. R. Calvert, “The flow of foam through constrictions,” *Int. J. Heat Fluid Flow*, vol. 9, pp. 69–73, 1988.
  - [26] M. Bogdanovic, R. N. Gajbhiye, and S. I. Kam, “Experimental study of foam flow in horizontal pipes: Two flow regimes and its implications,” *Colloids Surfaces A Physicochem. Eng. Asp.*, vol. 344, pp. 56–71, 2009.
  - [27] B. S. Gardiner, B. Z. Dlugogorski, and G. J. Jameson, “Prediction of Pressure Losses in Pipe Flow of Aqueous Foams,” *Ind. Eng. Chem. Res.*, vol. 38, pp. 1099–1106, 1999.
  - [28] W. Drenckhan and A. Saint-Jalmes, “The science of foaming,” *Adv. Colloid Interface Sci.*, vol. 222, pp. 228–259, 2015.
  - [29] W. Hanselmann and E. Windhab, “Flow characteristics and modelling of foam generation in a continuous rotor/stator mixer,” *J. Food Eng.*, vol. 38, no. 4, pp. 393–405, 1998.

- [30] P. Stevenson, *Foam Engineeing: Fundamentals and Applications*. Wiley, 2012.
- [31] P. Valkó, M. J. Economides, and A. Texas, “Foam Proppant Transport,” *Soc. Pet. Eng.*, vol. 12, pp. 1–6, 1997.
- [32] T. Eren, “Foam Characterization: Bubble Size and Texture Effects,” Middle East Technical University, 2004.
- [33] D. B. Ingham and I. I. Pop, *Transport phenomena in porous media*. Pergamon, 1998.
- [34] J. J. Bikerman, *Foams*, First. Springer-Verlag Berlin Heidelberg, 1973.
- [35] A. M. Kraynik, “Foam Flows,” *Annu. Rev. Fluis Mech.*, vol. 20, pp. 325–327, 1988.
- [36] I. Cantat *et al.*, “Foams: Structure and Dynamics,” *Clim. Chang. 2013 - Phys. Sci. Basis*, vol. 1, pp. 1–278, 2013.
- [37] H. C. Cheng and R. Lemlich, “Theory and experiment for interbubble gas diffusion in foam,” *Ind. Eng. Chem. Res.*, vol. 24, pp. 44–49, 1985.
- [38] W. Janna, *Design of Thermal Fluid Systems*, Third Edit. CL Engineering, 2009.
- [39] H. F. John, “University Microfilms, A Xerox Company, Ann Arbor, Michigan,” 1967.
- [40] J. R. Calvert, “A rheological model for a liquid,” vol. 7, pp. 164–168, 1986.
- [41] J. R. Calvert and K. Nezhati, “Bubble size effects in foams,” *Int. J. Heat Fluid Flow*, vol. 8, pp. 102–106, 1987.
- [42] P. C. Harris, “Effects of Texture of Foam Fracturing Fluids,” *SPE Prod. Eng.*, pp. 249–257, 1989.
- [43] J. O. Sibree, “The Viscosity of Froth,” *Trans. Faraday Soc.*, vol. 26, pp. 26–36, 1933.
- [44] M. Blackman, “On Transformation of Solid Foam to Fluid Foam under shear,” 1946.
- [45] C. Grove, G. E. Wise, W. C. Marsh, and J. B. Gray, “Viscosity of Fire-Fighting Foam,” *Ind. Eng. Chem. Process Des. Dev.*, vol. 43, pp. 1120–1122, 1950.
- [46] H. Raza and S. . Marsden, “The Streaming Potential and Rheology of Foam,” *Soc. Pet. Eng. J.*, pp. 859–868, 1967.
- [47] M. Mooney, “Explicit Formulas for Slip and Fluidity,” *J. Rheol. (N. Y. N. Y.)*, vol. 2, no. 2, p. 210, 1931.
- [48] A. David and S. S. Marsden, “The Rheology of Foams,” in *Society of Petroleum Engineers Journal*, 1969, p. 11.
- [49] H. Wenzel, R. Brungraber, and T. Stelson, “The Viscosity of High Expansion Foam,” *J. Mater.*, vol. 5, pp. 396–412, 1970.

- [50] V. N. Feklistov, "Calculating the hydraulic resistance of foam flows in tubes," vol. 39, pp. 1066–1069, 1981.
- [51] G. A. Okpobiri and C. U. Ikoku, "Experimental Determination of friction Factors for Mist and Foam Drilling and Well Clean out Operations," *J. Energy Resour. Technol.*, vol. 105, pp. 542–553, 1983.
- [52] M. I. Briceno and D. D. Joseph, "Self-lubricated transport of aqueous foams in horizontal conduits," *Int. J. Multiph. Flow*, vol. 29, pp. 1817–1831, 2003.
- [53] J. R. Calvert, "Pressure drop for foam flow through pipes," *Int. J. Heat Fluid Flow*, vol. 11, pp. 236–241, 1990.
- [54] J. L. Lage, "The Fundamental Theory of Flow through Permeable Media from Darcy to Turbulent," in *Transport Phenomena in Porous Media*, 1998, pp. 1–30.
- [55] T. C. Ransohoff and C. J. Radke, "Mechanisms of Foam Generation in Glass-Bead Packs," *Soc. Pet. Eng. J.*, pp. 573–585, 1988.
- [56] W. R. Rossen, "A critical review of Roof snap-off as a mechanism of steady-state foam generation in homogeneous porous media," *Colloids Surfaces A Physicochem. Eng. Asp.*, vol. 225, pp. 1–24, 2003.
- [57] P. A. Gauglitz, F. Friedmann, S. I. Kam, and W. R. Rossen, "Foam generation in homogeneous porous media," *Chem. Eng. Sci.*, vol. 57, pp. 4037–4052, 2002.
- [58] A. R. Kavscek *et al.*, "Foam Flow Experiments. I. Estimation of the Bubble generation-Coalescence Function," *Transp. Porous Media*, vol. 112, pp. 9–29, 2000.
- [59] A. H. Falls, J. J. Musters, and J. Ratulowski, "The Apparent Viscosity of Foams in Homogeneous Bead Packs," *SPE Reserv. Eng.*, vol. 4, pp. 155–164, 1989.
- [60] F. Friedmann and J. A. Jensen, "Some Parameters Influencing the Formation and Propagation of Foams in Porous Media," *Soc. Pet. Eng.*, p. 14, 1986.
- [61] W. R. Rossen, "Minimum pressure gradient for foam flow in porous media: Effect of interactions with stationary lamellae," *J. Colloid Interface Sci.*, vol. 139, pp. 457–468, 1990.
- [62] R. B. Bird, W. Stewart, and E. N. Lightfoot, "Transport phenomena," *AIChE J.*, vol. 7, p. 5J–6J, 1961.
- [63] D. B. Ingham and I. I. Pop, *Transport phenomena in porous media*. Pergamon, 1998.
- [64] Ö. Bağcı, N. Dukhan, and M. Özdemir, "Flow Regimes in Packed Beds of Spheres from Pre-Darcy to Turbulent," *Transp. Porous Media*, vol. 104, pp. 501–520, 2014.
- [65] C. Y. Wang, "Modeling Multiphase Flow and Transport in Porous Media," in *Transport Phenomena in Porous Media*, 1998, pp. 383–410.
- [66] G. Homsy, "Viscous Fingering in Porous Media," *Annu. Rev. Fluid Mech.*, pp. 271–311,

- 1987.
- [67] A. Kroezen and J. Groot Wassink, "Bubble size distribution and energy dissipation in foam mixers," *J. Soc. Dye. Colour.*, vol. 103, pp. 386–394, 1987.
- [68] V. Sanghani and C. U. Ikoku, "Rheology of Foam and its Implication inn Drilling and Cleanout Operations," *Am. Soc. Mech. Eng.*, 1983.
- [69] A. B. J. Kroezen, J. G. Wassink, and C. A. C. Schipper, "The flow properties of foam," *J. Soc. Dye. Colour.*, vol. 104, pp. 393–400, 1988.
- [70] C. Enzendorfer, "Pipe Viscometry of Foams," *J. Rheol. (N. Y. N. Y.)*, vol. 39, pp. 345–357, 1995.
- [71] J. Heller and M. Kuntamukkula, "Critical review of the foam rheology literature," *Ind. Eng. Chem. Res.*, vol. 26, p. 318, 1987.
- [72] S. A. Magrabi, B. Z. Dlugogorski, and G. J. Jameson, "Bubble size distribution and coarsening of aqueous foams," *Chem. Eng. Sci.*, vol. 54, pp. 4007–4022, 1999.
- [73] J. Grasmeijer, "Experimental determination of the bubble size in foam created in gas-liquid flow with surfactants," 2014.
- [74] L. W. Holm, "The Mechanism of Gas and Liquid Flow Through Porous Media in the Presence of Foam," *Soc. Pet. Eng. J.*, vol. 8, no. 4, pp. 359–369, 1968.
- [75] A. R. Kovscek and H. J. Bertin, "Foam Mobility in Heterogeneous Porous Media," *Transp. Porous Media*, vol. 52, pp. 17–35, 2003.
- [76] O. G. Apaydin and A. R. Kovscek, "Surfactant Concentration and End Effeccts on Foam Flow in Porous Media," *Transp. Pororus Media*, pp. 511–536, 2000.
- [77] B. X. Wang, J. H. Du, And X. F. Peng, "Internal Natural, Forced And Mixed Convection In Fluid-Saturated Porous Medium," in *Transport Phenomena in Porous Media*, 1998, pp. 357–382.
- [78] E. Christopher, Brennen, *Cavitation and bubble dynamics*, vol. 9, no. 1. 1977.
- [79] C. M. Scheid, F. P. Puget, and G. Massarani, "Fluid dynamics of bubbles in liquid," *Brazilian J. Chem. Eng.*, vol. 16, pp. 351–358, 1999.
- [80] B. Munson and T. Okiishi, *Fundamentals of Fluid Mechanics*, 7th ed. John Wiley & Sons, 2012.
- [81] Z. Zeng and R. Grigg, "A criterion for non-darcy flow in porous media," *Transp. Porous Media*, vol. 63, pp. 57–69, 2006.
- [82] C. R. Dudgeon, "An experimental study of flow of water through coarse granular media," *La houille Blanche*, pp. 785–801, 1966.

- [83] J. Bear, M. Y. Corapcioglu, and N. A. T. O. S. A. Division, *Advances in Transport Phenomena in Porous Media*. 1987.
- [84] A. Barak and J. Bear, "Flow at high Reynolds numbers through anisotropic porous media," *Adv. Water Resour.*, vol. 4, pp. 54–66, 1981.
- [85] J. Geertsma, "Estimating the Coefficient of Inertial Resistance in Fluid Flow Through Porous Media," *Soc. Pet. Eng. J.*, vol. 14, no. 5, pp. 1–6, 1974.
- [86] S. M. Hassanizadeh and W. Gray, "High Velocity Flow in Porous Media," *Transp. Porous Media*, vol. 2, pp. 521–531, 1987.
- [87] R. A. Wooding, "Multiphase Fluid Flow through Porous Media," *Annu. Rev. Fluid Mech.*, pp. 233–274, 1976.
- [88] K. R. Jolls and T. J. Hanratty, "Transition to turbulence for flow through a dumped bed of spheres," *Chem. Eng. Sci.*, vol. 21, pp. 1185–1190, 1966.
- [89] S. Ergun, "Fluid Flow Through Packed Columns," *Chem. Eng. Prog.*, vol. 48, pp. 89–94, 1952.
- [90] A. Dybbs and R. V Edwards, "A New Look at Porous Media Fluid Mechanics --- Darcy to Turbulent," in *Fundamentals of Transport Phenomena in Porous Media*, J. Bear and M. Y. Corapcioglu, Eds. Dordrecht: Springer Netherlands, 1984, pp. 199–256.

APPENDIX A      PROCEDURE FOR PRESSURE CHAMBER TESTS AND  
FOAM CAPTURE

**A.1 Pressure chamber testing procedure**

The experiments for the pressure chamber tests are carried out by following a specific procedure:

- 1) Assemble the pressure chamber and set the weighing chamber onto the weighing scale.
- 2) Pressurize the chamber to the desired a pressure, use the back pressure regulator to control the chamber pressure. Then, set the scale to zero.
- 3) Foam is generated using the system shown in the figure. Foam is initially bled-off in the bucket until the pressure transducers across the foam generator show a stable reading.
- 4) Once the pressures are stable, we partially close the bled-off valve and watch the pressure gauge (next to the bleeding off valve) until the pressure reaches the same pressure in the chamber. Then, we fully close the bleed-off valve and open the valve which connects to the pressure chamber simultaneously.
- 5) We allow the foam to flow into the pressure chamber up to a certain height and measure the mass of the foam using the scale. This helps us to determine the foam expansion ratio at pressure (FER<sub>p</sub>).

Figure A.1 shows the actual laboratory scale setup for generating foam as well as a foam capture device, back pressure regulator and a microscope to capture the foam bubbles at different pressures.

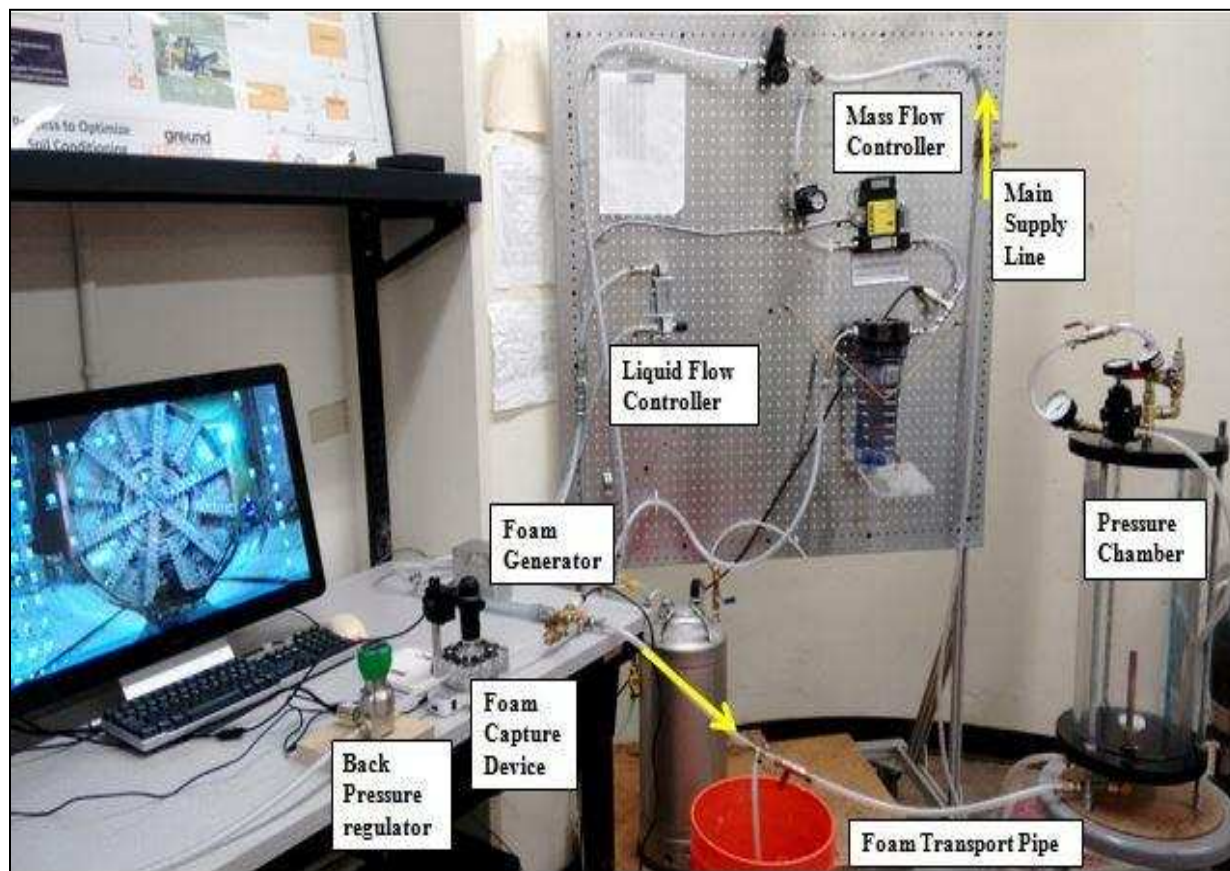


Figure A.1 Laboratory set-up for generating foam

## A.2 Foam bubble capture procedure

For photographing the foam bubbles, a specific procedure to capture the foam at the outlet of the foam generator is defined as follows:

1. Once the foam is generated, it is bleed off using the ball valve connected to the foam generator. At this time, the back pressure regulator is kept slightly open in order to flush the air through the line.
2. The back pressure is adjusted such that the air is flushed out through the device. The BPR is closed once the pressure in the capture device is similar to the pressure at the outlet of the foam generator. Then the bleed-off valve is closed.
3. The microscope shown in figure 3.6 is used to photograph the foam with the help of backlight placed under the capture device. The microscope is initially calibrated and the resolution is noted to carry out the bubble size analysis.
4. The images are captured and saved using a software tool provided with the microscope.

## APPENDIX B HISTOGRAM AND LOG-NORMAL DISTRIBUTION

The histograms with their respective log-normal distributions are shown for all the sets of experiments carried out in section 4.3 to 4.6. The histograms were generated to understand the bubble size distribution for the different conditions like variation of bead size, length of foam generator, length of transport pipe, and chamber pressure.

### B.1 Bead diameter

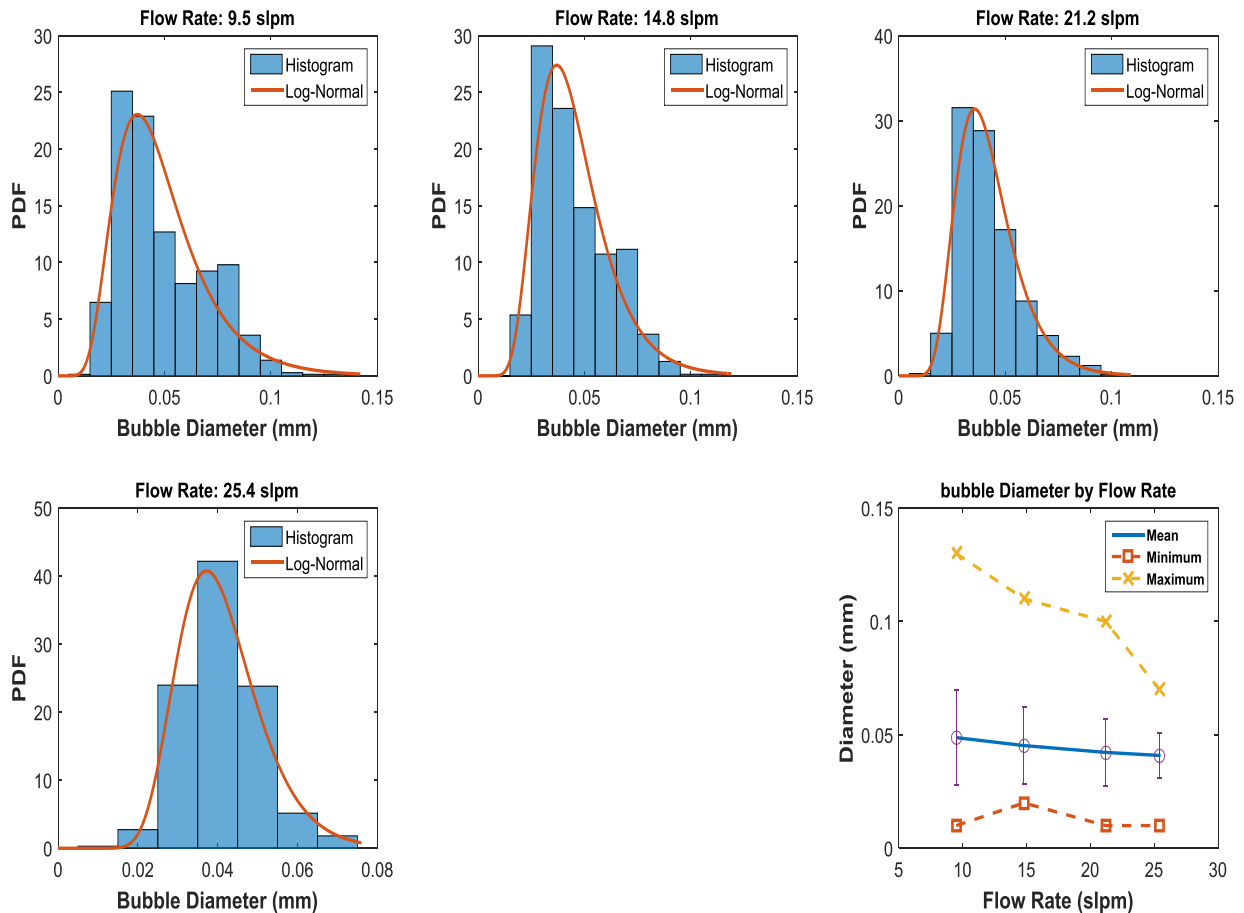


Figure B.1 Histogram with overlaid log-normal distribution for 1 mm beads

The histograms and their respective log-normal distributions for bead diameters 1, 2, and 3 mm are shown in figure B.1, B.2, and B.3 respectively. Note that for this set of experiments the length of transport pipe is fixed to 1 m, and length of foam generator is 110 mm.

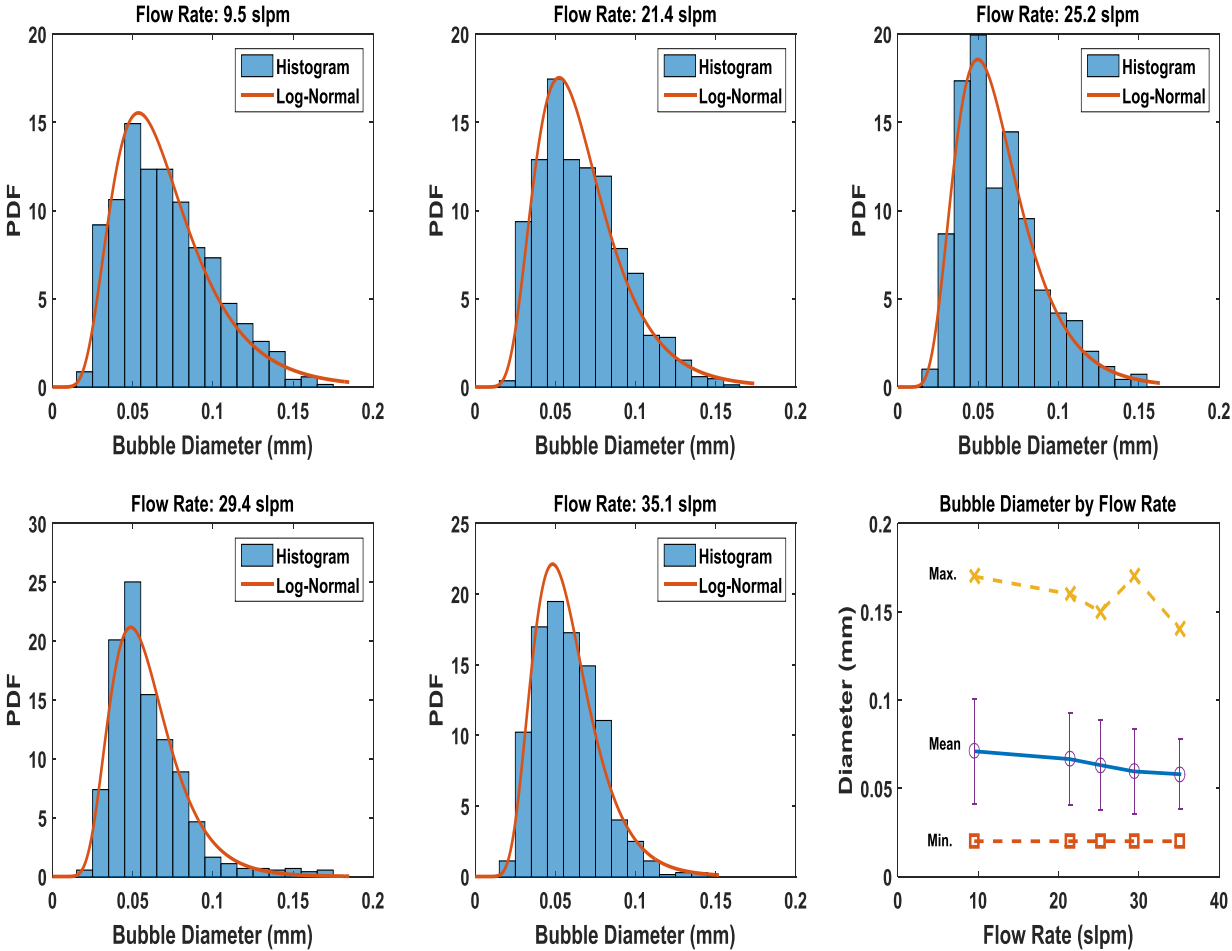


Figure B.2 Histogram with overlaid log-normal distribution for 2 mm beads

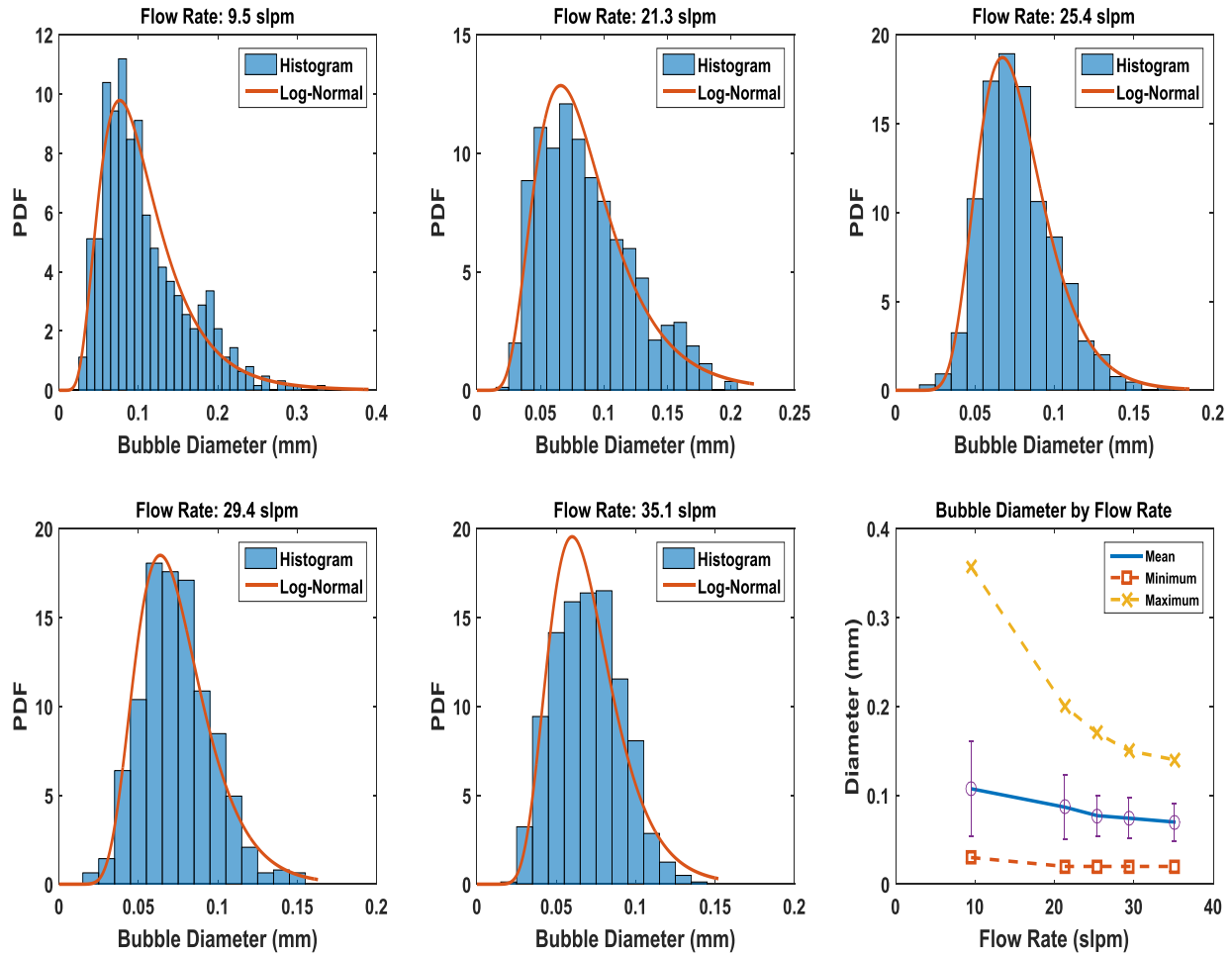


Figure B.3 Histogram with overlaid log-normal distribution for 3 mm beads

## B.2 Length of Foam Generator

The plots for the histograms and the log-normal distribution for varying lengths of foam generator ( 200 and 400 m) are shown in figure B.4 and B.5 respectively.. The plot for 110 mm length of transport pipe is shown in figure B.3. Note that for this set of experiment the length of transport pipe is fixed to 1 m, and bead size is 3 mm.

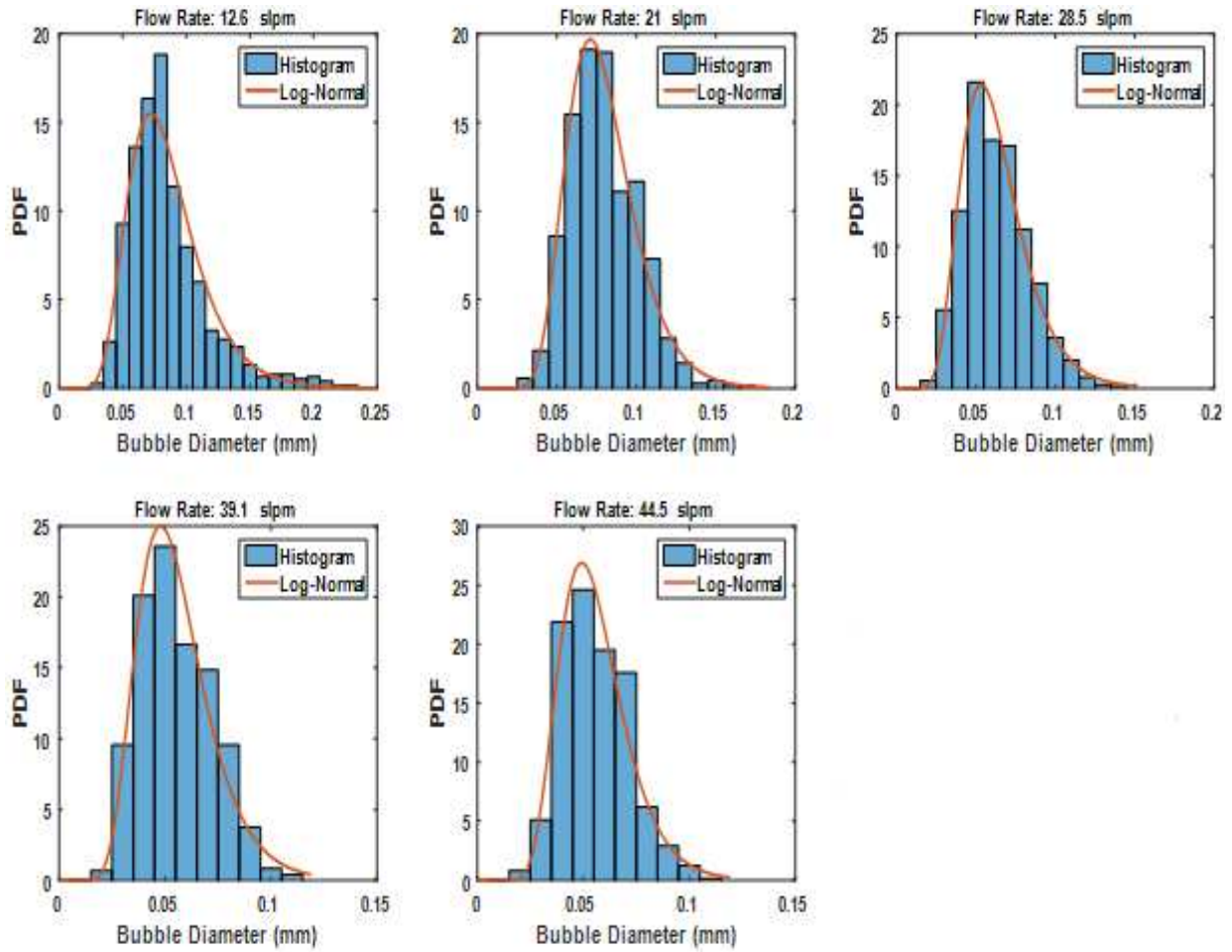


Figure B.4 Histogram with overlaid log-normal distribution for 200 mm length of generator

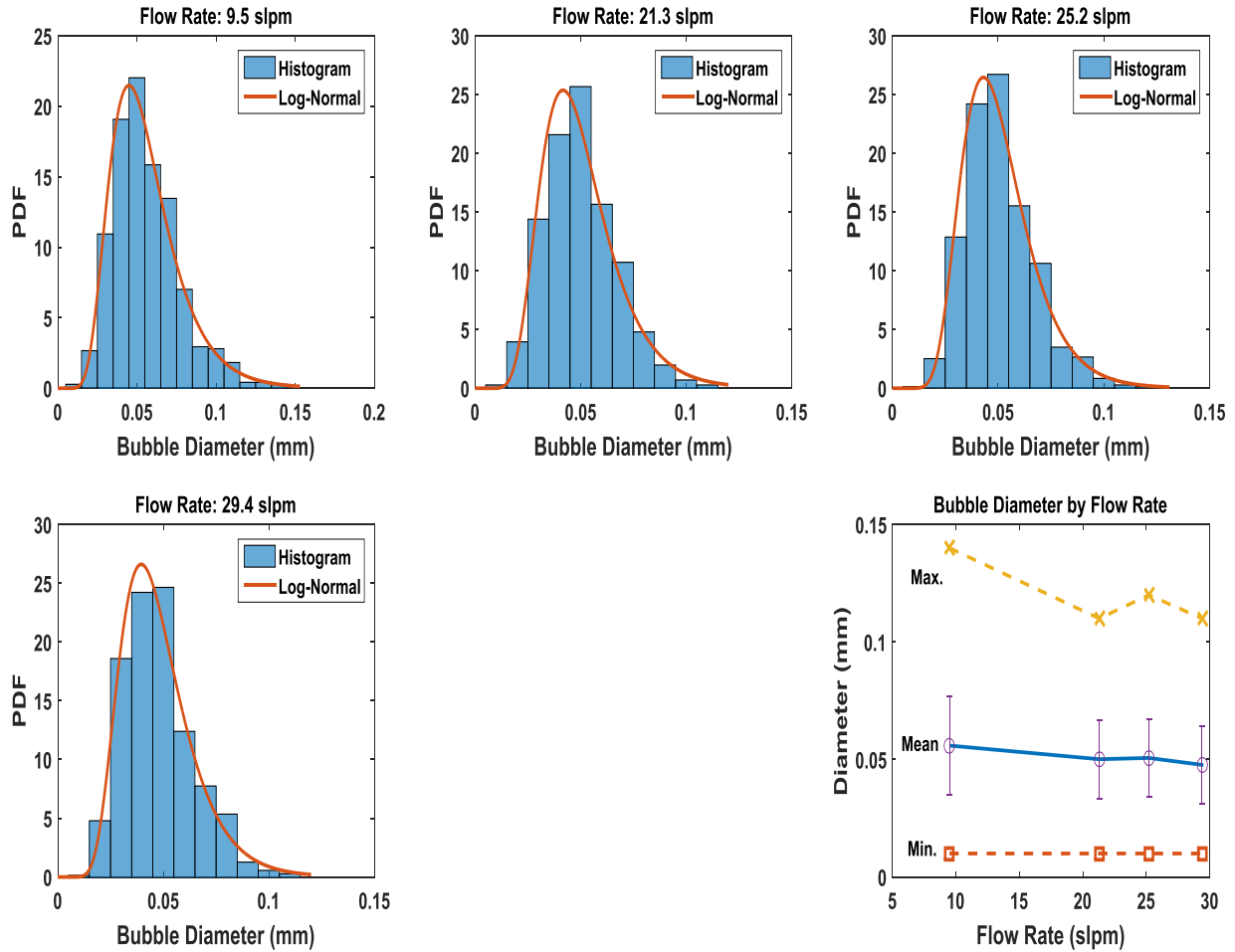


Figure B.5 Histogram with overlaid log-normal distribution for 400 mm length of generator

### B.3 Length of Transport Pipe

The plots for the histograms and the log-normal distribution for varying lengths of transport pipe (3 and 5 m) are shown in figure B.6 and B.7 respectively.. The plot for 1 m length of transport pipe is shown in figure B.3. Note that for this set of experiment the length of foam generator is fixed to 110 mm, and bead size is 3 mm.

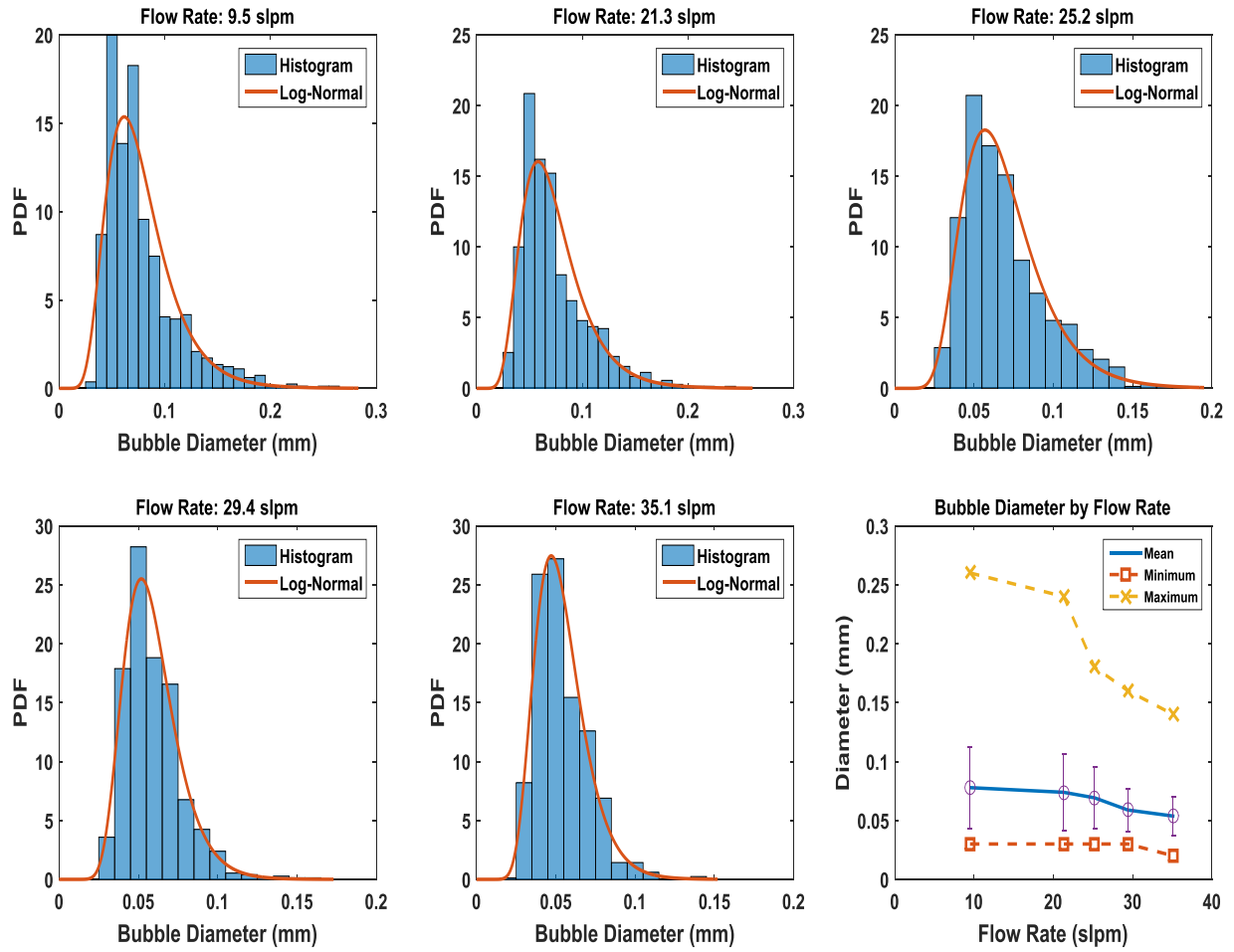


Figure B.6 Histogram with overlaid log-normal distribution for 3 m length of pipe

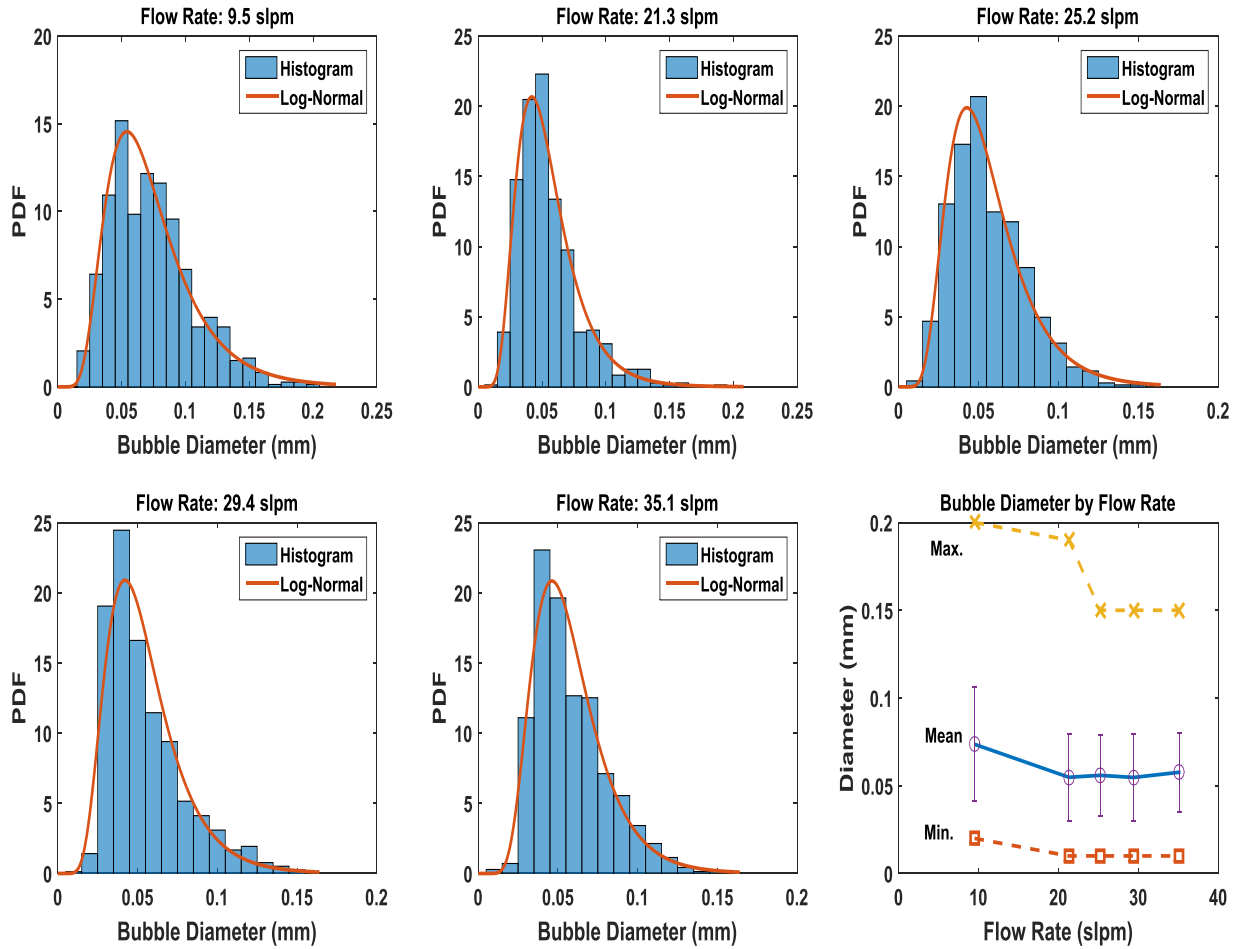


Figure B.7 Histogram with overlaid log-normal distribution for 5 m length of pipe

#### B.4 Chamber Pressure

The plots for the histograms and the log-normal distribution for varying chamber pressures (1, 3, and 5 bar) are shown in figure B.8, B.9, and B.10 respectively.. Note that for this set of experiment the length of foam generator is fixed to 200 mm, and bead size is 3 mm.

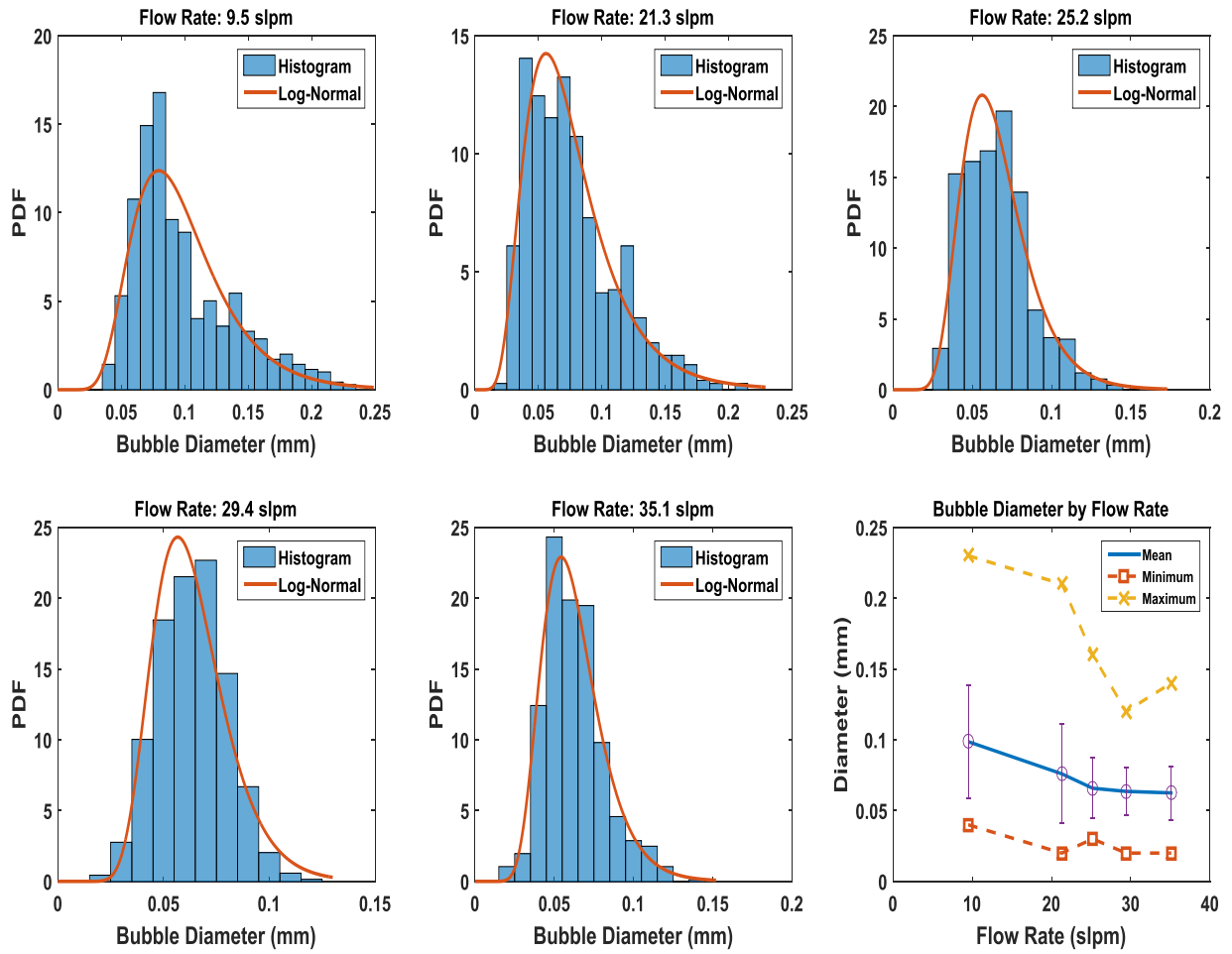


Figure B.8 Histogram with overlaid log-normal distribution for 1 bar chamber pressure

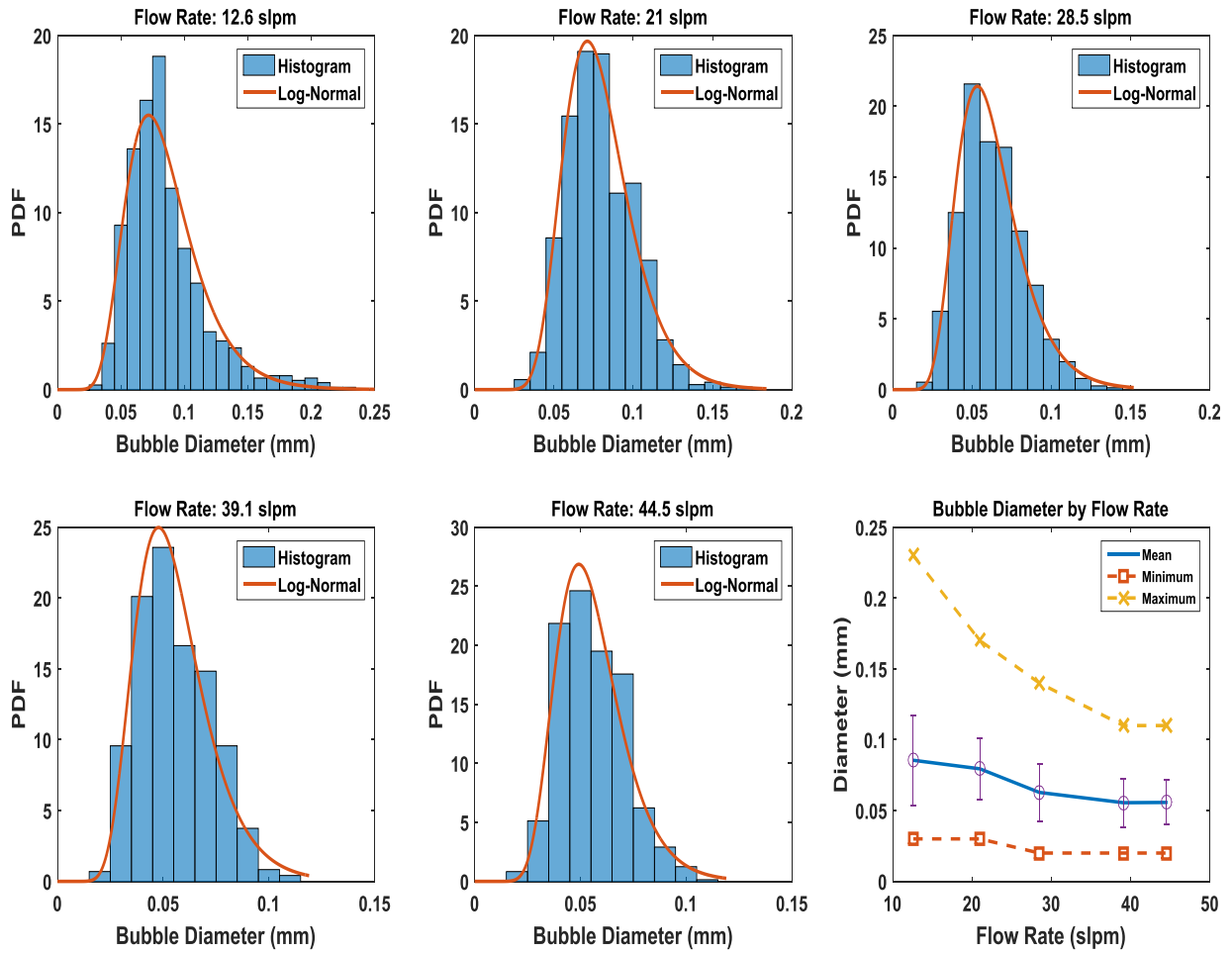


Figure B.9 Histogram with overlaid log-normal distribution for 3 bar chamber pressure

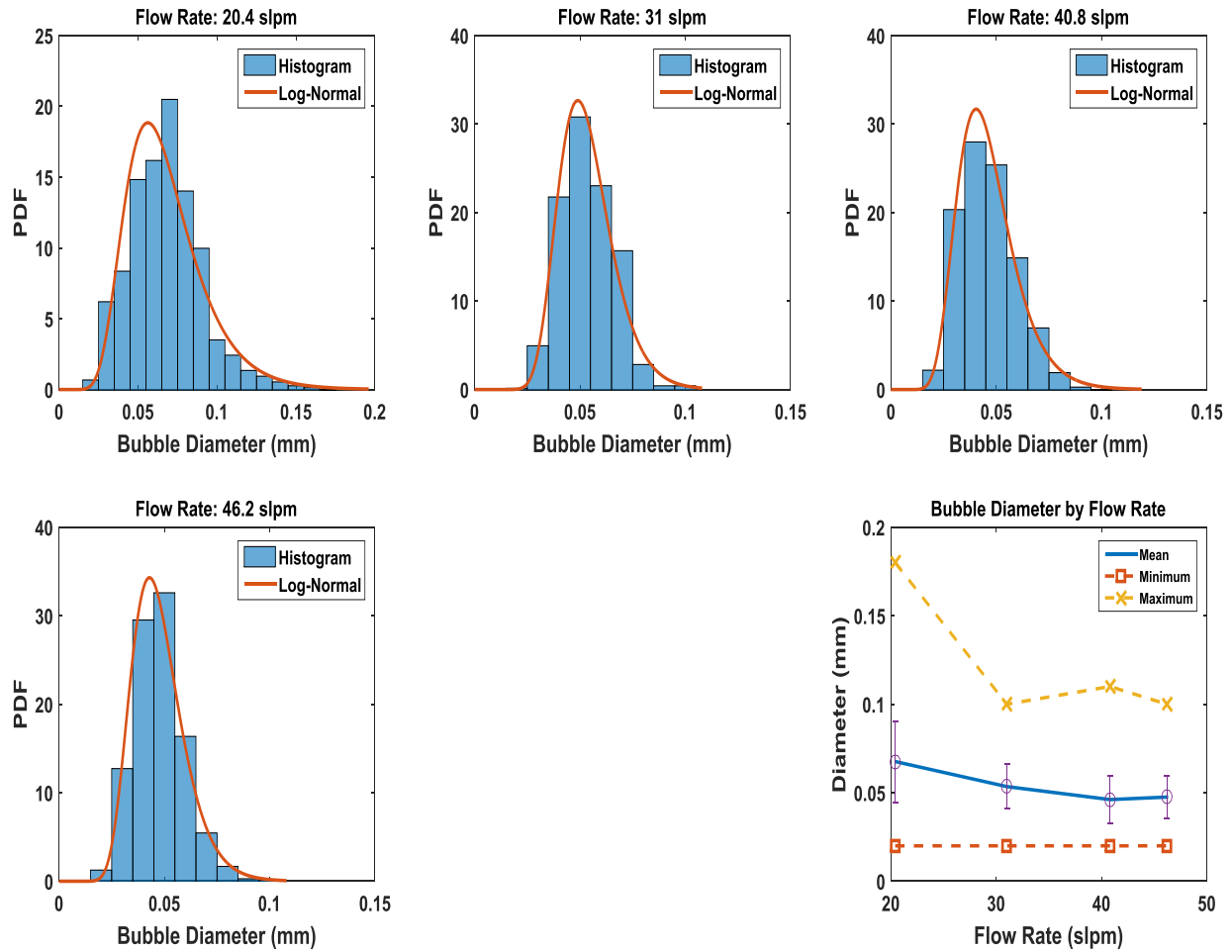


Figure B.10 Histogram with overlaid log-normal distribution for 5 bar chamber pressure

### B.5 Error for Curve Fitting

When a distribution is fit to an experimental data set, the distribution parameters are estimated to create a distribution that closely mirrors the overall patterns of the data. However, because no experimental data set will be a perfect fit for any distribution, there is an associated tolerance with any distribution curve, especially if that curve is to be used for predictive analysis. The fit tolerance is expressed as a 95% confidence interval for the driving parameters of the fit. In the case of a log-normal distribution those parameters are mean ( $\mu$ ) and standard deviation ( $\sigma$ ).

Once the confidence intervals for the parameters are calculated, the interval can be visualized by plugging the bounds of the interval into the equation for a log-normal distribution.

A confidence interval is the range of values for a parameter that there is a certain confidence level, expressed as a percent, of the actual value for the parameter existing within that range. The confidence interval is a function of the experimental data. The exact method for calculating confidence interval is beyond the scope of this report. Instead, computational tools such as MATLAB, R, or excel can be used to find confidence intervals of given data sets for various distribution types. Once the confidence interval for a parameter is calculated, it may be used to demonstrate the accuracy of a fit for describing the experimental data. The smaller the confidence interval, the better is the fit.

Example Analysis of 3mm Beads: Below are the results from an analysis of three data sets collected using 3mm beads at different flow rates. The procedure followed is,

1. Generate log-normal distribution objects using MATLAB. This is done with the 'fitdist' function.
2. Run the MATLAB function 'paramci', which generates the 95% confidence intervals for both  $\mu$  and  $\sigma$ . This is the end of pure confidence interval construction. Remaining steps are for visualization.
3. Any distribution defined by both a  $\mu$  and  $\sigma$  with the confidence interval is said to be within the interval. In order to represent the infinite number of distributions possible within the interval, calculated the values of a distribution while varying both  $\mu$  and  $\sigma$  within their ranges. The result is a 3-dimensional array of PDF values.
4. Use minimum and maximum functions to determine the smallest and largest potential value for a distribution within the confidence interval at each x value.

5. Plot the minimum and maximum values.

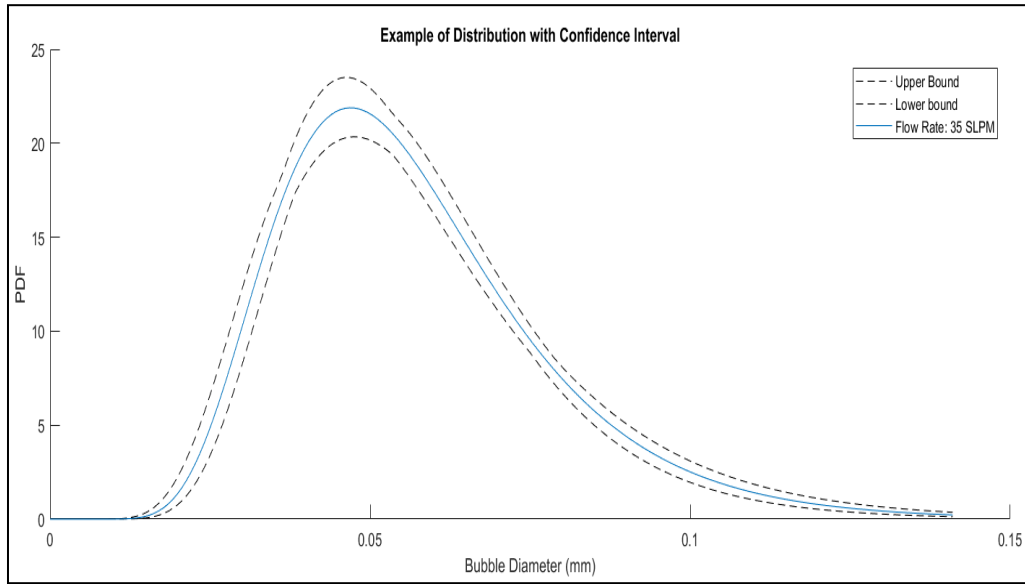


Figure B.11 Sample distribution with 95% confidence interval

Error analysis for the distribution curves with mean of the log plot ( $\mu$ ) and standard deviation ( $\sigma$ )

Table B.1 Error analysis for the distribution curves with mean of the log plot ( $\mu$ ) and standard deviation ( $\sigma$ )

<b>1 mm Beads</b>										
	9.5		14.8		21.2		25.4			
	$\mu$	$\sigma$	$\mu$	$\sigma$	$\mu$	$\sigma$	$\mu$	$\sigma$		
lower	-3.140	0.404	-3.189	0.350	-3.245	0.321	-3.246	0.242		
upper	-3.078	0.447	-3.135	0.388	-3.196	0.355	-3.207	0.269		
<b>2mm Beads</b>										
	9.5		21		25		29		35	
	$\mu$	$\sigma$	$\mu$	$\sigma$	$\mu$	$\sigma$	$\mu$	$\sigma$	$\mu$	$\sigma$
lower	-2.769	0.414	-2.816	0.383	-2.872	0.379	-2.916	0.344	-2.933	0.334
upper	-2.704	0.460	-2.762	0.421	-2.812	0.421	-2.864	0.381	-2.882	0.370

Table B.1 Continued

<b>3mm Beads</b>										
	9.5		21.3		25.4		29.4		35.1	
	mu	sigma	mu	sigma	mu	sigma	mu	sigma	mu	sigma
lower	-2.383	0.452	-2.564	0.409	-2.631	0.287	-2.675	0.305	-2.732	0.308
upper	-2.308	0.505	-2.505	0.451	-2.584	0.320	-2.624	0.340	-2.687	0.340
<b>400mm FG</b>										
	9.5		21.3		25.2		29.4			
	mu	sigma	mu	sigma	mu	sigma	mu	sigma		
lower	-2.955	0.365	-3.078	0.337	-3.060	0.315	-3.130	0.338		
upper	-2.898	0.406	-3.026	0.374	-3.011	0.350	-3.077	0.375		
<b>0 bar</b>										
	9.5		21.3		25.2		29.4		35.1	
	mu	sigma	mu	sigma	mu	sigma	mu	sigma	mu	sigma
lower	-2.417	0.359	-2.711	0.430	-2.794	0.309	-2.813	0.264	-2.840	0.291
upper	-2.361	0.399	-2.646	0.476	-2.752	0.339	-2.772	0.294	-2.797	0.322
<b>3 bar</b>										
	12.6		21		28.5		39.1		44.5	
	mu	sigma	mu	sigma	mu	sigma	mu	sigma	mu	sigma
lower	-2.543	0.322	-2.589	0.261	-2.844	0.314	-2.963	0.302	-2.949	0.275
upper	-2.495	0.356	-2.549	0.290	-2.797	0.348	-2.916	0.335	-2.906	0.305
<b>5 bar</b>										
	20.4		31		40.8		46.2			
	mu	sigma	mu	sigma	mu	sigma	mu	sigma		
lower	-2.779	0.337	-2.975	0.230	-3.141	0.284	-3.099	0.249		
upper	-2.728	0.373	-2.940	0.256	-3.098	0.314	-3.060	0.276		
<b>3 m Transport Pipe</b>										
	9.5		21		25		30		35	
	mu	sigma	mu	sigma	mu	sigma	mu	sigma	mu	sigma
lower	-2.741	0.434	-3.024	0.400	-3.004	0.406	-2.771	0.468	-2.961	0.538
upper	-2.675	0.481	-2.963	0.444	-2.941	0.451	-2.698	0.519	-2.877	0.597

Table B.1 Continued

<b>5 m Transport Pipe</b>										
	9.5		21		25		30		35	
	mu	sigma	mu	sigma	mu	sigma	mu	sigma	mu	sigma
lower	-2.784	0.463	-2.729	0.461	-2.943	0.396	-3.131	0.380	-3.030	0.322
upper	-2.713	0.514	-2.658	0.511	-2.883	0.439	-3.073	0.421	-2.980	0.357